January 2014

# SURFACE SCIENCE APPROACH TO ATOMIC LAYER DEPOSITION CHEMISTRY

Amir Gharachorlou
*Purdue University*

Graduate School ETD Form 9
(Revised 01/14)

# PURDUE UNIVERSITY
## GRADUATE SCHOOL
## Thesis/Dissertation Acceptance

This is to certify that the thesis/dissertation prepared

By Amir Gharachorlou

Entitled
SURFACE SCIENCE APPROACH TO ATOMIC LAYER DEPOSITION CHEMISTRY

For the degree of Doctor of Philosophy

Is approved by the final examining committee:

Fabio H. Ribeiro

Dmitry Zemlyanov

W. Nicholas Delgass

Michael Harris

To the best of my knowledge and as understood by the student in the Thesis/Dissertation Agreement, Publication Delay, and Certification/Disclaimer (Graduate School Form 32), this thesis/dissertation adheres to the provisions of Purdue University's "Policy on Integrity in Research" and the use of copyrighted material.

Fabio H. Ribeiro

Approved by Major Professor(s): _____

_____

Approved by: John Morgan 08/19/2014

Head of the Department Graduate Program Date

# SURFACE SCIENCE APPROACH TO ATOMIC LAYER DEPOSITION CHEMISTRY

A Dissertation

Submitted to the Faculty

of

Purdue University

by

Amir Gharachorlou

In Partial Fulfillment of the

Requirements for the Degree

of

Doctor of Philosophy

December 2014

Purdue University

West Lafayette, Indiana

*To my mom,*

***Vaji***

*and my family*

# ACKNOWLEDGEMENTS

I would like to acknowledge my advisor, Professor Fabio H. Ribeiro, and my mentor, Dr. Dmitry Zemlyanov. I am greatly indebted to the time they invested into me as a graduate student in the chemical engineering department. Looking back at my research quality, I can see a drastic improvement under Fabio's supervision. Fabio's expectations and standards have been always a great motivation for improving my research quality. Fabio has always helped me to understand the big picture in my research, and guided me in the right direction. Dima has always been available to answer all my questions with lots of bright ideas. I admire Dima's attention to experimental details and his expertise in surface science characterization techniques. Dima has the unique ability to transfer his bright ideas from a simple sketch on paper to a fully functional and sophisticated experimental device. Through 4 years of working with him in the surface science lab I have been greatly inspired by his confidence and excitement for ultra-high vacuum and surface science research. I was blessed with having the best set of advisor and mentor for a Ph. D. student working on surface science characterization.

I would also like to thank Professor W. Nicholas Delgass for his feedback and questions during our valuable meetings. I left every meeting with him with tons of new ideas. His graduate level courses in surface science characterization and heterogeneous catalysis are among the best courses I completed in graduate school. I would also like to thank the

other member of my committee, Professor Mike Harris, for providing me with helpful feedback in my preliminary exam and dissertation.

I acknowledge insight and help I received from Professor Ron Reifenberger on the STM portion of my work. He has been always a valuable part of our surface science research group with his expertise in UHV and STM techniques. Coming from a physics background, he brought a new perspective to our meetings that allowed us to improve our research quality and target a wider range of audiences.

During my initial years in grad school I was gifted to work under the guidance of Dr. Anna Nartova from the Boreskov Institute of catalysis in Novosibirsk, Russia. Anna visited us twice as a visiting researcher, and her help in teaching me about ultra-high vacuum field and the surface science characterization field is highly appreciated. I would also like to thank Dr. David Taylor. He helped me with lots of electronic repairs and taught me the correct approach to troubleshooting.

I would like to thank Dr. Xiangkui Gu and professor Jeff Greeley for their DFT calculations and collaboration with our experimental group which helped us answer complicated questions in our research.

I would also like to express my gratitude to my current and past group and classmates: Harshavardhan Choudhari, Vinod Venkatakrishnan, Dr. Wen-Sheng Lee, Dhairya Mehta, Dr. Jorge H. Pazmino, Dr. Sara Yohe, Yanran Cui, John Degenstein, Mckay Easton, Anuj Verma, James Harris, Kaiwalya Sabnis, Atish Parekh, Fred Sollberger, Dr. Paul Dietrich, and Dr. Vincent Kaspersky. I would like to especially thank Dr. Bradley R. Fingland. Brad introduced me to surface science and UHV systems and taught me how to work with different surface science analysis techniques. I have learned a lot from him during

our short time together. Advice given by Dr. Andrew Smeltz has been a great help in understanding the surface science concepts and experiments during my starting period.

I also want to thank Mike Detwiler, my lab mate whom has worked closely with me during the last 4 years. I was fortunate to have him by my side during our tough UHV experiments. His friendship and knowledge has been a valuable resource to me.

I would also like to express my appreciation to Purdue Chemical Engineering and Birck Nanotechnology Center staff that assisted me during my grad school years. I am particularly grateful for the assistance given by Dr. Yury Zvinevich and Jeff Valley and Debra Bowman.

I would also like to express great thanks to my roommate during the grad school years, Dr. Pooria Haghi, for our interesting discussions and fun times we had together.

Finally, I wish to thank my parents for their support and encouragement throughout my study. Even if I was not able to see them during last 5 years I have always felt their love. I appreciate them for all I have achieved. I would also like to thank my brother Ali and my sister Afsaneh for their love and support. I also want to thank Ava Nassir who has been by my side during the last two years in grad school. She added new sets of goals to my life and her patience and support is highly appreciated. I could simply not ask for a better companion.

I would also like to acknowledge the Department of Energy and the Institute for Atom-Efficient Chemical Transformations (IACT) for their financial support.

TABLE OF CONTENTS

Page

Page

# LIST OF TABLES

# LIST OF FIGURES

Figure Page

Figure Page

Figure Page

Figure Page

Figure Page

Figure Page

Figure Page

Figure Page

Figure Page

# ABSTRACT

Gharachorlou, Amir. Ph.D., Purdue University, December 2014. Surface Science Approach To Atomic Layer Deposition Chemistry. Major Professor: Fabio H. Ribeiro.

Recently, atomic layer deposition (ALD) has been employed as a promising technique for the growth of solid thin films with high conformality on complex geometries such as heterogeneous catalysts and microelectronic devices. In this work, surface sensitive characterization techniques have been employed to investigate initial precursor-substrate reactions and ALD surface chemistry.

To understand the nucleation and growth mechanisms of palladium nanoparticles on metal oxide supports by ALD, Pd nanoparticles were synthesized by thermal decomposition of palladium (II) hexafluoroacetylacetonate ($Pd(hfac)_2$)on a $TiO_2$(110) surface. $Pd(hfac)_2$ adsorption at room temperature is a self-limiting process on the $TiO_2$(110) surface yielding $Pd(hfac)_{ads}$ and/or $hfac_{ads}$ (hexafluoroacetylacetonate) species and partial hfac fragmentation. The removal of the hfac ligand and its fragments through thermal decomposition of surface species removes the nucleation inhibition of Pd nanoparticles previously observed for the $Pd(hfac)_2$ precursor on $TiO_2$.

Additional studies were devoted to understanding transition metal (Pd, Pt, Cu) interactions with trimethylaluminium (TMA) as an alumina ALD precursor. Over-coating of Pd, Pt and Cu nanoparticles with alumina films synthesized by TMA and water/$O_2$ as

precursors has been shown in the literature to prevent deactivation of catalyst by protecting them against particle instability (sintering). The surface chemistry of TMA was investigated on Pt(111), Pd(111) and Cu(111)/$CuO_{ads}$ surfaces with regard to its application in preventing Pd, Pt and Cu nanoparticle sintering. Our results showed that TMA decomposes to form methylaluminum (MA) on both Pd(111) and Pt(111). Further dissociation of MA to aluminum and adsorbed methyl groups is limited to step sites. Similarly, the removal of Pt and Pd atoms from (111) terraces is hindered while surface vacancy formation is facilitated on Pt and Pd step edges. Pd steps are fully covered with fractal Pd-Al alloy islands that spread over terraces. Pd hydrogenates and removes carbonaceous species, freeing step sites for MA to Al decomposition and Pd step vacancies serve as nucleation sites for Pd-Al alloy formation. On Pt(111), TMA only decomposed to MA and methyl groups. No evidence of Pt-Al alloy formation was observed on the Pt surface. The Pt(111) surface was uniformly covered with MA and residual carbon species after TMA exposure. On the Pt(111) surface, the residual carbon species were hypothesized to block access to step sites preventing MA to Al dissociation and subsequent alloy formation.

Unlike for Pt(111) and Pd(111), TMA does not interact with Cu(111). However, after exposing copper surface oxide ($CuO_{ads}$) to TMA, an alumina overlayer was detected as the TMA consumed the oxygen in $CuO_{ads}$ lattice and reduced the CuOads surface to $Cu^0$. After the first TMA half-cycle on $CuO_{ads}$, two dimensional alumina islands homogenously covered the surface. High resolution electron energy loss spectroscopy (HREELS) was used to investigate the relative occupancy of tetrahedrally and octahedrally coordinated Al ($Al_{oct}$ and $Al_{tet}$) after each alumina ALD half-cycle using

TMA and $O_2$ as precursors. TMA half-cycles produce alumina films which predominately consist of octahedral alumina ($Al_{tet}/Al_{oct} \approx 0.3$) while $O_2$ half-cycles favor formation of tetrahedral alumina ($Al_{tet}/Al_{oct} \approx 0.5$). $O_2$ half-cycles remove the residual carbon species after TMA exposure and result in a carbon-free alumina film.

# CHAPTER 1. INTRODUCTION

The thesis work presented here has been focused on understanding the surface chemistry of the atomic layer deposition (ALD) using surface science characterization techniques. The ALD technique is introduced in Section 1.1. The application of ALD in heterogeneous catalysis is discussed in Section 1.2. Common ALD *in-situ* and *ex-situ* characterization techniques are mentioned in Section 1.3. The importance of surface science characterization technique in fundamental understanding of ALD surface chemistry as well as previous studies on the surface science characterization of ALD is mentioned in Section 1.4. Finally Section 1.5 states the objective of this research and outlines the organization of the dissertation.

## 1.1 Atomic layer deposition (ALD)

Initially referred to as atomic layer epitaxy (ALE), ALD was developed by Sunola and Antson in 1970s for epitaxial deposition of ZnS and amorphous alumina in commercial flat panel screens.[1] With further development of the ALD technique, wide range of materials was deposited in non-epitaxial fashion and a more general term of ALD has been adopted.

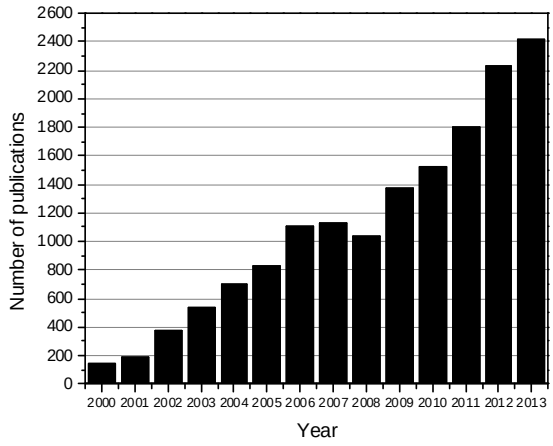


Figure 1.1. Number of scientific publications on ALD published per year during 2000 to 2013, analyzed from the SciFinder (keywords: atomic layer deposition, ALD).

In the early stage of development, ALD application was limited due to the low effective deposition rate (~100-300 nm/h) and precursor availability. Since 2000 the interest towards ALD has been rapidly increased as it is evident from the number of peer review publications appeared on the ALD (Figure 1.1). This is mainly due to the ever increasing demands in reducing the film thickness in microelectronic. With introduction of nanoscale microelectronic devices the low deposition rate of ALD became one of its greatest advantages in comparison with other available deposition techniques. Moreover, with development of new organometallic precursors the previous restriction due to lack of suitable precursors for different elements was removed. The net result was ever increasing application of ALD in thin film technology and introduction of new application such as heterogeneous catalysis.

### 1.1.1 ALD principles

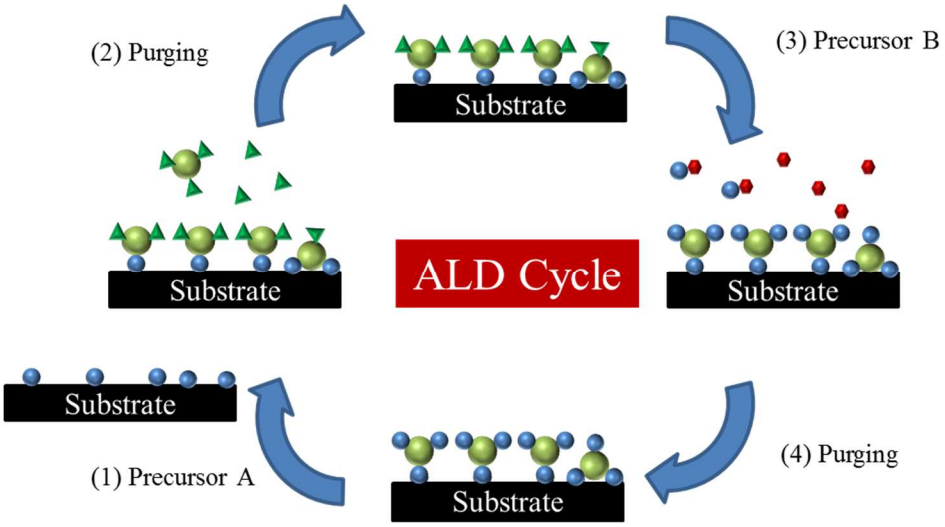


Figure 1.2. Simplified ALD principles. Four stages of an ALD cycle are shown.

The ALD process has been frequently reviewed.[2-9] In ALD the surface is alternatively exposed to the pulses of chemical precursors for certain amount of time to reach the saturation. Unlike the chemical vapor deposition (CVD) two precursors are exposed in two different stages separated by purging an inert gas between. A simplified scheme for the ALD principle is shown in Figure 1.2. One ALD growth cycle consists of four separated steps. During the first step the precursor A reacts with the surface functional groups and anchors to the substrate. The reaction proceeds until all the surface functional groups are consumed (saturation). In the second step, inert gas flows through the reaction chamber to remove the volatile byproducts and unreacted precursor. The combination of precursor exposure and consecutive purging steps is called an ALD "half-cycle". In 3$^{rd}$ step, precursor B (co-reactant) is dosed and reacts with the remaining of the first precursor ligands and regenerates the surface functional groups. The 4$^{th}$ step includes

purging byproducts and remaining of the precursor B. One cycle can generally takes about 0.3 to several seconds to complete. This process is repeated until the desired coverage (thickness) is achieved. Ideally each ALD cycle should form one monolayer (ML). However, in practice due to the surface contamination, precursor impurities, limited surface active sites or steric hindrance of the precursor ligands one ALD cycle only forms a fraction of a monolayer.

During dosing steps, the precursor from gas phase only reacts with the surface until saturation. The main advantage of ALD is originated from this self-limiting, sequential gas-surface reaction that results in high conformality of ALD-deposited film. Therefore, complicate geometries with high aspect ratio (such as porous catalyst supports) can be uniformly covered. Moreover, the film thickness can be simply controlled by the number of the ALD cycles. Other techniques such as CVD and physical vapor deposition (PVD) are not able to provide the same level of conformality and atomic-level control and are highly dependent on the dosing parameters and reaction chamber geometry and specifications. The self-limiting property of the ALD means that the exact control of precursor dosage is not required. The precursor molecules react with surface functional group and the excess molecules will be purged out during the inert gas purging step. Also, the self-limiting nature of the ALD allows for direct transition from fundamental research experiments in lab scale instruments to industrial scale applications.

## 1.2 ALD in catalysis

### 1.2.1 Metal nanoparticle deposition by ALD

ALD can be used for synthesizing metal nanoparticles on metal oxide supports in heterogeneous catalysis. The application of the ALD in heterogeneous catalysis was

recently reviewed by Junling et al. .[7] The review paper by Hämäläinen et al. summarizes the available precursors for ALD of noble metals and their oxides.[6] With exception of the gold most of the noble metals that are used in heterogeneous catalysis can be deposited using ALD. Heterogeneous catalysis takes advantage of the self-limiting property and low deposition rate of the ALD technique. For instance while non-ideal discrete coverage of the surface during initial cycles of the ALD is undesirable for many thin film applications, ALD allows one to maximize the particle surface area of the catalyst by synthesizing sub-nanometer highly dispersed metal particles on high surface area of catalyst support. Particle size and distribution play major roles in catalyst performance.[10, 11] ALD offers the possibility to control the particle size and achieve uniform particle size distribution by simply controlling the number of the ALD cycles.

In heterogeneous catalysis research, effort to link the nanoparticles size and structure to the reaction kinetics suffers from non-uniform particle size. The uniform nanoparticles deposition by ALD can enhance understanding of the structure/kinetics relationship in supported heterogeneous catalysis.[12]

By careful selection of co-reactant and deposition temperature, selective deposition of bi-metallic catalyst with atomic-level control in the catalyst composition can be achieved by the ALD technique. The step-wise deposition in ALD can be used to tune the final bimetallic morphology and composition. Bimetallic catalysts deposited by ALD have the advantages of each component and enhance the final catalyst properties comparing to their individual physical mixture because of the synergistic effects.[13, 14, 15].

### 1.2.2 Protecting metal nanoparticles by ALD

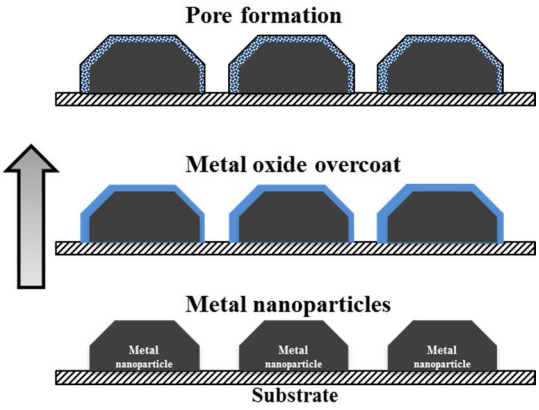


Figure 1.3. ALD can be used to uniformly deposit metal nanoparticles on catalyst support. Later the metal nanoparticles can be coated by ALD of metal oxide. Annealing the overcoat layer cause formation of a porous structure that protects the metal nanoparticle versus sintering while keeping them accessible to the reactant molecules.

Metal nanoparticles are prone to deactivation mainly caused by particle instability (sintering) and formation of the carbon filaments (coking).[16] Generally, the carbon filaments formed on the catalyst can be removed by high temperature annealing (~900 K) in oxidative environment to burn the residual carbon (calcination). Each cycle of calcination increases the metal nanoparticle size which eventually results in catalyst deactivation. The application of the ALD with atomic-level control and high conformality provides a potential solution to this problem (Figure 1.3). The transition metal nanoparticles can be coated by a uniform and conformal metal oxide layer to protect them versus particle instability while preserving their catalytical properties (reaction rate and selectivity toward the desired products).

ALD of metal oxide on metal nanoparticles have been used successfully to stabilize the metal nanoparticles during several reactions.[16-19] The metal oxide film thickness and coverage on the metal nanoparticles should be precisely controlled. If nanoparticles are buried by the metal oxide film, reactants in gas or liquid phase cannot reach the them and the ALD protective coating would fail its purpose. If the coating is too thin the nanoparticles will not be stable during the high temperature annealing.

Different strategies and mechanism have been suggested for overcoating the metal nanoparticles while keeping them accessible to the reactants phase. Lu et al. proposed that the residual organic ligands can adsorb on the surface and poison the surface during the first precursor exposures with trimethylaluminium (TMA) as the alumina precursor. These residual ligands can block the further access to the surface. During the co-reactant exposure (water) the residual ligands are removed from the deposited layer. The net effect would be formation of a porous overlayer.[19] Pores can be generated through high temperature post treatment of the overcoated catalyst. Alba-Rubio et al. stabilized copper nanoparticles on $\gamma$-$Al_2O_3$ by ALD of an alumina for liquid-phase catalytic reactions (hydrogenation of biomass-derived furfural in alcoholic solvents or water). During the alumina ALD the copper nanoparticles got completely covered with alumina overlayer. They suggested that high temperature annealing causes appearance of the porosity within the alumina overcoat by converting the amorphous alumina to the well-ordered $\alpha$-$Al_2O_3$.[20]

Lu et al. suggested that during the overcoating of the Pd nanoparticles with 45 cycles of alumina ALD the edge and corner atoms are selectively blocked by alumina overlayer. These corner atoms claimed to be responsible for instability of the Pd nanoparticles. The

resulted catalyst showed no detectable particle size changes after oxidative dehydrogenation of ethane (ODHE) at 948 K for 28 hours.[18]

The nanoparticles can be intentionally blocked prior to ALD to form a porous overlayer. In this process, the metal oxide layer is grown around nanoparticles masked with the blocking agent. Later, thermal decomposition of the blocking agent would leave pores within the metal oxide layer. This method has been used in covering the Pd nanoparticles with octadecanethiol molecules during alumina ALD on Pd nanoparticles.[21]

The interaction between transition metal nanoparticles and ALD thin film during the post annealing process plays a major role in successful protection of the nanoparticles. ALD of $TiO_2$ coating has been used to stabilize cobalt nanoparticles supported on $TiO_2$ versus sintering for aqueous-phase hydrogenation (APH) reaction.[22] While the $TiO_2$ film successfully protected the Co nanoparticles the ALD alumina film completely shut-off the reaction. The high temperature treatment applied for formation of the porosity in the ALD coating formed an irreducible cobalt aluminate phase which has no catalytical activity.

## 1.3 ALD characterization techniques

Despite the increasing interest in ALD technique little work is done on characterization and understanding of the ALD reaction mechanism and intermediates. They are three major characterization techniques that have been employed to study ALD.

### 1.3.1 Quartz crystal microbalance (QCM)

The main characterization technique used for mechanistic studies of the ALD is quartz crystal microbalance (QCM). QCM is made by a quartz crystal vibrating at its resonance frequency. When the quartz sample is covered by a deposited material, its weight is changed and its resonance frequency changes accordingly.[23] The mass gain or loss during each ALD half-cycle can be monitor by the changes in the vibration frequency of the quartz crystal. Later, assuming constant density and uniform coverage of the crystal surface or calibration of the device with other thickness sensitive techniques such as ellipsometry, the mass gain can be converted to the film thickness and the growth per cycle (GPC) can be calculated. The *in-situ* characterization capability of QCM has been a valuable tool in understanding of different ALD growth behavior.[24, 25] However, this technique suffers from lack of chemical information. Often the ALD precursors show substrate dependent behavior that deviate from the growth mechanism on the quartz surface. Different groups covered the QCM quartz surface with similar elements as the ALD substrate to resolve this problem. However, there has been no effort to validate the resemblance of the coated surface to the actual substrate used during the deposition. In fact, using ALD to pre-cover the quartz crystal prior to the actual ALD process may cause incorporation of surface contamination and impurities within the film structure that deviate from the actual growth behavior on often cleaner substrate.

### 1.3.2 Quadrupole mass spectrometer (QMS)

Mass spectroscopy has been widely employed to analyze the gas phase products that are released during each ALD half-cycles as a complimentary technique to QCM.[25, 26] The introduction of the quadrupole mass spectrometer (QMS) has helped to gather more accurate information on the ALD half-cycles. Though, most of the chemical species that are released during ALD process are very instable which make them hard to detect in gas phase. Many of these species can react together or with the reactor wall and skip the QMS analysis. Moreover, the sample surface is only responsible for very small portion of the gas phase products. The major contribution can be originated from the reactor wall with higher surface area or the heating components that cannot be seperated in the QMS analysis.

### 1.3.3 Fourier transform infrared spectroscopy (FTIR)

The FTIR has been recently introduced as *in-situ* ALD characterization technique that can provide valuable chemical information during each ALD half-cycle reaction. When it is combined with recent development in theory for peak interpretation, FTIR can be used to monitor different functional groups involve in the ALD surface chemistry.[26, 27] Adsorption of the surface sensitive probe molecules such as CO on the final film structure and following the vibration frequency of the probe molecule can provide information about the morphology of the deposited film.[16-18]

As it was mentioned in section 1.1.1 the ALD surface reactions are limited to the most outer layer of the surface. FTIR is not a surface sensitive technique and the powder samples with high surface area are generally used in FTIR characterization of the ALD process to increase the signal-to-noise ratio. Moreover, many of the surface

contaminations and reaction intermediates such as carbon are not IR active and cannot be detected by FTIR spectroscopy.

## 1.4 Surface science studies of ALD

Most of the current researches on the ALD technique are focused on synthesizing new precursors and tuning the deposition conditions by monitoring the performance and structure of the final products. Often based on the final product performance, a specific recipe for ALD deposition condition and precursors are suggested. The ideal ALD picture presented in the Section 1.1.1 (Figure 1.2) has been frequently used to explain the effect of different ALD parameters on the final chemistry and properties of the ALD process.[9] However, like many other complex chemical reactions the ideal picture is never fulfilled. The substrate condition, the ALD reaction mechanism and surface intermediates have been treated as a "black-box". This approach created a knowledge gap between the final performance of the ALD products and the surface chemistry involve in molecular level.

In the ideal ALD picture, the organometallic precursor ligands remain intact upon adoption on the surface. Based on this picture the second precursor (co-reactant) is selected to react with the remaining ligands and regenerate the original substrate condition. However, as it has been demonstrated by previous surface science studies, most of the organometallic precursors undergo stepwise thermal decomposition.[19, 28-33] The precursor decomposition becomes even more crucial and complex in case of ALD deposition on transition metals nanoparticles that are catalytically active. During the second ALD half-cycle the main role of the co-reactant is to provide the missing element such as oxygen, sulfur and nitrogen and removing the residual ligands. Often, the co-reactant is found to be ineffective in removing the surface intermediates which incorporate organic fragments inside the film structure.

The surface science characterization can bridge the knowledge gap exist in ALD chemistry. The importance of the surface science characterization is highlighted by Zaera in his recent ALD review paper:" Many surface-science techniques are already available for the study of the chemistry of ALD. This is at present an undeveloped area of research. The potential is there…".[34]

### 1.4.1 Surface science characterization of the ALD in literature

Many of the challenges in ALD surface chemistry and growth behavior can be answered by employing surface science characterization techniques. X-ray photoelectron spectroscopy (XPS) and scanning tunneling microscopy (STM) are two common techniques used for surface characterization of ALD. In next section, the application of these two surface science characterizations techniques in ALD surface chemistry is reviewed.

#### 1.4.1.1 X-ray photoelectron spectroscopy (XPS)

The adsorption of copper(I)-N,N′-di-sec-butylacetamidinate as a copper ALD precursor on a Ni(110) surface was studied by XPS. The binding energy of the copper was used to track the chemical sate of the organometallic molecules. By following the BE of Cu 2p peak, it was shown that dosing the copper acetamidinate on Ni at temperature higher than 500 K (typical ALD dosing temperature) causes dissociative adsorption of the precursor and formation of the metallic copper particles. With this precursor, $H_2$ is typically used in the second half-cycle to react with the organic ligands and remove the carbon species. The dissociative adsorption of the copper acetamidinate makes the organic ligands unavailable for the hydrogenation and removal from the surface in the second ALD half-

cycle. As a result impurities and carbon species are incorporated inside the deposited film.[35]

Thermal chemistry of copper(I)- N,N′-di- sec-butylacetamidinate adsorbed on Cu(110) single-crystal surfaces has been studied by XPS technique. The copper acetamidinate decomposition on Cu surface has a low probability (approximately 10%). This offers a wide deposition temperature and makes the $H_2$ exposure in the second ALD half-cycle effective in achieving impurity-free copper film.[36]

Adsorption of ALD precursor bis(N-tert-butyl-N′-ethylpropionamidinato) cobalt(II) (CoAMD) on Cu surface was studied by XPS. XPS spectra showed that the CoAMD precursor decomposed to $Co^0$ and absorbed AMD ligands on the copper surface. The carbon region in the XPS spectra showed that in the second half-cycle $H_2$ can be used to remove the chemisorbed AMD ligands to achieve carbon-free Co film.[37]

Surface chemistry of the copper(I) β-diketonate precursor for ALD of Cuprous oxide ($Cu_2O$) on $SiO_2$ was investigated by in-situ x-ray photoelectron spectroscopy. Presence of metallic Cu due to the thermally induced disproportionation of the precursor was detected for temperature above 473 K. Based on the XPS characterization it was suggested that the ALD temperature range should be kept below 500 K to keep the precursor intact after chemisorption on the substrate.[38]

The copper(II)acetylacetonate $Cu(acac)_2$, adsorption on Ni(110) and Cu(110) single crystal surfaces was probed by XPS. Based on the BE of the Cu 2p and C 1s peak a reaction pathway for the first ALD half-cycle was suggested. At 300 K, the $Cu(acac)_2$ reduced to metallic copper while the remaining acac ligands remained intact on the

surface. The intact acac ligands can be removed by using $H_2$ during the second half-cycle.[29]

Initial ALD stages of ZnO using diethylzinc as metal-precursor and oxygen ($O_2$) as co-reactant have been analyzed by XPS and synchrotron radiation photoemission spectroscopy (SR-PES) techniques. Replacing the water with oxygen as the co-reactant favored ZnO structure with increased level of the interstitial $O_2$ defects while the rest of chemical structure of the ZnO film remained intact.[39]

Deposition of different ALD precursors has been shown to result in native oxide removal in group III–V semiconductors such as GaAs and InAs in a process called “clean-up” effect. The removal of the oxide layer during initial ALD cycles can increase the quality of the III–V semiconductors devices by preventing the charge trapping at the interface.

The formation of oxide interfacial layer during ALD of $TiO_2$ on InAs(100) substrate with tetrakis (dimethylamino) titanium and $H_2O$ has been investigate by XPS. Upon adsorption of the precursor the surface arsenic oxide was reduced. However, the oxide layer removal was limited to the very first layer of the $TiO_2$ ALD and increased in intensity with film thickness due to diffusion of the surface indium oxide through $TiO_2$ film.[40]

The ALD of alumina on Ru and $RuO_2$ has been investigated by SR-PES. Exposing the $RuO_2$ to trimethylaluminium (TMA) as an alumina precursor removed the adsorbed and sub-surface oxygen species by reducing the initial $Ru^{+4}$ to $Ru^0$ which is crucial for enhancing the final film application.[41]

#### 1.4.1.2 Scanning tunneling microscopy (STM)

The ALD of alumina on graphene has been probed by STM. Imaging the surface after exposure to TMA showed that only the graphene step edges are active versus TMA. Functionalizing the graphene surface with perylene tetracarboxylic acid (PTCA) molecule caused uniform coverage of the graphene surface with alumina ALD.[42]

Mack et al. combined scanning tunneling microscope with ALD (STM-ALD) to perform in situ imaging of initial stages of ALD. As a proof of concept ZnS ALD was performed on the Au(111) surface by using diethylzinc and hydrogen sulfide. The STM images were obtained after each half-cycle up to 5 ALD cycles to show the validity of the ALD-STM system. ZnS started to grow as 3D clusters with grain sizes that showed temperature dependent behavior.[43, 44]

The surface chemistry of alumina ALD on the InP(100) was studied by STM and XPS. Initial alumina ALD cycles could not suppress the surface oxidation and caused formation of a defective $AlPO_4$ overlayer. Alumina film started to grow on the $AlPO_4$/InP during further ALD cycles.[45]

## 1.5 Motivation

With the application of the ALD limited to initial deposition cycles due to ever-increasing demand in shrinking the microelectronic devices, the substrate has become one of the main ALD reactant. The substrate-precursor interaction can tailor the final properties of deposited layer. With application of the ALD in thin film technology successful ALD process starts with characterization of the substrate and its interaction with ALD precursors during the initial ALD cycles. Moreover, application of the ALD in protecting metal nanoparticle in absence of surface functional group has complicated the general picture presented for surface-precursor interactions. In case of transition metal substrates the question is how the precursor reacts with a surface in absence of any surface functional group. What is active site available for precursor-substrate interaction on clean metal surface? What controls the ALD nucleation process and what can be done to avoid the nucleation delay? What are the surface intermediates in ALD?

Many of these challenges and questions concerning the underlying surface chemistry of alumina ALD can be answered by employing the surface science characterization techniques in a contamination free environment.

The dissertation is organized as follows. Chapter 2 presents the ultra-high vacuum (UHV) setup and our general experimental procedure. Chapter 3 present the study on nucleation and growth of palladium nanoparticles on $TiO_2$(110) surface using Pd hexafluoroacetylacetonate ($Pd(hfac)_2$) as ALD precursor. Chapter 4 contains the surface science characterization of alumina ALD using trimethylaluminium (TMA) on Pt(111) and Pd(111) single crystal with regard to its application in protecting Pd and Pt nanoparticles versus sintering and coking in heterogeneous catalysis. Chapter 5 focused

on alumina ALD on Cu(111) and copper surface oxide using TMA and water/$O_2$ as ALD precursor and co-reactants, respectively.

# CHAPTER 2. EXPERIMENTAL

## 2.1 Preparation chamber and precursor dosing line

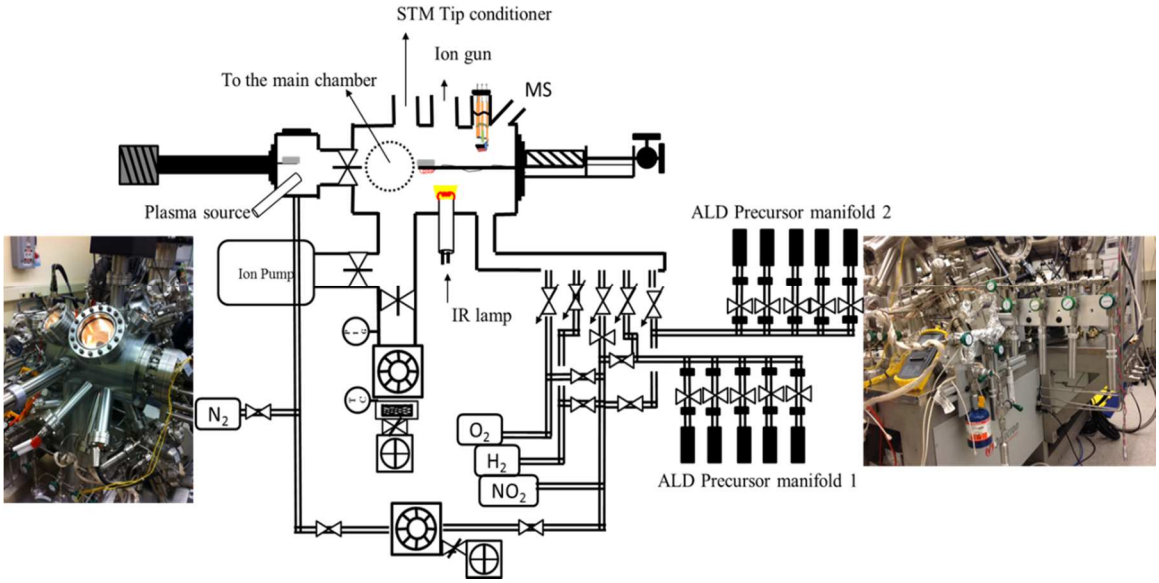


Figure 2.1. Simplified scheme for ALD dosing line and preparation chamber.

The majority of the experiments were carried out in Omicron Surface Analysis Cluster system at the Birck Nanotechnology Center (BNC) the set up consist of an ultra-high vacuum (UHV) preparation chamber and μ-metal analysis chamber with base pressures of $1\times10^{-9}$ mbar and $5\times10^{-11}$ mbar, respectively. The other experimental setups will be discussed where it was used. The preparation chamber is shown schematically in Figure 2.1. The preparation chamber was equipped with a mass spectrometer (MS), an $Ar^+$ sputtering gun (ion gun), resistive sample heating, STM tip conditioning stage, internal

bakeout IR heater (stab-in heaters using vacuum-compatible quartz IR lamps) designed to heat the preparation chamber walls and two ALD precursor manifolds connected through separated leak valves to the preparation chamber. The sample is introduced to the system via a load lock. The load lock is equipped with the Evactron® RF plasma cleaner (XEI Scientific, Inc.[46]).

The precursor-dosing line consists of two separated dosing lines built by VCR-fittings. Swagelok miniature sample cylinders were used as a reservoir for different organometallic precursors. Each cylinder was isolated from the dosing line by a shut-off VCR valve (Viton-free). The fluorine containing precursors were attached to manifold 1 while the other precursors are connected to manifold #2 to avoid fluorine cross contamination (see Figure 2.1) that are hard to remove. The dosing line can be heated by a heating tape. The dosing line temperature was controlled via three K-type thermocouples spread over the dosing lines. The dosing manifolds are pumped by a turbo pump to the base pressure of ~$1\times10^{-8}$ mbar.

### 2.1.1 Precursor safety precautions

Some of the precursors used in this research such as trimethylaluminium (TMA) and titanium isopropoxide (TTIP) are highly pyrophoric and react violently upon contact with air or water. Working with the pyrophoric material requires extreme care. Following design parameters and procedure have been placed to ensure safe usage of the precursors during our experiments:

- Miniature sample cylinder with the smallest available volume (10 $cm^3$) has been used to lower the risk of accidental release of the precursor.

- Minimum amount of each precursor is place inside the mini cylinders in an oxygen free glove-box and the cylinders are sealed by VCR Viton-free shut-off valves and VCR caps before transferring out of the glove-box.
- During the pumping procedure, the dosing line is pumped down by a turbo pump. Then the line is isolated from the pumping system and is opened to the mini-cylinder to avoid direct opening of the precursor to the pumping device.
- The turbo pump is attached to an oil sealed rotary vane vacuum pumps that can become contaminated with continuous pumping of the precursors. During prolong usage of the pump some of the precursor can end up in the pump oil. Using gas ballast on the rough pump allows a small flow of the air to enter the compression side of the pump. The air can naturalize the remaining of the precursor in the pumping oil. Using gas ballast device and frequent change of the pump oil can prevent potential accidents due to the sudden air exposure of large amount of the precursor during pump oil changes.
- We used the”Ultra-grade Oil” pump oil from Edwards company with the anti-oxidants included in the oils that enable the pump to withstand reactive species.

## 2.2 Analysis chamber

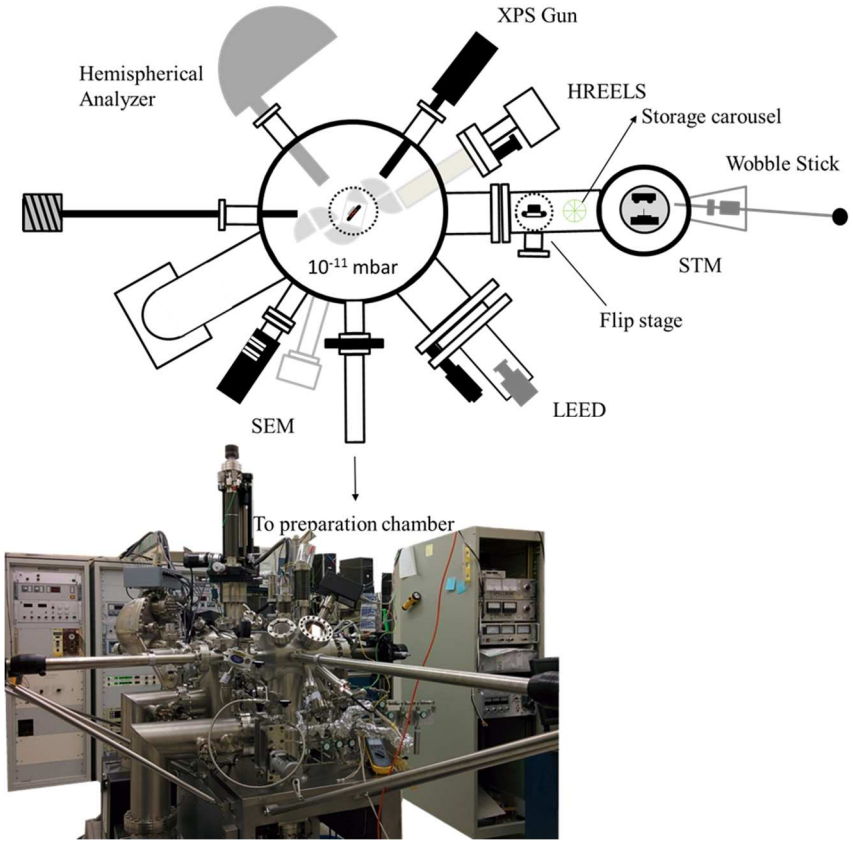


Figure 2.2. Omicron analytical chamber is shown schematically along the instrument picture used in this study.

The analysis chamber was equipped with XPS, low energy electron diffraction (LEED), high resolution electron energy loss spectroscopy (HREELS), STM, resistive sample heating and sample storage carousel. Up to six samples can be stored in the sample storage carousel. During the sample transfer from the XPS stage to STM the sample need to be rotated by 90 degree. A flip stage is located along the STM transfer arm to fulfill this task (see Figure 2.2).

STM images were obtained at room temperature in a constant current (topographic) mode with an electrochemically etched W tip. STM tips were conditioned by electron bombardment in the preparation chamber. The tip preparation procedure is explained in section 2.3. The STM images are displayed in a 2-D top-view representation with dark regions corresponding to lower levels. The sample temperature was measured by a K-type thermocouple spot welded to the stainless steel back plate. In order to assure that the crystal surface reached the desired temperature in our STM and HREELS experiments, the thermocouple reading was held constant for 15 min before cooling down the sample to room temperature.

## 2.3 STM tip preparation stage

The STM image resolution is a function of the tip sharpness used in STM imaging. Therefore, we tried different tip preparation methods to achieve a reliable tip that can provide consistent atomic resolution images on the suitable substrates. Achieving sharp STM tips is a well-developed art.[47] The tungsten etching tip station used for preparing STM tips is shown in Figure 2.3. The etching process is based on the electrochemical reaction shown below:[48]

| | | |
|---|---|---|
| *Cathode* | $6H_2O + 6e^- \rightarrow 3H_2(g) + 6OH^-$ | $SRP = -2.48V$ |
| *Anode* | $W(s) + 8OH^- \rightarrow WO_4^{2-} + 4H_2O + 6e^-$ | $SOP = +1.05V$ |
| *Total* | $W(s) + 2OH^- + 2H_2O \rightarrow WO_4^{2-} + 3H_2(g)$ | $E^0 = -1.43V$ |

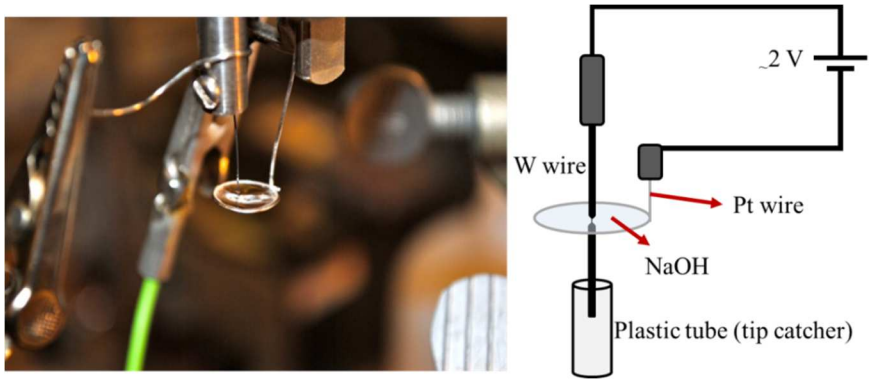


Figure 2.3. STM tip preparation stage. The W tip is etched inside the NaOH solution meniscus.

Tungsten wire with 10 mil (0.25 mm) diameter was used. Both AC and DC voltage have been tested for etching process. During our experiments AC voltage showed to be more reliable and consistent in producing sharp tips. Hydrogen bubbles are formed at the Pt ring during the etching process which allowed for visual control of the etching rate. The etching rate can be adjusted by changing the applied voltage or refreshing the etching solution. Solution of 1 molar NaOH in water has been used as the electrolyte. Current passing through the Pt wires was in the range of 15 mA. After catching the etched tip in the plastic tube (tip catcher) it is crucial to extensively rinse the tip in deionized water followed by ethanol to remove the traces of the NaOH. Failure to remove traces of the NaOH on the W tip can results in crashing the tip during the tip approaching step. Once the W tip is transferred inside the UHV chamber the W surface oxide layer is removed by a home-built e-beam heating stage. We probed the emission current on the W tip during the e-beam heating. The heating is continued until reaching to the maximum emission current as the emission current density is inversely proportional to the tip area.

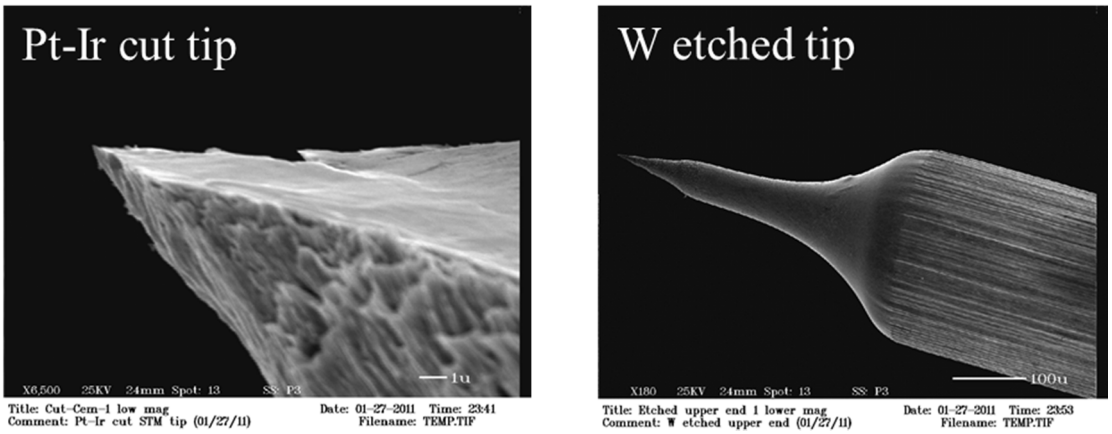


Figure 2.4. SEM images of the Pt-Ir cut tip versus the W etched tip. The cone shape of the etched tip makes more reliable STM tip that can be used for atomic resolution imaging.

The sharpness and appearance of the etched W tip was studied by scanning electron microscopy (SEM) and compared with the cut Pt-Ir tips in Figure 2.4. It is possible to achieve sharp STM tips by cutting Pt-Ir wires. However, the Pt-Ir tips are not stable for long term imaging and have a tendency to become dull after few cycles of scanning. The W etched tips showed more reliable and consistent scanning behavior. Moreover, the W tip sharpness can be regenerated by e-beam bombardment or annealing. Annealing the W tip can further sharpen the tip by removing the adsorbed species at the tip apex and formation of the most stable W(111) structure.

## 2.4 *Ex-situ* batch reactor

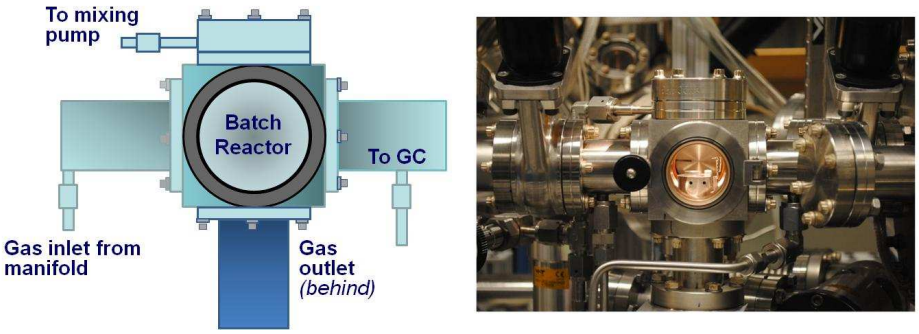


Figure 2.5. *Ex-situ* batch reactor connected to UHV chamber.

The batch reactor attached to the UHV system is shown in Figure 2.5. The batch reactor is attached to the UHV setup via a gate valve. This UHV apparatus has three main chambers: a PHI 5400 XPS chamber, an RHK UHV 350 AFM/STM chamber and preparation chamber equipped with e-beam heater and $Ar^+$ sputtering gun. The reactor is capable of performing catalytical reactions at ambient pressure (~760 Torr) on single crystals and foils without exposing the sample to the air. The sample can be directly transferred from UHV chamber to the batch reactor by use of magnetic transfer arm. The reactor can be evacuated from the atmospheric pressure to UHV regime by two separated scroll and turbo pumps. Gas chromatograph (GC) equipped with a flame ionization detector (FID) and a capillary column was used to monitor the hydrocarbon conversion and rate measurements.

Research purity ethylene (Matheson, 99.98% purity), hydrogen (Matheson, 99.99% purity), and Argon ultra-high purity grade (Matheson, 99.9% purity) was passed over a molecular sieve trap before use. During gas input the crystal was heated to the reaction temperature. The typical reaction gas mixture consisted of 10 Torr $C_2H_4$, 20 Torr $H_2$, and

Ar make-up gas to bring the total gas pressure to 760 Torr. Hydrogen was always introduced first, followed by ethylene. Circulation was started after introducing all the gases inside the reactor and whole process took about 2 minutes which was followed by 10 min of mixing before any data collection. Only one batch reaction was carried out for each clean sample to minimize effects of contamination. The reaction temperature was continuously regulated within ±1 K by using a temperature controller connected to IR lamp as a heating source and a K-type thermocouple spot-welded to the corners of the single crystal. The effect of thermocouple position on the side of the crystal as well as inevitable variations in placing crystal inside the RHK sample holder was tested by remounting the crystal several times and achieving similar kinetics parameters such as activation energy and turnover rates. Reaction rate was calculated from the slopes of product accumulation curves as a function of time. Blank experiments using empty sample holder with thermocouple attached to the sample holder body at 333 K showed negligible rate as the GC peak area was close to the background and only after two hours the rate can be measured to be less than 5% of the value measured for the clean single crystal sample.

## 2.5 XPS coverage and thickness model derivation

Differential photoelectron peak intensity as a function of photoemission angle, $dN_S(\theta)$, from a bounded, uniform density substrate, *s*, can be written as:

$$dN_s(\theta) = I \times \rho \times \frac{d\sigma_s}{d\Omega} \times \Omega(E_{kin}, x, y, z) \times D \times \exp\left(\frac{-z}{\Lambda_e^{subst}(E_s) \times cos\theta}\right) dxdydz \quad (1)$$

where $I$ is the x-ray flux, and is constant in most spectrometer systems at constant hν; $\rho$ is the number of atoms or molecules per unit volume, $\frac{d\sigma_s}{d\Omega}$ is differential cross-section for the substrate photoemission peak, which can be calculated from Scofield cross sections and the Reilman asymmetry parameter, Ω is the acceptance solid angle of the electron analyzer; $D$ is the instrument detection efficiency, which is the probability that an escaped electron encompassed by the acceptance solid angle will yield a single count and $\Lambda_e^{subst}(E_s)$ is the electron attenuation length of an electron originating from the substrate which was calculated using NIST SRD-82, $\theta$ is the angle of electron takeoff relative to the surface normal. The exponential term is the probability for no-loss escape from the specimen, where $\frac{z}{cos\theta}$ is the path length.

Integrating,

$$\int dN_s(\theta) = \int_{-\infty}^{\infty}\int_{-\infty}^{\infty}\int_{0}^{t} I \times \rho \times \frac{d\sigma_s}{d\Omega} \times \Omega(E_{kin}, x, y, z) \times D \times \exp\left(\frac{-z}{\Lambda_e^{subst}(E_s) \times cos\theta}\right) dxdydz \quad (2)$$

$$N_s(\theta) = I_s \times \Omega_s(E_s) \times A_S(E_s) \times D_S \times \rho_s \times \frac{d\sigma_s}{d\Omega} \times \Lambda_e(E_s) \times cos\theta \times \left(1 - exp\left(\frac{-t}{\Lambda_e^{subst}(E_s) \times cos\theta}\right)\right) \quad (3)$$

Where $A_S$ is the effective substrate area.

### 2.5.1 Derivation of non-attenuating overlayer model

This derivation follows the approach by Fadley. Substrate peak intensity, $N_s(\theta)$, for a semi-infinite substrate, where the substrate is represented by subscript *s*, can be represented by Equation 4, where the limit of Equation 2 is taken as t tends to infinity:

$$N_s(\theta) = I_s \times \Omega_s(E_s) \times A_S(E_s) \times D_S \times \rho_s \times \frac{d\sigma_s}{d\Omega} \times \Lambda_e^{subst}(E_s) \times cos\theta \quad (4)$$

Peak intensity from the overlayer, represented with subscript *l*, is written as:

$$N_l(\theta) = I_l \times \Omega_l(E_l) \times A_l(E_l) \times D_l \times s_l \times \frac{d\sigma_l}{d\Omega} \quad (5)$$

Where $s_l$ is the average surface density of atoms in the overlayer in cm$^{-2}$.

The ratio of overlayer to substrate peak intensity can be written as:

$$\frac{N_l(\theta)}{N_s(\theta)} = \frac{I_l \times \Omega_l(E_l) \times A_l(E_l) \times D_l \times s_l \times \frac{d\sigma_l}{d\Omega}}{I_s \times \Omega_s(E_s) \times A_S(E_s) \times D_S \times \frac{s_s}{d_s} \times \frac{d\sigma_s}{d\Omega} \times \Lambda_e^{subst}(E_s) \times cos\theta} \quad (6)$$

Where $\rho_s = s_s/d_s$, $d_s$ is the average separation of layers of density $s_s$ in the substrate. Solving for $s_l/s_s$ then yields the coverage:

$$\frac{S_l}{S_s}$$

$$= \frac{N_l(\theta) \times I_s \times \Omega_s(E_s) \times A_S(E_s) \times D_S \times \frac{d\sigma_s}{d\Omega} \times \Lambda_e^{subst}(E_s) \times cos\theta}{N_s(\theta) \times I_l \times \Omega_l(E_l) \times A_l(E_l) \times D_l \times \frac{d\sigma_l}{d\Omega} \times d_s} \quad (7)$$

$I_s = I_l$, and $D_S = D_l$ for constant pass energies so Equation 7 simplifies to:

$$\Theta = \frac{S_l}{S_s}$$

$$= \frac{N_l(\theta) \times \Omega_s(E_s) \times A_S(E_s) \times \frac{d\sigma_s}{d\Omega} \times \Lambda_e^{subst}(E_s) \times cos\theta}{N_s(\theta) \times \Omega_l(E_l) \times A_l(E_l) \times \frac{d\sigma_l}{d\Omega} \times d_s} \quad (8)$$

### 2.5.2 XPS model for thickness, *t*, of uniform overlayer

Peak intensity of the overlayer, $N_l(\theta)$, follows directly from Eequation (2), integrating over z from 0 to *t*:

$$N_l(\theta) = I_l \times \Omega_l(E_l) \times A_l(E_l) \times D_l \times \rho_l \times \frac{d\sigma_l}{d\Omega} \times \Lambda_l(E_l) \times cos\theta \times \left(1 - exp\left(\frac{-t}{\Lambda_l(E_l) \times cos\theta}\right)\right) \quad (9)$$

Where $\Lambda_l(E_l)$ is the electron attenuation length of an electron originating from the overlayer with kinetic energy $E_l$ through the overlayer.

For the substrate, Equation 2 is integrated over z from *t* to infinity in the case of a semi-infinite substrate, yielding:

$$N_s(\theta) = I_s \times \Omega_s(E_s) \times A_S(E_s) \times D_S \times \rho_s \times \frac{d\sigma_s}{d\Omega} \times \Lambda_s(E_s) \times cos\theta \times \left(exp\left(\frac{-t}{\Lambda_l(E_s) \times cos\theta}\right)\right) \quad (10)$$

Where $\Lambda_l(E_s)$ is the electron attenuation length of an electron originating from the substrate with kinetic energy $E_s$ through the overlayer.

Rearranging and cancelling similar terms yields the equation 11 that can be solved numerically for t:

$$\frac{N_l(\theta)}{N_s(\theta)} = \frac{I_l \times \rho_l \times \frac{d\sigma_l}{d\Omega} \times \Lambda_l(E_l) \times cos\theta}{I_s \times \rho_s \times \frac{d\sigma_s}{d\Omega} \times \Lambda_s(E_s) \times cos\theta} \times \frac{\left(1 - exp\left(\frac{-t}{\Lambda_l(E_l) \times cos\theta}\right)\right)}{\left(exp\left(\frac{-t}{\Lambda_l(E_s) \times cos\theta}\right)\right)} \quad (11)$$

# CHAPTER 3. PALLADIUM NANOPARTICLE FORMATION ON TIO2(110) BY THERMAL DECOMPOSITION OF PALLADIUM(II) HEXAFLUOROACETYLACETONATE

## 3.1 Abstract

Palladium nanoparticles were synthesized by thermal decomposition of palladium(II) hexafluoroacetylacetonate ($Pd(hfac)_2$), an atomic layer deposition (ALD) precursor, on a $TiO_2(110)$ surface. According to X-ray photoelectron spectroscopy (XPS), $Pd(hfac)_2$ adsorbs on $TiO_2(110)$ dissociatively yielding $Pd(hfac)_{ads}$, $hfac_{ads}$, and adsorbed fragments of the hfac ligand at 300 K. A (2 × 1) surface overlayer was observed by scanning tunneling microscopy (STM), indicating that hfac adsorbs in a bidentate bridging fashion across two Ti 5-fold atoms and Pd(hfac) adsorbs between two bridging oxygen atoms on the surface. Annealing of the $Pd(hfac)_{ads}$ and $hfac_{ads}$ species at 525 K decomposed the adsorbed hfac ligands, leaving PdO-like species and/or Pd atoms or clusters. Above 575 K, the XPS Pd 3d peaks shift towards lower binding energies and Pd nanoparticles are observed by STM. These observations point to the sintering of Pd atoms and clusters to Pd nanoparticles. The average height of the Pd nanoparticles was 1.2 ± 0.6 nm at 575 K and increased to 1.7 ± 0.5 nm following annealing at 875 K. The Pd coverage was estimated from XPS and STM data to be 0.05 and 0.03 monolayers (ML), respectively, after the first adsorption/decomposition cycle. The amount of palladium deposited on the $TiO_2(110)$ surface increased linearly with the number of adsorption/decomposition cycles

with a growth rate of 0.05 ML or 0.6 Å per cycle. We suggest that the removal of the hfac ligand and fragments eliminates the nucleation inhibition of Pd nanoparticles previously observed for the $Pd(hfac)_2$ precursor on $TiO_2$.

## 3.2 Introduction

Palladium is used for numerous catalytic applications including carbon–carbon coupling,[49] hydrocarbon hydrogenation and dehydrogenation,[50, 51] hydrocarbon oxidation and combustion,[52, 53] and the purification of automotive exhaust gases.[54] As it was explained in details in section 1.2.2, atomic layer deposition (ALD) has emerged as a technique promising greater control for synthesis of nanometer and sub-nanometer transition metal particles including Pd on oxide supports for heterogeneous catalysis.[16, 18, 19, 55-58] Primarily used to grow thin films, ALD is based on self-limiting surface reactions in which a surface is alternately exposed to different precursors separated by purging inert gas or vacuum, providing atomically-controlled growth.[6] Nanoparticles can be grown on oxide supports during early stages of ALD processes for heterogeneous catalysis applications. Palladium nanoparticles synthetized by ALD using palladium(II) hexafluoroacetylacetonate ($Pd(hfac)_2$) as a Pd precursor demonstrated higher selectivity toward desired products and particle stability compared to traditionally prepared catalysts in reactions such as methanol decomposition,[56] ethanol and isopropanol oxidation,[58] and oxidative dehydrogenation of alkanes.[18]

Formation of the nanoparticles from (hfac)-based organometallic precursor has a nucleation delay and requires a high number of ALD cycles (~100 cycles) that limits its large scale application. Different characterization techniques have been used to isolate the surface intermediates and identify the surface active sites during the initial precursor

exposure. Fourier transform infrared (FTIR) measurements suggested that $Pd(hfac)_2$ decomposes to $Pd(hfac)_{ads}$ and $Al(hfac)_{ads}$ upon adsorption on $Al_2O_3$ and shows nucleation delay period, which was assigned to the possible surface poisoning with $Al(hfac)_{ads}$ species.[21, 55, 59] Using gas-phase infrared spectroscopy Weber et. al suggested that $H_2$+$O_2$ plasma are required to remove the hfac ligands and other carbon moieties left from $Pd(hfac)_2$ adsorption on $Al_2O_3$ substrate.[32]Adsorbed hfac ligands were also suggested to block adsorption sites on $TiO_2$ for the Pt particle formation using $Pt(hfac)_2$ precursor.[60]

In addition to the surface intermediates, the substrate chemistry can also change the growth behavior of the (hfac)-based precursors. The Pd nucleation is faster on ZnO than $Al_2O_3$ at the same conditions. 100 ALD Pd cycles on ZnO yields Pd islands with 10 to 20 nm domains. However, 200 cycles were required to form islands consisting of 10 nm domains on the $Al_2O_3$.[56] X-ray photoelectron spectroscopy (XPS) studies of $Cu(hfac)_2$ adsorption on Pt(111) showed differences compared to the chemistry of $Cu(hfac)_2$ on copper and $TiO_2$. The hfac group formed on copper and $TiO_2$ surfaces remained intact until 373 K and 473 K respectively, while hfac species formed on Pt(111) showed significant decomposition by 300 K.[28, 61] Moreover, the surface contamination prior to deposition has been shown to influence the decomposition pathway and the final structure of nanoparticles. X-ray absorption spectroscopy (XAS) showed, for example, that residual chlorine on the $TiO_2$ surface can participate in the decomposition pathway of $Pd(hfac)_2$. In the presence of chlorine the $Pd(hfac)_2$ decomposed to form $Pd(hfac)Cl_{2ads}$ and $Ti(hfac)_{ads}$ species.[62]

All these studies showed that the initial substrate-$Pd(hfac)_2$ interaction and initial surface intermediates and species are playing a major role in tailoring the final properties of the nanoparticles and the Pd growth behavior. As it has been recently highlighted by Zaera,[34] the fundamental surface science studies can serve as an ideal tool to understand the intermediates involved in the deposition mechanism and elucidate how the overall precursor-substrate interaction process takes place during the initial exposure of the precursor.

In this work, Pd(II) hexafluoroacetylacetonate ($Pd(hfac)_2$), was used for synthesis of Pd nanoparticles on the $TiO_2$(110) surface. In order to understand the surface chemistry and to improve the synthesis of Pd nanoparticles, the evolution of the organometallic precursor was monitored by surface science characterization techniques such as X-ray photoelectron spectroscopy (XPS) and scanning tunneling microscopy (STM). This chapter is a contribution on the adsorption and decomposition pathways of $Pd(hfac)_2$ on $TiO_2$(110) surface.

## 3.3 Experimental Methods:

### 3.3.1 UHV Instruments

Experiments were performed in two separate UHV systems. An Omicron Surface Analysis Cluster at Birck Nanotechnology Center (BNC), Purdue University. The second experimental apparatus at the Center for Nanoscale Materials, Argonne National Laboratory, was an Omicron VT SPM system equipped with a variable temperature STM/AFM (Omicron VT-SPM XA), a preparation chamber for dosing ALD precursors through a leak valve, an $Ar^+$ sputtering gun, and resistive sample heating. STM images were obtained using etched W tips. STM images were analyzed using WSxM software.[63] Pymol software (version 1.5.0.4) was used for molecular visualization.[64]

$TiO_2$(110) single crystals of 9 mm diameter and 1 mm thickness (Princeton Scientific Corp.) were used. In both systems, the sample cleaning procedure consisted of repeated cycles of $Ar^+$ sputtering and vacuum annealing at 925 K. For the XPS study, sample temperature was measured by a K-type thermocouple spot welded to the stainless steel back plate, and crystal cleanliness was monitored by XPS and LEED. Upon $Pd(hfac)_2$ exposure the observed LEED pattern was not stable (disappeared in less than 5 s) due to the decomposition of the precursor caused by electron bombardment from the electron gun and, therefore, is not used.[65] The appearance of the fresh crystal changed from transparent to light blue following several cleaning cycles, the signature of a slightly reduced crystal.[66]

$TiO_2$(110) crystals were exposed to Pd(II) hexafluoroacetylacetonate ($Pd(hfac)_2$) (Aldrich, 99.9%) in the preparation chambers of both systems. For the XPS experiment, dosing was performed for 10 min. at a pressure of ~$5 \times 10^{-7}$ mbar for an exposure of 225 L to ensure

saturation. Higher exposures of $Pd(hfac)_2$ did not change surface Pd coverage. Dosing pressure was determined during a test experiment, and the ion gauge was kept off during $Pd(hfac)_2$ exposure to avoid electron-induced decomposition of $Pd(hfac)_2$. Dosing lines were heated overnight at 423 K, and the lines were filled with $Pd(hfac)_2$ and pumped by a turbo pump for several times before dosing. For the STM experiment, the maximum achievable $Pd(hfac)_2$ base pressure was much lower (~$4 \times 10^{-9}$ mbar) due to system geometry differences, however, the sample sat ~ 2 in. away from a dosing capillary aimed at the sample. $Pd(hfac)_2$ was dosed at approximately this pressure for 60 min. to ensure saturation.

XPS data were acquired using a non-monochromatic Mg Kα X-ray source (hν = 1253.6 eV) at 150 W. High resolution spectra were recorded at a constant pass energy of 20 eV. The resolution, defined as the full-width at half-maximum (FWHM) of the Ti $2p_{3/2}$ peak, was approximately 1.1 eV. Slight sample charging was corrected by fixing the Ti $2p_{3/2}$ peak at 459.3 eV.

XPS data were analyzed with CasaXPS (version 2313Dev64) software.[67] Curve fitting was done assuming a Gaussian/Lorentzian line shape (30% Lorentzian, CasaXPS function: SGL(30)) for symmetric peaks and an asymmetric Lorentzian shape (CasaXPS function: LF(1,1.5,25,70)) for asymmetric peaks.

### 3.3.2 Coverage calculations

The detail of the coverage calculations is presented in section 2.5. XPS coverage and thickness model derivation section.

The required parameters for coverage calculation using Equation 8 can be found in the Table 3.1.

Table 3.1 The XPS parameters used for the quantification

| | |
|---|---|
| Name of solid | $TiO_2$ (110) |
| XPS Source | Mg Kα |
| Transition | Ti 2p |
| Density, $g/cm^3$ | 4.23 |
| Kinetic energy, eV | 795.0 |
| Inelastic mean free path (Å) | 17.8 |
| Transport mean free path (Å) | 60.8 |
| Emission angle, θ (degree) | 45 |
| Asymmetry parameter | 1.45 |
| Practical EAL (L) for a film thickness of 30 Å (Å) | 14.7 |
| $d_s$ (Å) | 3.24 |

## 3.4 Results

### 3.4.1 X-ray photoelectron spectroscopy

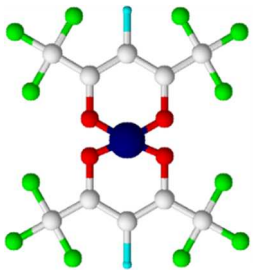

Figure 3.1. Ball and stick schematic of $Pd(hfac)_2$ molecule (Pd atom: blue, O atoms: red, C atoms: white, F atoms: lime, H atoms: cyan).

The structure of $Pd(hfac)_2$ is shown in Figure 3.1. Figure 3.2 shows XPS spectra of the F 1s, O 1s, Pd 3d and C 1s core-levels obtained after saturation exposure of the $TiO_2$(110) surface to $Pd(hfac)_2$ at 300 K. The main component of the F 1s peak is at 688.3 eV and represents a $CF_3$ functional group in hfac ligand. The minor F 1s peak detected at 684.9 eV is assigned to Ti-F.[68] The O 1s spectrum was fitted with two components at 530.6 and 532.1 eV. The former peak is a feature of $TiO_2$, and the latter represents oxygen atoms in the hfac ligand. Supporting this assignment, heating the sample to 575 K causes hfac ligands to decompose (discussed below), and the peak at 532.1 eV is absent. The same peak was observed following adsorption of $Cu(hfac)_2$ on the $TiO_2$ surface.[28] Palladium is represented by a single broad Pd $3d_{5/2}$ peak (FWHM = 1.6 eV) at 336.9 eV. The observed binding energy (BE) is slightly higher than 336.6 eV, which is the reference value for PdO (see for instance reference [69] and references therein). Intact $Pd(hfac)_2$ adsorbed in multilayers on copper substrate is characterized by a Pd $3d_{5/2}$ peak at 339.1 eV,[70] therefore, the component at 336.9 eV was assigned to a palladium atom in a $Pd(hfac)_{ads}$

species. This assignment is further confirmed by the XPS quantification and STM images as will be discussed later.

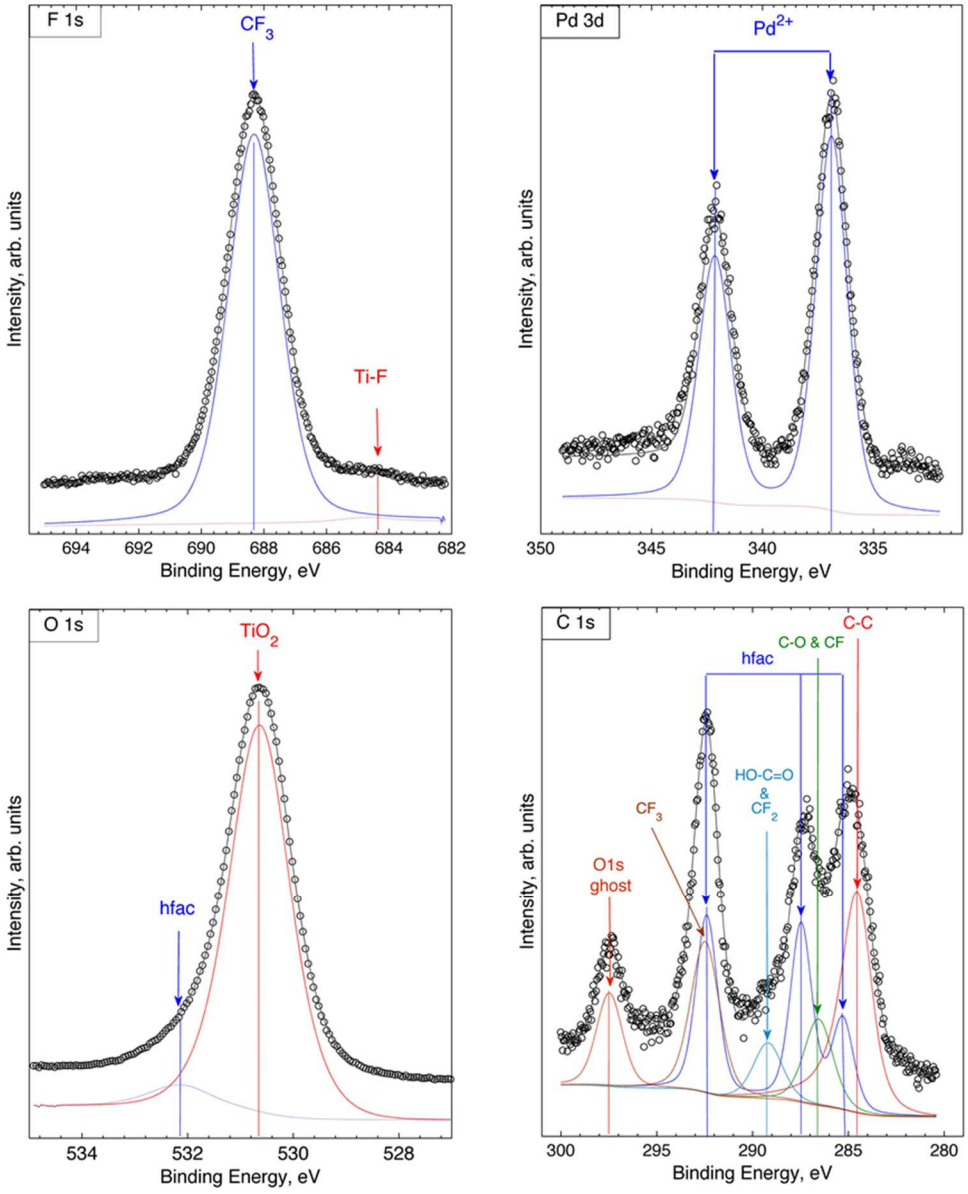


Figure 3.2. The F 1s, O 1s, Pd 3d and C 1s photoemission spectra obtained after exposure of the $TiO_2$(110) surface to $Pd(hfac)_2$ up to saturation at 300 K.

Analysis of the C 1s region revealed contributions from several species. The first is an hfac species, which is characterized by three components, each representing a distinct chemical state of the carbon atoms in hfac (see Figure 3.1). These components at 285.2, 287.5 and 292.4 eV were assigned to carbon atoms in C-H, C=O and $CF_3$, respectively. Our assignments are based on Hantsche,[71] and these values are in good agreement with those observed for $Cu(hfac)_2$ and $Pd(hfac)_2$.[30, 70, 72-74] Characteristic BEs are summarized in Table 3.2.

Table 3.2 Characteristic XPS features observed after $Pd(hfac)_2$ adsorption at room temperature and its subsequent thermal decomposition.

| Species | Binding Energy, eV | | | | |
|---|---|---|---|---|---|
| | C 1s | F 1s | Pd $3d_{5/2}$ | O 1s | Ti $2p_{3/2}$ |
| $Pd(hfac)_{ads}$ | 285.2 (C-H)<br>287.5 (C=O)<br>292.4 ($CF_3$) | 688.3 | 336.9 | 532.1 | - |
| $TiO_2$ | | | | 530.6 | 459.3 |
| Cracked fragments of $Pd(hfac)_2$ | | | | | |
| $CF_3$ | 292.5 | 688.3 | | | |
| $CF_2$, HO-C=O | 289.2 | | | | |
| CF, CO | 286.4 | | | | |
| C-H, C-C | 284.5 | | | | |
| $TiF_x$ | - | 684.9 | - | - | |
| $PdO_x$ and Pd NPs | | | 336.2-335.5 | | |
| Artifact | | | | | |
| O 1s ghost peak from Al Kα | ca 297.5 | | | | |

In order to identify fragments from hfac cracking, the area ratio between the $CF_3$, C=O, and C−H components was constrained to 2:2:1 during curve fitting based on the stoichiometry of the hfac group (Figure 3.1). As shown in Figure 3.2, the hfac components alone were not enough for a proper fitting of the C 1s region, therefore other components were added. The highest BE peak at approximately 297.5 eV was an O 1s ghost peak excited by Al Kα radiation (a dual Mg/Al X-ray gun was used). Inclusion of

the O 1s ghost peak in the curve fitting was crucial to ensure correct background subtraction and spectrum deconvolution. The ratio between the O 1s and ghost peak areas was always constant, confirming this assignment. The O 1s ghost peak area was excluded from carbon quantification. The four other components represent decomposition fragments of the hfac group: residual carbon (carbon bonded to carbon and/or hydrogen only) is assigned to the peak at 284.5 eV, the component at 286.4 eV is a feature corresponding to C-F and/or C-O species (carbon bonded to oxygen or fluorine), $CF_2$ and carboxyl groups are characterized by the peak at 289.2 eV, and the peak at 292.5 eV is due to $CF_3$ species. Partial dissociation of the hfac species likely occurs during adsorption. Caution was taken to avoid radiation damage by minimizing exposure to the X-ray flux. Characteristic $Pd(hfac)_2$ core levels (F 1s, C1s, Pd 3d) were collected first followed by Ti 2p and O 1s. However, radiation-induced decomposition of the precursor cannot be ruled out. One of the main signatures of decomposition was the F 1s peak at 684.9 eV, which appeared after longer exposure to X-ray radiation. This feature was closely monitored during the experiments to ensure no beam damage occurs during the XPS acquisition.

The coverage of adsorbed species was calculated using Eq. (1). The F 1s, Pd 3d, and C 1s peak areas represented the adlayer, and the Ti 2p peaks represented the substrate. At room temperature, the adlayer was assumed to consist of $Pd(hfac)_{ads}$ and hfacads species along with fragments of the hfac ligand. To calculate the coverage of $Pd(hfac)_{ads}$ + $hfac_{ads}$, corresponding contributions of these characteristic components were taken from the F 1s, C 1s, and O 1s peaks (hfac components only), which were obtained using the curve fittings shown in Figure 3.2. For Pd, the entire Pd 3d region was used for coverage calculations. The coverages of $Pd(hfac)_{ads}$ + $hfac_{ads}$ based on the F 1s, Pd 3d, and C 1s

regions were equal to 0.10, 0.10 and 0.08 ML at 300 K, respectively. The coverages were normalized to the stoichiometric ratio of Pd:C:F in the $Pd(hfac)_2$ molecule (1:10:12). The other quantification parameters, for instance the ratio between the $CF_3$ carbon component of C 1s and the $CF_3$ fluorine component of F 1s, matched the stoichiometry as well. The equal value between the normalized coverages (~0.1 ML) for the Pd, C, and F showed that the surface species kept the original stoichiometry of the molecule and can consist of $Pd(hfac)_2$ or $Pd(hfac)_{ads}$ + $hfac_{ads}$. However, the Pd $3d_{5/2}$ XPS peak at 336.9 eV eliminates the presence of the Pd in $Pd(hfac)_2$ state and allows us to conclude that following $Pd(hfac)_2$ exposure at 300 K, the $TiO_2$(110) surface is covered by the $Pd(hfac)_{ads}$ + $hfac_{ads}$ species at a coverage of approximately 0.1 ML. Cracked fragments of hfac such as C-H, C-C, C-F, C-O, $CF_2$, carboxyl groups, and $CF_3$ species were also present on the surface.

The effect of temperature on $Pd(hfac)_2$ adsorption was investigated by exposing the $TiO_2$(110) surface to $Pd(hfac)_2$ at 300, 375 and 450 K. For increasing adsorption temperatures, the extent of fragmentation of the $hfac_{ads}$ and $Pd(hfac)_{ads}$ species increased. At 300 K, the symmetric F 1s peak at 688.3 eV represents the $CF_3$ functional group in hfac ligand. With increasing adsorption temperature, a peak at 684.9 eV grows, which is the signature of the Ti-F bond (Figure 3.3).[68] The maximum concentration of Ti-F occurred at 450 K due to the thermal decomposition of the hfac ligand. At 300 K, a single chemical state of palladium as $Pd(hfac)_{ads}$ was observed at 336.8 eV, but a new Pd $3d_{5/2}$ peak at 336.2 eV appeared following adsorption at 375 and 450 K (Figure 3.3).

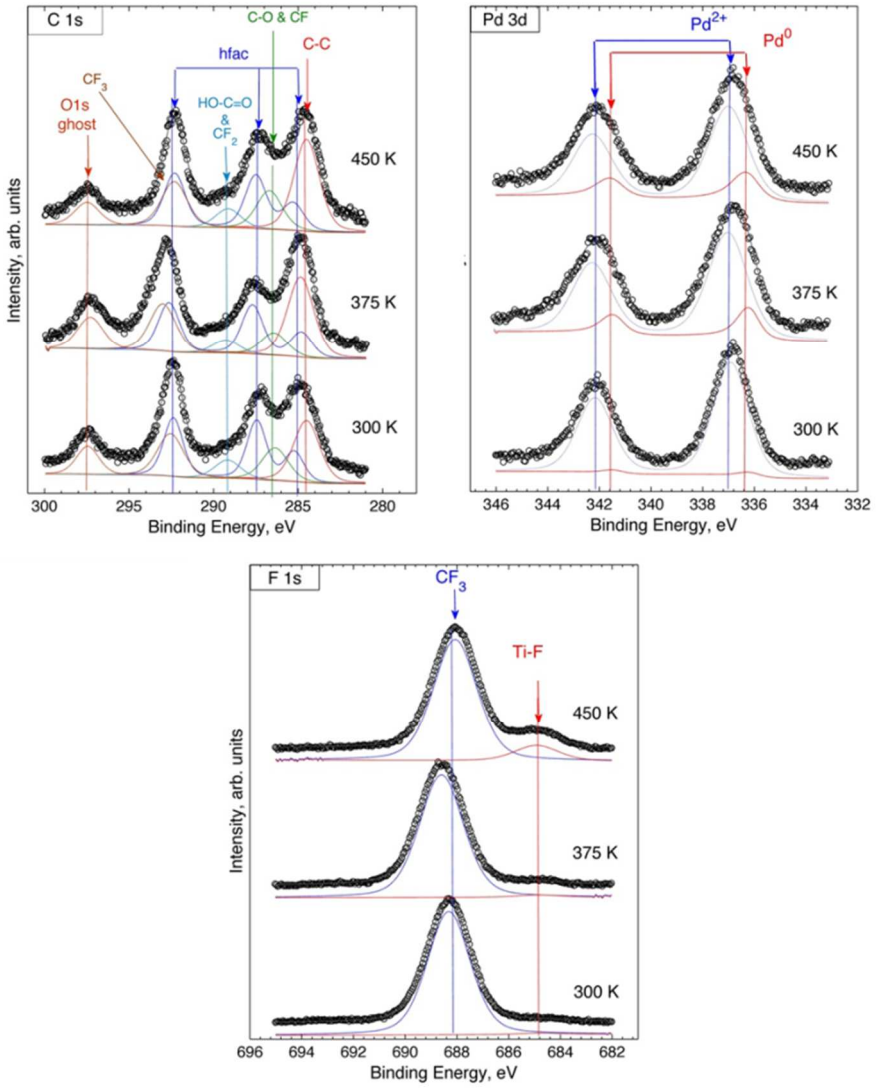


Figure 3.3. The F 1s, Pd 3d and C 1s photoemission peaks obtained after $Pd(hfac)_2$ adsorption on the TiO2(110) surface at 300, 375 and 450 K.

The appearance of this peak could be due to $Pd(hfac)_{ads}$ decomposition and the appearance of a $PdO_x$ ($x < 1$) species and/or Pd clusters. The coverage of the hfac-containing species was calculated using Eq. (1) based on the Pd 3d, C 1s, and F 1s regions and the results are summarized in Table 3.3 and Table 3.4.

Table 3.3. Coverage of hfac species as a function of adsorption temperature

| Adsorption Temperature, K | Coverage, ML, calculated based on | | |
|---|---|---|---|
| | Pd 3d | C 1s (the hfac component only) | F 1s (the hfac component only) |
| 300 | 0.10 | 0.08 | 0.10 |
| 375 | 0.11 | 0.09 | 0.08 |
| 450 | 0.12 | 0.09 | 0.10 |

Table 3.4. Coverage for the different C-containing species as a function of adsorption temperature

| Adsorption Temperature | Coverage, ML | | | | |
|---|---|---|---|---|---|
| | C-F+C-O | residual HC | $CF_2$+-HO-C=O | $CF_3$ | hfac |
| 300 K | 0.28 | 0.54 | 0.16 | 0.37 | 0.09 |
| 375 K | 0.23 | 0.65 | 0.15 | 0.39 | 0.09 |
| 450 K | 0.33 | 0.78 | 0.16 | 0.38 | 0.09 |

The observed trend in these calculations demonstrated that (i) the hfac coverage does not change with adsorption temperature, (ii) the extent of hfac cracking increased, and (iii) the amount of palladium increases. The conclusion is that, at elevated adsorption temperatures, some products of $Pd(hfac)_2$ decomposition desorb leaving palladium atoms on the surface. This assumption is supported by the observation of the Pd $3d_{5/2}$ peak at 336.2 eV assigned to a $PdO_x$ species and/or Pd clusters.

Thermal decomposition of the adlayer prepared by exposure of $TiO_2$(110) to $Pd(hfac)_2$ at 300 K was studied by heating in a stepwise manner from 375 K to 875 K under UHV. Relevant XPS spectra are shown in Figure 3.4.

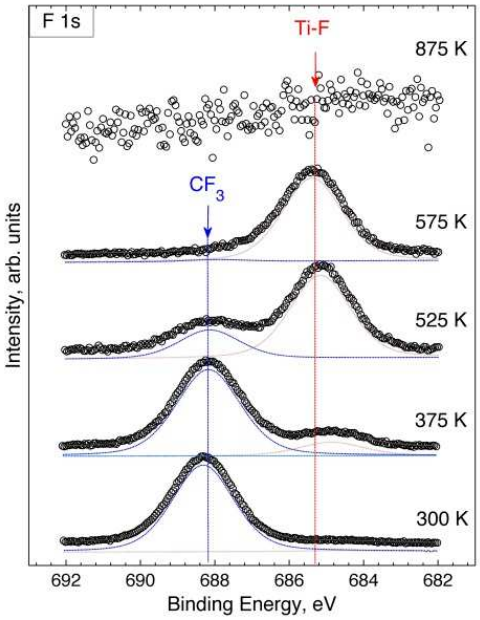


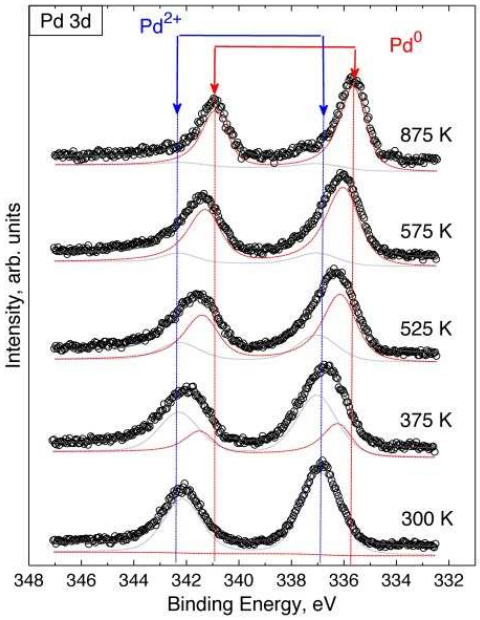

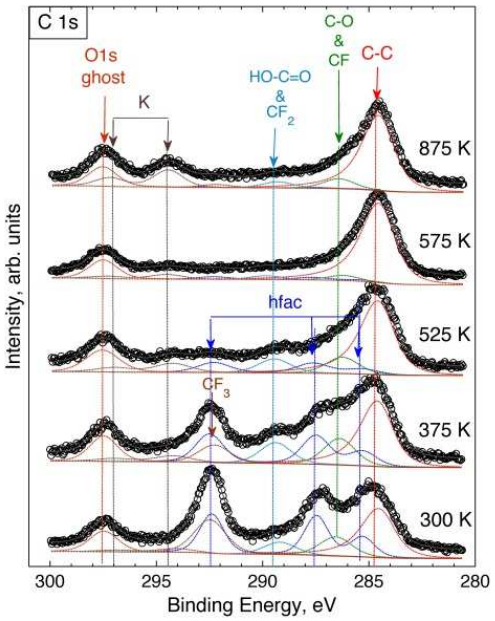


Figure 3.4. The F 1s, Pd 3d and C 1s XPS spectra obtained following $TiO_2$(110) exposed to $Pd(hfac)_2$ at 300 K and heated at 375, 525, 575, 775, 875 K. The spectra were collected at the specified temperature.

Following heating at 575 K, the $CF_3$ species represented by the F 1s peak at 688.3 eV was replaced by the Ti-F species, represented by the F 1s peak at 684.9 eV. The Ti-F species decomposed completely following heating at 875 K. In the Pd 3d region, heating to 375 K resulted in the appearance of a Pd $3d_{5/2}$ peak at 336.2 eV, which was assigned to a $PdO_x$ ($x < 2$) species and/or Pd clusters and/or atoms. The intensity of the $Pd(hfac)_{ads}$ component reached a plateau at 525 K, indicating decomposition of the $Pd(hfac)_{ads}$ species (see Figure 3.4 and Figure 3.5)

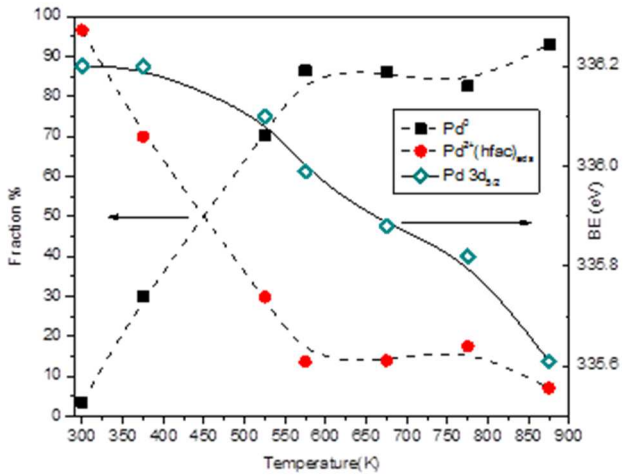


Figure 3.5. Changes of the palladium chemical state upon heating in UHV. The original adlayer was prepared by exposure of the $TiO_2$(110) surface to $Pd(hfac)_2$ at 300 K.

At 775 K, the Pd $3d_{5/2}$ peak is at 335.8 eV. This BE is too low to be assigned to a $PdO_x$ species,[69] therefore, we assume that the $PdO_x$ species decomposed. However, this BE is too high for bulk metallic Pd, which is characterized by a Pd $3d_{5/2}$ peak at 335.0 eV.[69] Thus, we conclude that this shift to higher binding energy is caused by size effect in Pd metal nanoparticles which give shifts to higher BE because of incomplete final state relaxation.[75] With increasing temperature, the Pd $3d_{5/2}$ peak at 335.8 eV shifted towards lower BE and reached 335.6 eV following annealing at 875 K. The BE shift towards lower binding energies observed between 775 and 875 K is assigned to a sintering effect that partially removes the final state relaxation limitation.

Thermal decomposition of adsorbed hfac-containing species and the transformation of its dissociation fragments were traced by monitoring the coverages of different carbon species during annealing (Figure 3.4 and Figure 3.6).

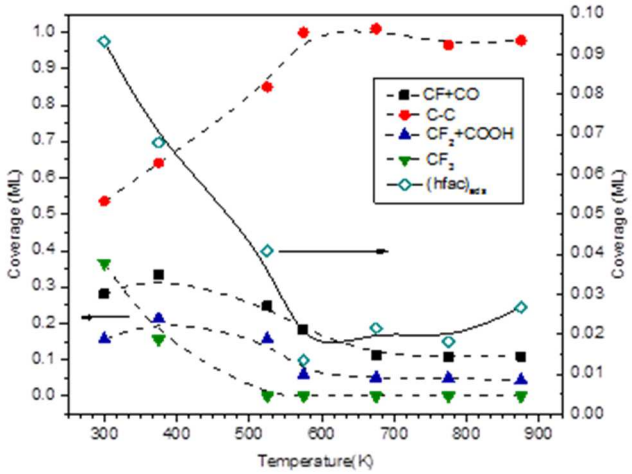


Figure 3.6. Coverage of carbon species observed during heating in UHV. The corresponding XPS spectra are shown in Figure 3.4. The points with dashed lines are belonging to the left side y-axis.

Coverages were calculated using Eq. (1). The $Pd(hfac)_{ads}$ species fully decomposes at 525 K, in agreement with the conclusion reached based on the evolution of the Pd 3d spectra (Figure 3.4). $CF_3$ fragments associated with the decomposition of the hfac ligand follow the same trend and, therefore, have thermal stability similar to $Pd(hfac)_{ads}$. The $CF_2$, carboxyl, and CF species are likely intermediates of $Pd(hfac)_{ads}$ or $hfac_{ads}$ decomposition. $CF_2$ and CF species might form through decomposition of $CF_3$ by transfer of fluorine atoms to $TiO_2$(110). Above 575 K, the carbon species related to hfac groups vanish, and only a single asymmetric peak related to graphitic carbon or other carbon species formed by decomposition of the organic moieties could be detected. The carbon remaining following annealing at 875 K is likely graphitic. Potassium, a bulk crystal contamination, diffuses from the bulk to the surface during annealing at 875 K.

Detailed XPS analysis of surface chemical states also revealed possible adsorption sites for $Pd(hfac)_{ads}$ and $hfac_{ads}$. The clean $TiO_2(110)$ surface was characterized by the Ti $2p_{3/2}$ peak at 459.3 eV, which is a feature of stoichiometric $TiO_2$. An additional Ti $2p_{3/2}$ peak at 457.5 eV assigned to reduced titania, $TiO_x$ ($x < 2$), was also observed.

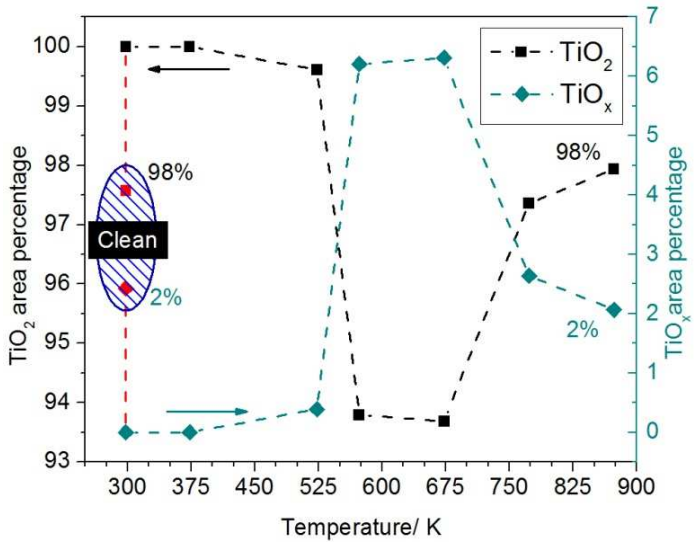


Figure 3.7. Changes in area fraction of $TiO_2$ and $TiO_x$ components upon heating for clean $TiO_2$ (110), $Pd(hfac)_2$ exposure at 300 K and during annealing to 875 K. The shaded area shows the fractions of $TiO_2$ and $TiO_x$ for the clean $TiO_2$ (110) single crystal before the $Pd(hfac)_2$ exposure.

The evolution of the $TiO_x$ and $TiO_2$ components is shown in Figure 3.7. The $TiO_x$ component disappears following $Pd(hfac)_2$ adsorption. However, the $TiO_x$ peaks reappeared upon heating to 525 K, the same temperature at which the $Pd(hfac)_{ads}$ and $hfac_{ads}$ species decomposed. This suggests that the reduced titania centers are involved in $Pd(hfac)_2$ adsorption and/or dissociation. The oxygen atoms of the hfac ligand might interact with the reduced $TiO_x$ centers providing oxygen needed for a fully oxidized

surface. Following decomposition of the $hfac_{ads}$ ligands at 575 K in UHV, the $TiO_x$ area fraction increases to ~6.5% before returning to the original value of ~2% following heating at 875 K The increase of the $TiO_x$ contribution at 575 K might be due to the reaction of the surface oxygen from stoichiometric $TiO_2$ with carbon fragments from the hfac ligands. Heating to 875 K results in the diffusion of the oxygen vacancies to the bulk and return of the surface to its initial state.

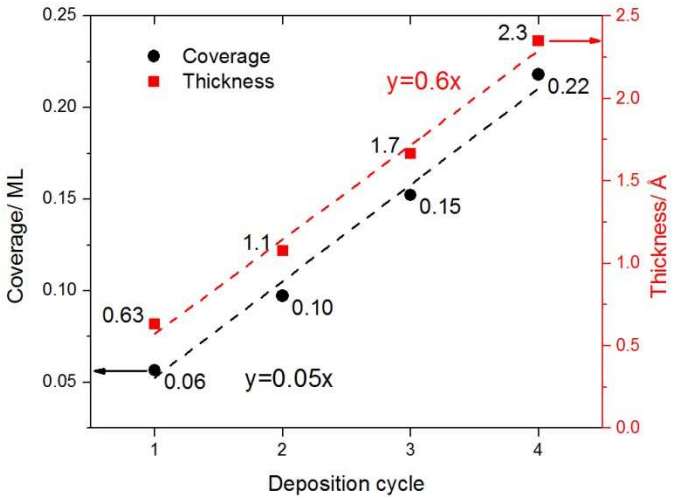


Figure 3.8. Pd growth curve showing the coverage of the Pd in ML versus number of deposition cycles. Each cycle consist of adsorption of $Pd(hfac)_2$ at 300 K followed by annealing in UHV to 875 K.

The number of $Pd(hfac)_2$ adsorption and decomposition cycles on the $TiO_2(110)$ surface determines the amount of the deposited Pd. Palladium coverages and palladium layer thicknesses are shown in Figure 3.8 for four consecutive cycles of $Pd(hfac)_2$ adsorption at 300 K followed by heating to 875 K in UHV. XPS spectra for consecutive cycles are similar to those for the first deposition cycle. In addition to the Pd coverage, the thicknesses are presented for comparison with the value of growth per cycle (GPC) for

$Pd(hfac)_2$ ALD measured by quartz crystal microbalance (QCM), which assumes formation of a uniform overlayer after each cycle. Similarly, we have used a uniform Pd overlayer XPS quantification model. Growth is linear with a GPC of 0.6 Å (Figure 3.8). Therefore, the amount of deposited palladium can be controlled by the number of adsorption and decomposition cycles. The linear growth of Pd indicates that the remaining graphite-like carbon does not block adsorption sites for $Pd(hfac)_2$.

### 3.4.2 Scanning tunneling microscopy

To complement the XPS results with topography data, an STM investigation was performed. A typical 100 × 100 nm STM image of the clean $TiO_2$ (110) surface following the preparation procedure described in the experimental section is shown in Figure 3.9A. Irregularly-shaped terraces are present, as are defect sites that show up as bright spots and added rows. The spots might be oxygen vacancies or other defect types, and the added rows act as precursors for the $TiO_2$(110)-(1×2) surface reconstruction.[76] The measured step height was approximately 3.2 ± 0.2 Å, in agreement with the expected value of 3.24 Å for rutile $TiO_2$(110). Alternating bright and dark rows running along the [001] direction are visible. The spacing between bright rows and between dark rows in the $[1\bar{1}0]$ direction is approximately 6.5 Å. Within bright rows, the spacing between features was approximately 3 Å. Atomic resolution data after Fourier transform filtering is shown in the inset in Figure 3.9A with the dimensions labeled. These dimensions correspond to a bulk terminated $TiO_2$(110)-(1×1) surface, where the bright features are attributed to surface 5-fold Ti atoms and the dark features to bridging oxygen atoms.[76]

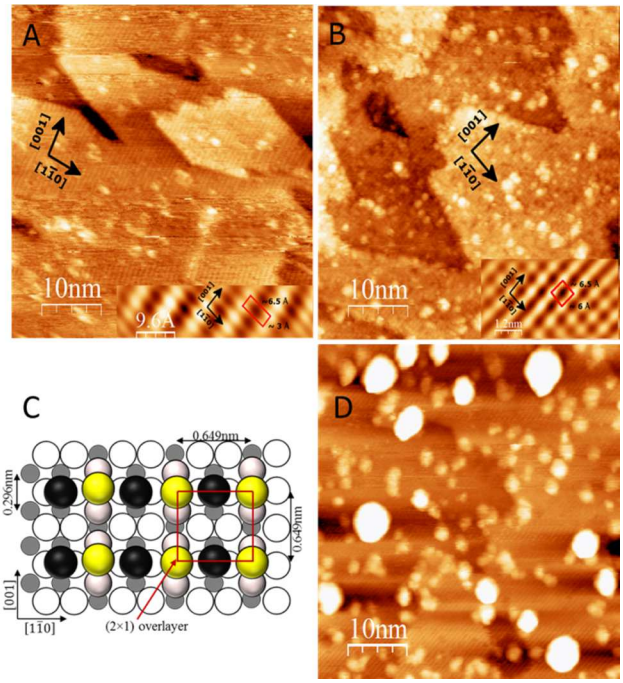


Figure 3.9. STM images of the $TiO_2$(110) surface. A: Clean $TiO_2$(110) following sputtering and annealing cycles (V = +2.0 V, I = 70 pA). Inset: Atomic scale image after Fourier transform showing the unreconstructed (1 × 1) unit cell. B: $TiO_2$ following dosing of $Pd(hfac)_2$ for 60 min. at room temperature (V = +1.75 V, I = 0.1 nA). Inset: Small scale image after Fourier transform showing structured (2 × 1) overlayer of adsorbates. The bright spots are assigned to $Pd(hfac)_{ads}$ group. C: Model for $Pd(hfac)_2$ adsorbed on $TiO_2$(110): The $Pd(hfac)_2$ dissociates. The resulting hfac (hfac: black spheres) binds to two five-fold coordinated Ti atoms (gray spheres) in a bi-dentate fashion and the Pd(hfac) (Pd(hfac): yellow spheres) adsorbed between two bridging oxygen (oxygen: white spheres). The adsorption geometry matches the experimental value reported in image B inset. D: Following annealing of the as-deposited sample to 875 K for 20 min (V = +0.5 V, I = 2.0 nA).

A 100×100 nm image following saturation dosing of $Pd(hfac)_2$ at RT is shown in Figure 3.9B. This surface is characterized by bright clusters with similar approximate size and density as the defect sites on the clean $TiO_2$, and bright, discontinuous rows running along the [001] direction with inter-row spacing of approximately 6.5 Å. Though the discontinuities could not be resolved in all images, a Fourier transform of an area containing discrete features revealed their spacing along a row in the [001] direction to be approximately 6 Å (inset, Figure 3.9B). The dimensions of these dark and bright spots correspond to a structured (2 × 1) overlayer, can be assigned to bidentate bridging hfac ligands bonding through both oxygen atoms to two 5-fold Ti atoms, and $Pd(hfac)_{ads}$ with Pd bonding to two surface bridging oxygen atoms shown schematically in the ball model in Figure 3.10. The contrast in the STM images allows for a model for the identity of the adsorption species and adsorption sites: Pd(hfac), if bound between two bridging oxygen atoms, would protrude further from the surface than an hfac ligand bound to two 5-fold coordinated Ti atoms, and would therefore appear brighter on the basis of topography. Based solely on topography, then, the adsorbed hfac ligands would appear as the dark spots also in a (2 × 1) arrangement. The contrast may also be explained by electronic arguments. For example, the appearance of dark and bright areas was reported in the STM images of the Si(111)-(7×7) surface exposed to $Cu(hfac)_2$.[77] Based on the bias dependence, dark areas were assigned to hfac ligands and the bright regions to Cu atoms when empty electronic states of the sample were tested at positive bias voltage. The STM images shown in Figure 3.9 were obtained at positive biases. Therefore, hfac ligands might appear as the dark rows. The $Pd(hfac)_{ads}$ species is expected to have a higher

density of states above the Fermi level than those for the $hfac_{ads}$ group, leading to the $Pd(hfac)_{ads}$ species appearing as the bright spots (Figure 3.9B).

This proposed model in Figure 3.10 is in agreement with, observed a (2 × 1) overlayer following dosing of $Cu(hfac)_2$ on $TiO_2(110)$.[28, 78] The authors of that study noted that the distance of the two oxygen atoms in the hfac ligand of $Cu(hfac)_2$ is 2.79 Å, close to the distance of 2.96 Å between two 5-fold surface Ti atoms on $TiO_2(110)$ that make it suitable adsorption site for hfac structure. This is close to the value of 2.77 Å between two O atoms in an hfac ligand in $Pd(hfac)_2$.[79]

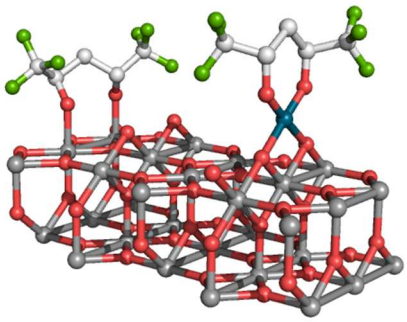

Figure 3.10. $Pd(hfac)_2$ molecule adsorbed on the $TiO_2(110)$ surface at room temperature. $Pd(hfac)_2$ molecule dissociates into a $hfac_{ads}$ ligand, which bonds across neighboring 5-fold coordinated Ti sites (grey atoms), and a Pd(hfac), which bonds across bridging O atoms (red atoms) on the surface. The continuous row of Pd(hfac) adsorbed species can be responsible for the (2 × 1) structure observed after $Pd(hfac)_2$ adsorption at room temperature. The adjacent Pd(hfac) and hfac groups are not shown for clarity.

Following annealing at 575 K, nanoparticles appeared with an average height of 1.2 ± 0.6 nm (see Figure 3.11), where the error is one standard deviation from the average value.

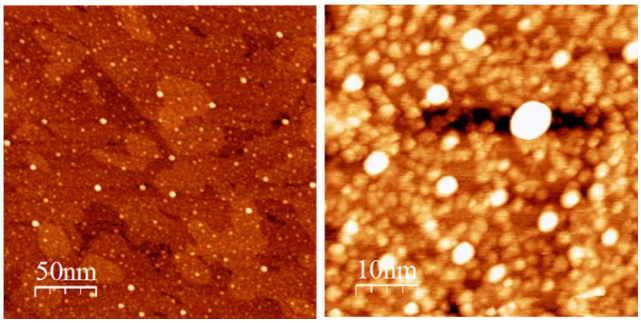


Figure 3.11. STM images (left: 200 nm×200 nm, right: 50 nm×50 nm) of the $TiO_2$(110) surface exposed to $Pd(hfac)_2$ at 300K and annealed at 575 K in UHV ($U_t$ = +0.8 V, $I_t$ = 1.0 nA). The Pd average particle height is 1.2 ± 0.6 nm.

Uncertainty in the height distribution arises from the difficulty in determining which features are Pd nanoparticles, which are agglomerations of ligand fragments, and which are original defects in the $TiO_2$ surface. The best quality images were obtained at higher tunneling current and lower bias ($V_{bias}$ =0.8 V $I_t$ =1.0 nA) than for the previous experiment, indicating that surface conductivity had increased. This might be due to the formation of Pd nanoparticles.

Annealing at 875 K resulted in the agglomeration of the nanoparticles, and the unreconstructed $TiO_2$(110)-(1 × 1) surface reappeared as shown in Figure 3.9D. These results agree with the XPS data, which demonstrated the complete decomposition of the $(hfac)_{ads}$ species at 575 K and Pd nanoparticle sintering at 875 K. The average height of the nanoparticles was 1.7 ± 0.5 nm at 875 K. Even after annealing to 875 K, the particle size is within the range where a size-dependent BE shift could be observed. Therefore, the + 0.6 eV shift of the Pd $3d_{5/2}$ peak from the peak position for the bulk palladium (335.0 eV) could be assigned to a particle size effect. No preferential nucleation of the Pd

NPs was observed at step edges. The coverage of Pd particles was estimated from the STM data to be 0.03 ML at 875 K. This value is in good agreement with the 0.05 ML calculated using the XPS data. It must be noted that the apparent lateral dimension of these nanoparticles depends on the STM tip shape and, therefore, is not used. The coverage estimation from STM assumes a hemispherical NP shape in which the radius is approximately equal to the height.

## 3.5 Discussion

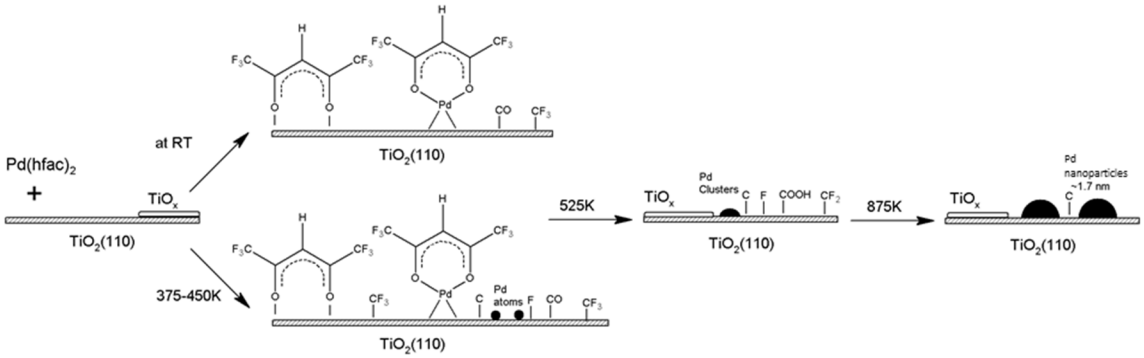


Figure 3.12. Schematic of the reaction of $Pd(hfac)_2$ with a $TiO_2(110)$ surface.

Based on the experimental data, the mechanism shown in Figure 3.12 is proposed for the interaction of $Pd(hfac)_2$ with $TiO_2(110)$. The cleaning procedure of $TiO_2(110)$ causes thermal desorption of surface oxygen leaving behind a partially reduced surface with $TiO_x$ species.[76] Upon adsorption at 300–450 K, the $Pd(hfac)_2$ precursor dissociates to $(hfac)_{ads}$ and $Pd(hfac)_{ads}$ species. Further decomposition of the $(hfac)_{ads}$ and $Pd(hfac)_{ads}$ species occur at 375 and 450 K. The $(hfac)_{ads}$ and $Pd(hfac)_{ads}$ species form a $(2 \times 1)$ surface overlayer. The hfac fragment adsorbs in a bidentate bridging fashion across two Ti 5-fold atoms and Pd(hfac) adsorbs between two bridging oxygen atoms (Figure 3.10). Following $Pd(hfac)_2$ adsorption, the $TiO_x$ species disappeared, showing that $hfac_{ads}$ and its cracked fragments re-oxidize the surface (Figure 3.7). This implies that in a parallel path with the adsorption on Ti 5-fold atoms, the $hfac_{ads}$ species can adsorb on the $TiO_x$ defects and compensate for the lack of oxygen.

Cracked fragments of the hfac ligand were observed at all adsorption temperatures. The degree of hfac decomposition increases with increasing adsorption temperature.

Heating the adsorbed layer resulted in decomposition of the $Pd(hfac)_{ads}$ and $(hfac)_{ads}$ species, which dissociated at approximately 525 K, leaving the cracked hfac fragments and $Pd^0$ clusters (Figure 3.12). The $CF_3$ species underwent decomposition through sequential loss of fluorine atoms, which then bond to titanium. Ti-F species were observed on the surface up to 775 K. No fluorine-containing species were detected at 875 K. Carbon atoms segregate to graphitic-like (C-C) structures at 575 K. The rest of the carbon-containing species partially desorb: the carbon level decreases upon heating until 675 K and then remains unchanged upon further annealing to 875 K. Once the hfac groups thermally decomposed at 525 K, reduced titania appeared on the surface. At 875 K, the level of reduced titania returned to the original level of the clean $TiO_2$(110) surface due to diffusion of surface oxygen vacancies to the bulk (Figure 3.7).

Following annealing at 775 K, the Pd coverage decreased to 0.07 ML indicating sintering of the Pd nanoparticles, which is accompanied by the Pd $3d_{5/2}$ peak shifting towards lower BE. This BE shift is attributed to the formation of larger Pd nanoparticles. It could also be attributed to the encapsulation of Pd nanoparticles by $TiO_x$ species, however, for Pd particle encapsulation to take place, the $TiO_2$ support must first be reduced.[80] Here, the $TiO_x$ component decreases continuously upon annealing to 875 K, which indicates absence of encapsulation in our system. Encapsulated particles also look different in a STM image: the boundary between the particle and support is blurred. This was not case: the particles have a sharp boundary and do not look encapsulated.

Since $hfac_{ads}$ and its cracked fragments can block $Pd(hfac)_2$ adsorption, their removal step is critical for the next deposition cycles. As shown in Figure 3.8, on the surface free of hfac ligands and decomposition fragments, the amount of palladium linearly increases

with the number of deposition cycles. The key factor for linear growth was thermal decomposition and removal of the hfac ligands at 875 K prior to each cycle of the $Pd(hfac)_2$ adsorption. On the other hand, for a real $Pd(hfac)_2$ ALD process, the number of typical ALD cycles required to reach steady-state Pd ALD growth was reported to be between 20 to 100 ALD cycles.[55] QCM measurements for $Pd(hfac)_2$/formalin ALD on $TiO_2$ showed 0.22 Å growth per cycle [21]. This is about 1/3 of the value of 0.6 Å per cycle calculated from our XPS data. The residual fluorine- and carbon-containing contaminations might cause surface poisoning during the first few cycles (see for instance Figure 3 in reference[55]). The contaminations could be a reason for the lower growth per cycle. Surface blocking by $hfac_{ads}$ and its fragment moieties was assumed to be responsible for $Pd(hfac)_2$ nucleation delay on the $Al_2O_3$ and $TiO_2$ surfaces.[21, 55, 59] Following annealing at 875 K, the Pd nanoparticles with average height of 1.7 ± 0.5 nm were obtained. Assuming a hemi-spherical shape of the particle, the average diameter at the base of the particle is 3.4 ± 1.0 nm. The Pd coverage was estimated to be 0.1 ML after $Pd(hfac)_2$ exposure, and 0.03 - 0.05 ML after annealing at 875 K, respectively. Judging from the Pd $3d_{5/2}$ BE shift, the palladium NPs started to sinter above 675 K. The particle size increased from 2.4 ± 1.2 nm at 575 K to 3.4 ± 1.0 nm at 875 K.

## 3.6 Conclusion

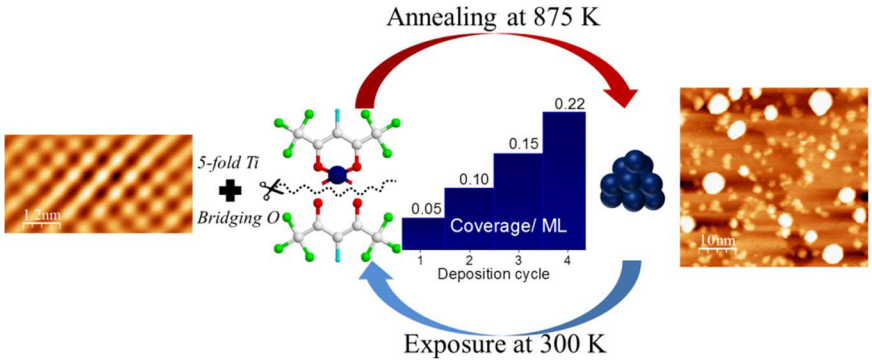


Figure 3.13. Graphical summary of the chapter 3.

The $Pd(hfac)_2$ adsorption is a self-limiting reaction on the $TiO_2(110)$ surface yielding $Pd(hfac)_{ads}$ and/or $hfac_{ads}$ species and partial hfac fragmentation at room temperature. The removal of the hfac ligand and its fragments through thermal decomposition of surface species remove the initial growth delay period and results in linear growth of Pd on the $TiO_2$ surface. The Pd amount linearly increases with the number of adsorption/dissociation cycles with the growth per deposition cycle of about 0.05 ML (0.6 Å) (see Figure 3.13).

# CHAPTER 4. THE SURFACE CHEMISTRY OF TRIMETHYLALUMINIUM (TMA) ON PD(111) AND PT(111)

## 4.1 Abstract

The surface chemistry of trimethylaluminium (TMA), a widely used atomic layer deposition (ALD) precursor, was investigated on Pt(111) and Pd(111) single crystals by using X-ray photoelectron spectroscopy (XPS), high resolution electron energy loss spectroscopy (HREELS), scanning tunneling microscopy (STM), and density functional theory (DFT). Based on the DFT calculations, TMA decomposition to methylaluminum (MA) is thermodynamically favorable on both Pt and Pd (111) terraces. Further dissociation of MA to aluminum and adsorbed methyl groups is limited to step sites. Similarly, Pt and Pd atoms removal from (111) terraces is hindered by high energy barriers of 2.44 and 2.31 eV while surface vacancy formation has lower energy barriers of 1.62 and 1.16 eV on Pt and Pd step edges, respectively. In agreement with DFT calculations, experiments showed that TMA dissociates to aluminum, methyl, and ethylidyne groups on the Pd surface. Pd steps are fully covered with fractal Pd-Al alloy islands that spread over terraces with an average composition of $Pd_{1.4}Al_{1.0}$. Pd hydrogenates and removes carbonaceous species, freeing step sites for MA to Al decomposition. Pd step vacancies serve as nucleation sites for Pd-Al alloy formation. On Pt(111), TMA only decomposed to methylaluminum (MA) and methyl groups. No evidence of Pt-Al alloy formation was observed on the Pt surface. The Pt(111) surface

was uniformly covered with MA and residual carbon species after TMA exposure. On the Pt(111) surface, the residual carbon species were hypothesized to block access to step sites preventing MA to Al dissociation and subsequent alloy.

## 4.2 Introduction

Palladium and platinum are widely used for many heterogeneous catalytic reactions including carbon-carbon coupling,[81] hydrocarbon oxidation,[82] water-gas shift,[83] and environmental pollution control.[84-86] Pd and Pt are the catalysts of choice for hydrogen sensors and fuel cell devices.[87-89] Despite their utility, both metals are prone to deactivation due to particle instability (sintering) and carbon poisoning (coking). Recently, the over-coating of Pd and Pt nanoparticles with alumina films synthesized by atomic layer deposition (ALD) using trimethylaluminium (TMA) and water as precursors has been shown to prevent catalyst deactivation.[7, 16, 18, 19, 90, 91] Among ALD precursors, TMA is the most widely used organometallic precursor, and the TMA-water ALD system is often used for ALD characterization technique development (see for instance reference[4] and references therein).

In this chapter we seek to better understand how TMA interacts with transition metal surfaces. Numerous characterization techniques were used to study the TMA reaction pathway on Pd and Pt surfaces. Density functional theory (DFT) predicted that TMA can catalytically dissociate on bare Pd(111) and Pt(111).[19] Adsorbed methylaluminum (Al-$CH_{3ads}$) and metallic aluminum were found to be the most thermodynamically favorable species remaining on the Pd(111) and Pt(111) surfaces following TMA decomposition. TMA adsorption and alumina overlayer growth mechanisms on Pd and Pt have been studied using quadrupole mass spectrometry (QMS)[18, 19, 55] and quartz crystal

microbalance (QCM).[13, 18] The QCM data suggested that TMA forms a discontinuous film rather than a continuous overlayer and leaves bare patches on the Pd surface. The Pd surface remained available for CO adsorption even after 8 cycles of TMA/water ALD. Based on the QCM measurements, Elam et al.[19] proposed that on Pd(111) $CH_{3ads}$ species block TMA adsorption and can result in non-uniform coverage of the Pd surface by alumina. The authors also suggested that preferential decomposition of TMA occurred on under-coordinated sites such as steps; this might result in non-uniform coverage of alumina on the Pd surface as well.[16]

Probing the interaction between ALD precursors and substrates as well as tracking surface intermediates from ALD processes presents a formidable challenge since ALD is typically performed at millibar gas pressures with precursor exposure times in the range of seconds in flow reactors. Following the fate of carbon, an inevitable species in TMA ALD chemistry due to the attached methyl groups,[19] is needed to understand the interaction of TMA with various substrates. However, this task is difficult using only characterization techniques integrated with the conventional ALD reactor, especially when attempting to distinguish between TMA surface intermediates, adventitious carbon, and other impurities on the surface. Moreover, with application of ultra-thin (< 10 nm) alumina overlayers on heterogeneous catalysts[20] the substrate itself can be one of the ALD reactants that needs to be probed during the ALD growth. As highlighted by Zaera[34] in his recent review, surface sensitive characterization techniques in controlled environments can help increase understanding of ALD surface chemistry and provide solution to the above challenges.

In this chapter, we investigated TMA adsorption on Pd(111) and Pt(111) surfaces using scanning tunneling microscopy (STM), X-ray photoelectron spectroscopy (XPS), high resolution electron energy loss spectroscopy (HREELS), and density functional theory (DFT). This study highlights the effect of the different carbon-containing groups on morphology and overlayer composition. TMA interaction with Pd(111) and Pt(111) during the first ALD half-cycle determines the final structure and morphology of the alumina over-layer on Pt and Pd surfaces.

## 4.3 Experimental Methods

Experiments were performed in an Omicron Surface Analysis Cluster at Birck Nanotechnology Center (BNC) consisting of ultra-high vacuum (UHV) preparation and μ-metal analysis chambers with base pressures of $1\times10^{-9}$ mbar and $5\times10^{-11}$ mbar, respectively. The preparation chamber was equipped with a mass spectrometer, an $Ar^+$ sputtering gun, electron beam bombardment heating, STM tip conditioning stage, internal bakeout system (stab-in heaters using quartz IR lamps), and leak valves connected to two gas manifolds for ALD precursor dosing. The analysis chamber was equipped with XPS, LEED, HREELS, and STM. Samples were heated resistively in both chambers. Sample temperature was measured with a K-type thermocouple attached to the sample holder.

STM images were obtained using an Omicron ambient temperature UHV STM/AFM in constant current (topographic) mode. Electrochemically etched W tips conditioned by electron bombardment were used. Images were analyzed using the WSxM v3.1 software.[63] STM images were used as a method to determine the fractal dimension ($d_p$) based on the perimeter and area of observed islands. The $d_p$ value, depends on the chosen yardstick length (i.e. size of a pixel) used to measure perimeter of the fractal islands (P). The yardstick value (δ) is obtained by dividing total area scanned by the number of pixels in each image to be δ=0.15nm. We have considered only islands with an area greater than $\sim200\delta^2$ in our analysis.[92]

HREELS spectra were acquired using an ELS5000 instrument (LK Technologies) in the specular direction with primary beam energy of 5.0 eV. The full width at half maximum (FWHM) of the elastic peak was usually ~2.8 meV (~23 $cm^{-1}$). The intensity of an elastic

peak was above $10^5$ cps. For intensity comparisons, all HREELS spectra have been normalized to the elastic peak intensity.

XPS data were acquired using a non-monochromatic Mg Kα X-ray source (hν = 1253.6 eV) at 150 W. High resolution spectra were recorded at a constant pass energy of 20 eV. The resolution of the instrument, reported as the FWHMs of the Pd $3d_{5/2}$ and Pt $4f_{7/2}$ peaks of clean Pd(111) and Pt(111) crystals, was approximately 1.2 eV. Photoelectrons were collected at a 45° angle with respect to the surface normal.

XPS data were analyzed with CasaXPS (version 2313Dev64) software. Metallic Pt, Pd, and Al components, along with graphitic/carbidic C components, were fit using an asymmetric Gaussian/Lorentzian line shape with tail dampening (CasaXPS Line shape = LF(1,1.8,30,90)). Nonmetallic species of C and Al were fit with symmetric Gaussian/Lorentzian line shapes (CasaXPS Line shape = GL(10) or SGL(10)). Doublets arising from spin-orbit coupling in the Pt 4f ($4f_{7/2}$ and $4f_{5/2}$), Pd 3d ($3d_{5/2}$ and $3d_{3/2}$), and Al 2p ($2p_{3/2}$ and $2p_{1/2}$) regions were subject to spacing constraints of 3.33, 5.26, and 0.43 eV, respectively.[93] Area ratios for spin-orbit coupling doublets were kept constrained, and FWHMs of these spin-orbit coupling doublets were constrained to be equal. To quantify the XPS result, we followed Fadley's approach,[94] which assumes a non-attenuating adlayer at fractional coverage which is described in details in section 2.5.

Pd(111) and Pt(111) single crystals with 9.0 mm diameter and 1.0 mm thickness (MaTecK) with orientation accuracy of < 0.5° were used. The single crystals were cleaned by repeated cycles of $Ar^+$ sputtering and annealing in vacuum at 1000 K and in oxygen at 623 K. Cleanliness was monitored by XPS, LEED and HREELS.

The single crystals were exposed to TMA (Aldrich, 97%) in the preparation chamber via a leak valve. Prior to dosing TMA, several cycles of freeze-pump-thaw were performed for purification. Dosing lines were heated overnight at 423 K, and the lines were filled with TMA and pumped several times before dosing. The empty preparation chamber was exposed to TMA before dosing to a single crystal for each experiment in order to passivate the chamber walls. Exposures are reported in Langmuir (L, 1 L = $1 \times 10^{-6}$ Torr s), and are calculated from uncorrected ion gauge measurements. The ionization gauge was left on during TMA dosing, but this did not affect the state of the deposited material. Reported exposure values are estimates because decomposition of TMA on the walls of the chamber depends on the history of gas exposures, and this might cause errors in reported exposure values especially at low TMA exposures.

DFT calculations were performed by Vienna ab initio simulation package (VASP)[98] using project augmented wave (PAW)[99] potential and PW91 exchange-correlation functional.[100] The plane wave cutoff of 400 eV was used. The optimized lattice constants of bulk Pd and Pt are 3.956 and 3.985 Å, respectively. The four-layer slabs were used to model (111) and (211) surfaces with (2×2) and (1×3) unit cells, respectively. To prevent the artificial interaction between the repeated slabs along z-direction, 12 Å vacuum was introduced with correction of the dipole moment. A (4×4×1) k-point mesh was used to sample the Brillouin zone. The bottom two layers were fixed and the remained atoms and adsorbates were relaxed until the residual forces were less than 0.02 eV/Å. The transition states and reaction barriers were searched by the climbing-image nudged elastic band (CI-NEB) method.[101]

## 4.4 Results

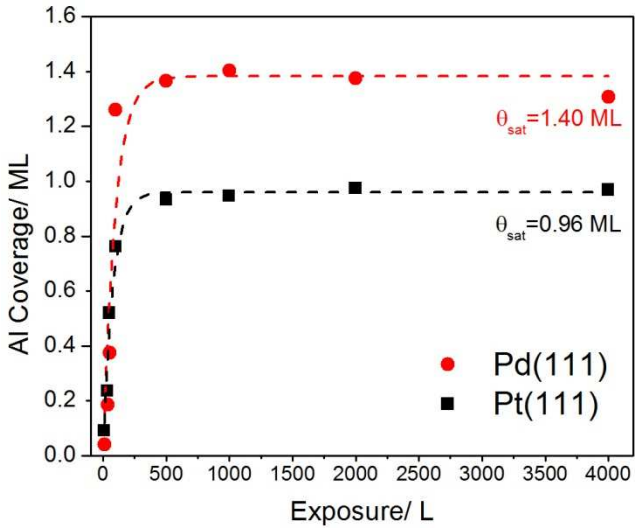


Figure 4.1. Aluminum coverage (ML) on Pd(111) and Pt(111) surfaces versus TMA exposure in Langmuir (L) at 473 K. The dashed lines serve as the guidance to the eye.

To verify that the amount of Al deposited during one ALD half cycle reached saturation under high vacuum dosing conditions (i.e., that TMA is an ALD precursor in high vacuum), Pd(111) and Pt(111) surfaces were exposed to TMA at 473 K, and Al coverage was calculated from XPS data using a non-attenuating adlayer model. Figure 4.1 shows the Al coverage in monolayers (ML) versus TMA exposure for Pd(111) and Pt(111) surfaces. At exposures up to about 500 L the Al coverage increased rapidly on both surfaces before reaching a plateau at higher exposures. The saturation coverages of Al ($\theta_{sat}$) were 1.40 and 0.96 ML on the Pd(111) and Pt(111) surfaces, respectively, demonstrating the self-limiting nature of the reaction between TMA and Pd(111) and Pt(111) surfaces.

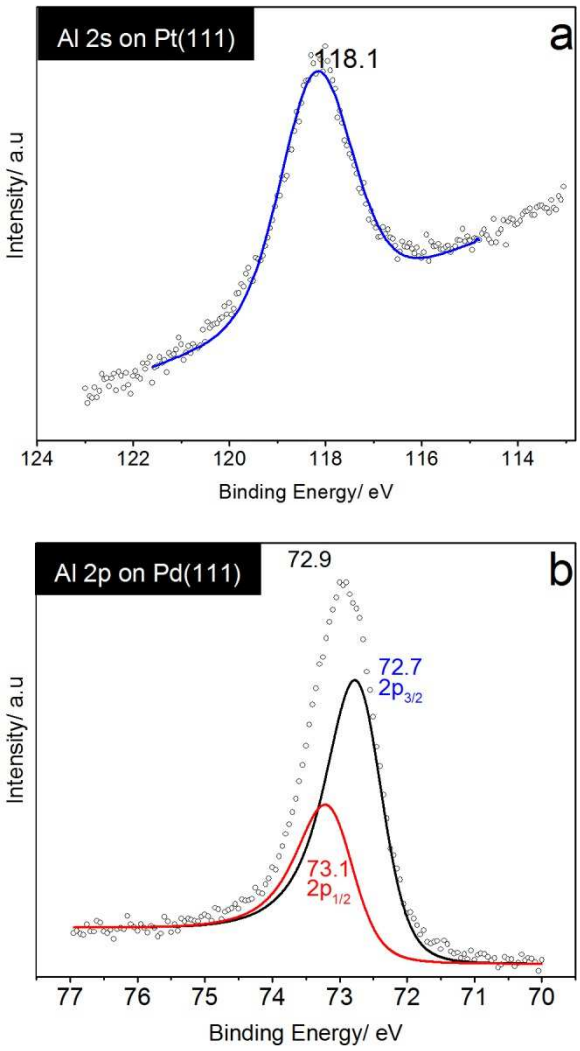


Figure 4.2. XPS spectra of (a) the Al 2s core-level from Pt(111) and (b) Al 2p core level from Pd(111) after exposure to 2000 L TMA at 473 K.

Figure 4.2 shows typical Al 2s and Al 2p spectra obtained from Pt(111) and Pd(111) surfaces after saturation TMA exposure (2000 L) at 473 K. On Pt(111), the Al 2p peak overlaps with Pt 4f and, therefore, the Al 2s peak was used for analysis. The Al 2s peak was fit with one component at 118.1 eV, which was assigned to either metallic Al and/or Al−$(CH_3)_x$.[102] In case of Pd(111), the Al 2p spectra from TMA/Pd(111) was fit with two

spin-orbital components; the Al 2p peak is located at 72.9 eV, which was assigned to either metallic Al and/or Al−$(CH_3)_x$ species. This is in good agreement with the reported Al 2p BE for metallic Al at 73.0 ± 0.1 eV.[103] From these experiments, it is clear that TMA catalytically decomposes on bare palladium and platinum surfaces. This is consistent with DFT calculations and XPS experiments showing that TMA dissociation is favorable on both Pd(111) and Pt(111) surfaces.[19]

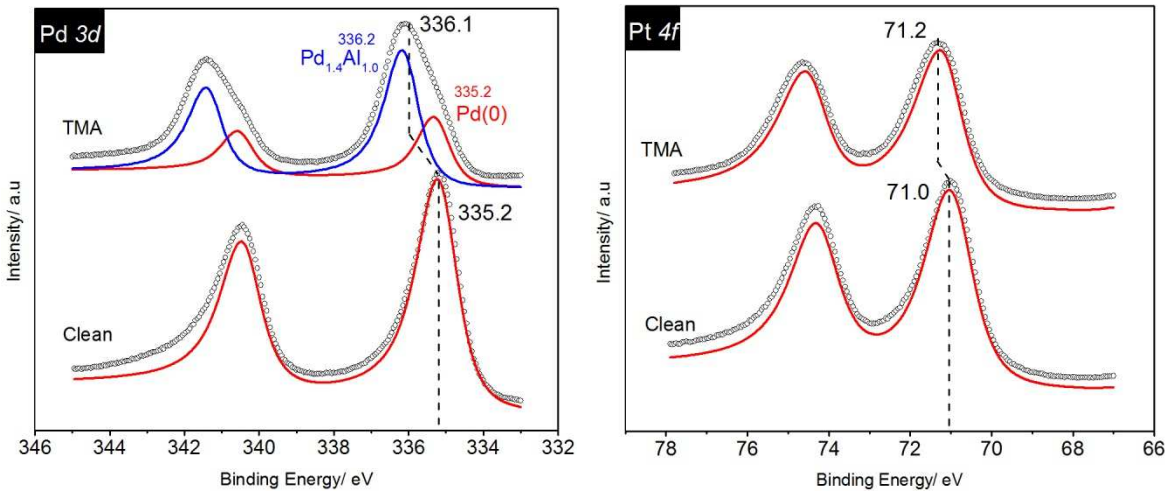


Figure 4.3. XPS spectra of Pd 3d and Pt 4f obtained from the clean Pd(111) and Pt(111) surfaces (left spectra) and after exposure to 2000 L TMA at 473 K (right spectra).

Figure 4.3 shows the Pd 3d and Pt 4f core level regions obtained from clean Pd(111) and Pt(111) surfaces and the same surfaces after exposure to 2000 L TMA at 473 K. For the clean Pd(111) surface, the Pd $3d_{5/2}$ peak was located at 335.2 eV, characteristic of metallic palladium (see for instance reference[69] and references therein). Following TMA exposure, the centroid of the Pd $3d_{5/2}$ peak shifted to 336.2 eV, suggesting alloy formation (Figure 4.3). The curve-fitting analysis yielded two Pd $3d_{5/2}$ components at 335.2 and 336.2 eV. The former was attributed to Pd metal (36% of the total Pd 3d peak

area), and the latter was assigned to the Pd-Al alloy (64% of the total Pd 3d peak area). The assignment of the component at 336.2 eV to the Pd-Al alloy was based on literature data where 0.8-2.1 eV shifts to higher BEs were reported for Pd 3d peaks for Pd-Al alloys.[104-107] Shifts to higher BEs were observed for palladium alloys with Zn, Ga and In as well.[108-110] The magnitude of the BE shift typically correlates the Al to Pd ratio, with higher Al:Pd ratios shifting to higher BEs. Assuming that all Al assigned to Al metal or $Al-(CH_3)_x$ is alloyed with Pd following TMA dosing, XPS data quantification yielded an average Pd-Al alloy composition of $Pd_{1.4}Al_{1.0}$.

TMA adsorption on Pt(111) did not result in a pronounced shift of Pt $4f_{7/2}$: the peak centroid was located at 71.0 and 71.2 eV before and after TMA adsorption, respectively (Figure 4.3). Since, similar to Pd-Al, Pt-Al alloys exhibit a shift to higher BE of Pt $4f_{7/2}$ from 0.9 to 1.2 eV,[111-113] the absence of this shift should point to the lack of Pt-Al alloying. Our experiments performed using surface sensitive synchrotron-based XPS showed a similar 0.1-0.2 eV BE shift after exposing the Pt(111) to TMA, which is consistent with no Pt-Al alloying.

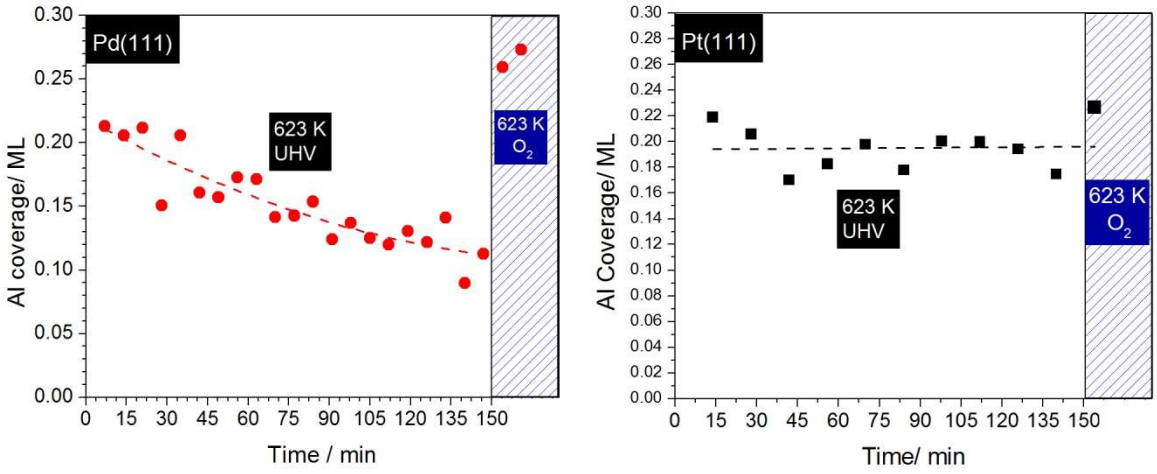


Figure 4.4. The Al coverage on Pd(111) (left panel) and on Pt(111) (right panel) as a function of time at 623 K in UHV. The initial Al adlayer was prepared by exposing Pd(111) and Pt(111) to 3 L and 10 L TMA, respectively, at 473 K. The XPS spectra were obtained at 623 K. Points within the shaded regions were obtained following further exposure to $4\times10^4$ L $O_2$ at 623 K.

To further investigate the alloying of Al, Pd(111) and Pt(111) were heated at 623 K in UHV for 150 min. following exposure to 3 L and 10 L TMA, respectively, at 473 K. As shown in Figure 4.4 Al coverage decreased from approximately 0.2 ML to 0.1 ML upon heating at 623 K for 150 min. on the Pd(111) surface. This was interpreted as aluminum diffusion into the Pd bulk. The Al 2p peak remained at 72.9 eV during annealing in UHV. After exposure of the annealed surface to $4\times10^4$ L oxygen at 623 K (the blue shaded regions in Figure 4.4), Al coverage increased beyond the initial value to approximately 0.25 ML as oxygen pulls Al which had previously diffused into the bulk back to the surface and oxidizes it. The Al 2p peak was observed at 74.1 eV, which is a characteristic

position for $Al_2O_3$.[114] This experiment also ruled out possible evaporation of aluminum upon heating.

In the case of Pt(111), Al coverage did not change during annealing at 623 K in UHV as shown in Figure 4.4, which proved the absence of Al diffusion into the Pt bulk. The Al 2s peak at 118.1 eV did not shift upon heating in UHV. The following $O_2$ exposure did not change the Al coverage as shown in the shaded blue region of Figure 4.4. The Al 2s peak broadened and shifted to 118.5 eV, and a shoulder appeared on the higher binding energy side at 118.9 eV. These data demonstrated that aluminum can readily diffuse into the Pd(111) bulk, forming a Pd-Al alloy. On the other hand, no Al diffusion into the bulk or alloying with Pt was detected on the Pt(111) surface.

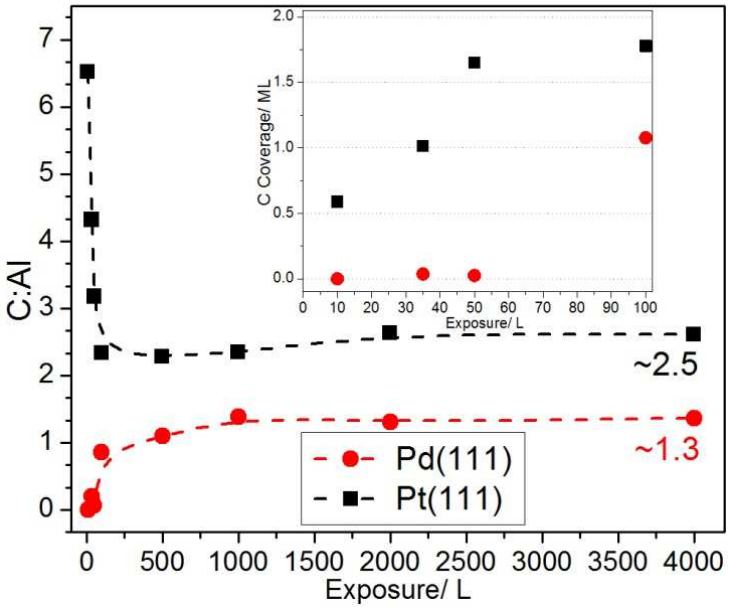


Figure 4.5. Carbon to aluminum ratio as a function of TMA exposure at 473 K. Inset: Carbon coverage on the Pt(111) and Pd(111) surfaces at 473 K as a function of TMA exposure for exposures less than and equal to 100 L.

Figure 4.5 shows the carbon to aluminum ratios for TMA exposures to 4000 L at 473 K. The C:Al ratios were about 2.5 and 1.3 at TMA exposures above saturation (≥ 500 L) on Pt(111) and Pd(111), respectively. As shown in the inset of Figure 4.5, the carbon coverage is negligible on Pd(111) at TMA exposures < 50 L, whereas the carbon coverage increased rapidly on the Pt(111) surface at the same exposures.

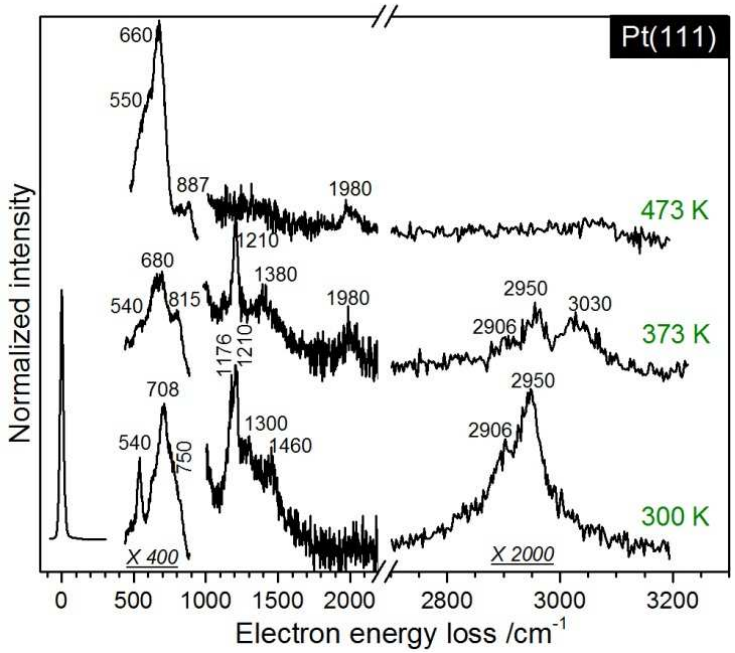


Figure 4.6. HREELS spectra following 6 L TMA exposure at 300 K and consecutive annealing to 373 and 473 K in UHV on Pt(111).

Because the XPS C 1s regions following exposure to TMA on Pd(111) and Pt(111) showed only a single peak at 284.3 eV, detailed information about the nature of the carbon-containing species present could not be determined. Therefore, HREELS, a vibrational technique that is highly sensitive (~$10^{-3}$ ML) to the nature of adsorbed carbon species, was used to follow the initial stage of TMA adsorption on both surfaces. Figure 4.6 shows the HREELS spectra obtained from the Pt(111) surface exposed to 6 L TMA at

300 K and then annealed at 373 and 473 K in UHV. Judging from complexity of the spectra, TMA adsorption resulted in the formation of several species. To identify the peaks, the literature data are summarized in Table 4.1 for TMA and other relevant hydrocarbon species on metal surfaces. Table 4.2 shows the positions of the main HREELS peaks after TMA adsorption on Pt(111) and heating in UHV.

Table 4.1 The main vibration modes and frequencies for relevant hydrocarbon species on metal surfaces. [a] t: terminal.

| Vibration mode | Methylaluminum $Al-CH_3$ | Metal-$C_1$ species | | | Ethylidyne $M\equiv CCH_3$ |
|---|---|---|---|---|---|
| | | $M-CH_3$ | $M=CH_2$ | $M\equiv CH$ | |
| $\nu_{as}(CH_3)$ | 2940-2950[115-119] | | – | – | 2890-2928[120-123] |
| $\nu_s(CH_3)$ | 2900-2907[115-117] | 2955-3044[124-126] | – | – | 2890-2928[120-123] |
| $\nu_{as}(CH_2)$ | – | – | 2900-2925[119, 127, 128] | – | – |
| $\nu_s(CH_2)$ | | | 2850[128] | | |
| $\nu(CH)$ | – | – | | 2950-2975[129, 130] | – |
| $\delta_{as}(CH_3)$ | 1430-1450[119, 131, 132] | 1420-1435[124, 126] | – | – | 1400-1420[120, 123] |
| $\delta_s(CH_3)$ | 1196-1217[26, 115, 116, 118, 132] | 1180-1285[124-126] | – | – | 1329-1350[120-123, 133] |
| $\delta(CH_2)$ | – | – | 1340[119, 127] | – | – |
| $\nu(C-C)$ | – | – | – | – | 900-1180[121-123, 130] |

| | | | | | |
|---|---|---|---|---|---|
| $\rho(CH_3)$ | 650-742[115, 119] | 882-1040[124-126] | – | – | 923[134] |
| $\rho(CH_2)$ | – | – | 860-865[119, 127] | – | – |
| $\delta(CH)$ | – | – | – | 770-805[129, 130, 134] | – |
| $\delta(Al-C^t)^a$ | 567[115] | – | – | – | – |
| $\nu(M-C)$ | | 495-520[126] | | | 371[121] |

Table 4.2 The major HREELS peaks observed from the Pt(111) surface following 6 L TMA exposure at 300 K and consecutive annealing to 373 and 473 K in UHV. Abbreviations: w, weak; s, strong; sh, shoulder; br, broad. NA: not assigned.

| **Pt(111)** | | |
|---|---|---|
| **300 K** | | |
| Energy loss/ $cm^{-1}$ | Vibrational mode | Assignment |
| $2950^s$ | $\nu_{as}(CH_3)$ | MA/ $M-CH_3$ |
| $2906^{sh}$ | $\nu_s(CH_3)$ | MA |
| $1460^{br}$ | $\delta_{as}(CH_3)$ | MA |
| $1210^s$ | $\delta_s(CH_3)$ | $M-CH_3$ |
| $1176^s$ | $\delta_s(CH_3)$ | MA |
| $750^{sh}$ | $\rho(CH_3)$ | MA |
| $540^s$ | $\delta(Al-C)$ | MA |
| **373 K** | | |
| $3030^s$ | $\nu(CH_2)$ | $M-CH_2$ |
| $2950^s$ | $\nu_{as}(CH_3)$ | MA/ $M-CH_3$ |

| | | |
|---|---|---|
| $2906^{sh}$ | $\nu_s(CH_3/CH_2)$ | MA/M−$CH_2$ |
| $1980^{w}$ | ν(C−O) | $CO_{ads}$ |
| $1460^{br}$ | $\delta_{as}(CH_3)$ | MA |
| $1380^{w}$ | $\delta(CH_2)$ | M−$CH_2$ |
| $1210^{s}$ | $\delta_s(CH_3)$ | M−$CH_3$ |
| $1176^{s}$ | $\delta_s(CH_3)$ | MA |
| $815^{sh}$ | $\rho(CH_3)$ | M−$CH_3$ |
| $808^{sh}$ | δ(CH) | M−CH |
| $750^{sh}$ | $\rho(CH_3)$ | MA |
| **473 K** | | |
| $1980^{w}$ | ν(C−O) | $CO_{ads}$ |
| $660^{s}$ | | NA |
| $550^{sh}$ | | NA |

Following TMA adsorption on Pt(111) at 300 K, several characteristic vibration bands of the Al−$(CH_3)_x$ species were detected: the peak at 2950 $cm^{-1}$ is an asymmetric stretching of $CH_3$, $\nu_{as}(CH_3)$; the peak at 2906 $cm^{-1}$ is an symmetric stretching of $CH_3$, $\nu_s(CH_3)$; 1460 $cm^{-1}$ is an asymmetric deformation of $CH_3$, $\delta_{as}(CH_3)$; 1176 $cm^{-1}$ is a symmetric deformation of $CH_3$, $\delta_s(CH_3)$; 750 $cm^{-1}$ is a rocking vibration of $CH_3$, $\rho(CH_3)$; and 540 $cm^{-1}$ is deformation of Al−C, δ(Al−C). These spectroscopic signatures and the relative peak intensities unambiguously point to the presence of the Al−$(CH_3)_x$ species. The resolution of HREELS was not enough to discriminate between Al−$(CH_3)$, Al−$(CH_3)_2$, and Al−$(CH_3)_3$. However, according to DFT calculations, TMA readily dissociates on the Pt(111) surface at 300 K, and the Al−$(CH_3)$ species is predicted to be the most

thermodynamically favorable decomposition product compared to Al−$(CH_3)_2$ and intact TMA. Therefore, the above loss bands were assigned to Al−$(CH_3)$ (methylaluminum (MA)) species. The peak at 1210 $cm^{-1}$ was assigned to symmetric deformation of $CH_3$ adsorbed on Pt(111), $\delta_s(CH_3)$. The stretching vibrations of the $CH_3$ species on Pt(111) were expected around 2950 $cm^{-1}$ but were likely overlapping with the MA stretching bands. The deformation vibration, δ(CH), and rocking vibration, $\rho(CH_2)$, of $CH_{ads}$ and $CH_{2,ads}$ species should be around 700-860 $cm^{-1}$. The HREELS region below 1000 $cm^{-1}$ is crowded with peaks, so making straightforward assignments is difficult. Therefore, the presence of the $CH_{2,\,ads}$ and $CH_{ads}$ species cannot be ruled out. The conclusion is that after TMA adsorption on Pt(111) at 300 K, the surface is covered by MA, $CH_{3,\,ads}$ and $CH_{x,\,ads}$. The heating of this adlayer at 373 K resulted in strong changes in the HREELS spectra. All vibrations associated with the Al−$(CH_3)$ species decreased in intensity significantly. On the other hand, the deformation band at 1210 $cm^{-1}$ of the $CH_{3ads}$/Pt(111) species did not change. A new energy loss band was observed at 1380 $cm^{-1}$ and was assigned to the in-plane bending mode of a surface methylene group, $CH_{2,ads}$. The peak at 3030 $cm^{-1}$, the stretch mode of $CH_{2,ads}$, increased in intensity after heating at 373 K. The methylene group ($CH_2$) has been observed during the thermal decomposition of TMA and trimethylindium (TMIn) on the GaAs(100) surface.[119, 127] In our case, the methylene group might form during decomposition of the Al−$(CH_3)$ species through the migration of methyl groups to Pt(111) followed by dehydrogenation. Further dehydrogenation of $CH_{2,\,ads}$ to $CH_{ads}$ species could not be confirmed: the region around 700 $cm^{-1}$ is filled with unresolved features which hindered following the δ(CH) peak. Additionally, the

stretching frequency of $CH_{ads}$ may overlap with stretching bands of $CH_{3,ads}$ around 2950 $cm^{-1}$.

Further heating at 473 K led to complete dehydrogenation of the hydrocarbon groups: no C−H stretching was detected. XPS data showed the presence of carbon after annealing to 623 K. Based on the literature data,[130, 135] carbon remaining after $CH_{3,\ ads}$, $CH_{2,\ ads}$ and $CH_{ads}$ dehydrogenation could be carbon atoms and/or clusters. A broad feature at ~660 $cm^{-1}$ with a shoulder at 550 $cm^{-1}$ and a peak at 887 $cm^{-1}$ were still detected in the low frequency region after heating at 473 K. These peaks are probably due to some vibration involving aluminum and carbon atoms left on the surface but a straightforward assignment was not possible. A weak peak centered at ~1980 $cm^{-1}$ was assigned to $CO_{ads}$ originating from background CO that only appeared after annealing at 373 K.

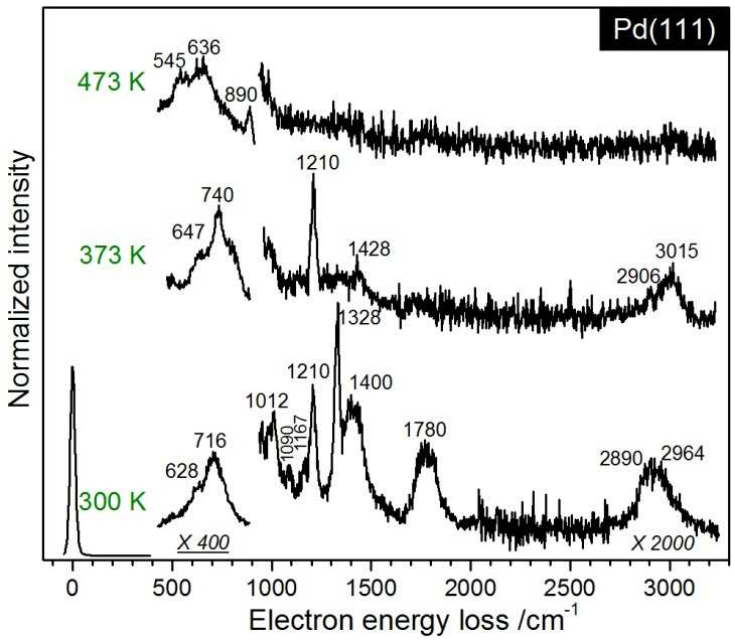


Figure 4.7. HREELS spectra obtained from the Pd(111) surfaces following 6 L TMA exposure at 300 K and consecutive annealing to 373 and 473 K in UHV.

Figure 4.7 displays the HREELS spectra obtained after exposure of the Pd(111) surface to 6 L TMA at 300 K and following annealing at 373 and 473 K in UHV. Table 4.3 shows the positions of the main HREELS peaks after TMA adsorption on Pd(111) and heating in UHV. The characteristic peaks at 1012 ($\nu$(C-C)), 1090 ($\rho(CH_3)$), 1328 ($\delta_s(CH_3)$), 1400 ($\delta_{as}(CH_3)$), 2890 ($\nu_s(CH_3)$), and 2964 ($\nu_{as}(CH_3)$) $cm^{-1}$ are due to the ethylidyne species ($\equiv CCH_3$). The peak at 1210 $cm^{-1}$, also observed on Pt(111), was assigned to symmetric deformation of $CH_3$ adsorbed on Pd(111), $\delta_s(CH_3)$. The high frequency region shows a broad, unresolved feature centered at ~2940 $cm^{-1}$. Therefore the stretching vibrations of the $CH_3$ species could not be separated from the vibrations of the other C−H containing species. The presence of a $CH_{2,ads}$ species was supported by a weak unresolved shoulder at 3035 $cm^{-1}$. The HREELS region below 1000 $cm^{-1}$ is crowded, and the presence of $\delta$(CH) at about 700 $cm^{-1}$ could not be confirmed. The presence of the MA species cannot be ruled out. Thus, the peak at 1167 $cm^{-1}$, which is a symmetric deformation $\delta_{as}(CH_3)$ of MA, was detected. Unfortunately, other ethylidyne signatures overlapped with other peaks. Judging from the peak intensities, the amount of the MA species on Pd(111) is much lower than on Pt(111) where MA was one of the dominant species.

Table 4.3. The major HREELS peaks observed from on Pd(111) following 6 L TMA exposure at 300 K and consecutive annealing to 373 and 473 K in UHV. Abbreviations: vw, very weak; w, weak; s, strong; sh, shoulder; br, broad; NA, not assigned.

| **Pd(111)** | | |
|---|---|---|
| **300 K** | | |
| Energy loss/ $cm^{-1}$ | Vibrational mode | Assignment |
| $2964^{br}$ | $\nu_s(CH_3)$ | $M-CH_3$/ $M\equiv CCH_3$ |
| $2890^{sh}$ | $\nu_{as}(CH_3)$ | $M\equiv CCH_3$ |
| $1780^{br}$ | $\nu(C-O)$ | $CO_{ads}$ |
| $1400^{br}$ | $\delta_{as}(CH_3)$ | $M\equiv CCH_3$ |
| $1328^{s}$ | $\delta_s(CH_3)$ | $M\equiv CCH_3$ |
| $1210^{s}$ | $\delta_s(CH_3)$ | $M-CH_3$ |
| $1167^{vw}$ | $\delta_s(CH_3)$ | MA |
| $1090^{w}$ | $\rho(CH_3)$ | $M\equiv CCH_3$ |
| $1012^{br}$ | $\nu(C-C)$ | $M\equiv CCH_3$ |
| **373 K** | | |
| $3015^{br}$ | $\nu_{as}(CH_3)$ | $M-CH_3$ |
| $2906^{w}$ | $\nu_{as}(CH_2)$ | $M-CH_2$/$M-CH$ |
| $1428^{vw}$ | $\delta_{as}(CH_3)$ | $M-CH_3$ |
| $1210^{s}$ | $\delta_s(CH_3)$ | $M-CH_3$ |
| **473 K** | | |
| $890^{s}$ | | NA |
| $636^{br}$ | | NA |
| $545^{sh}$ | | NA |

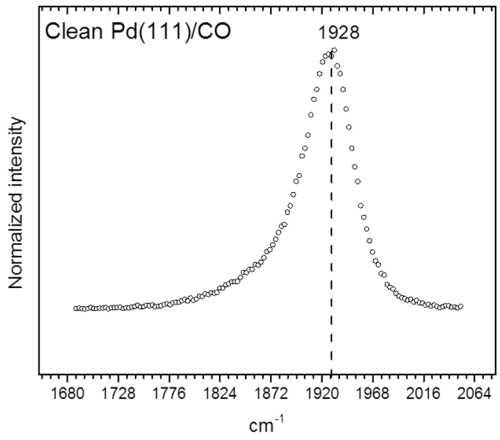


Figure 4.8.HREELS spectra for room temperature CO adsorption on clean Pd(111)

A broad peak centered at ~1780 $cm^{-1}$ was assigned to $CO_{ads}$ originating from chamber background gases (Figure 4.8). This is interesting for two reasons: first, the presence of $CO_{ads}$ indicates that the surface after adsorption/decomposition of 6 L TMA still had adsorption sites for CO. This was not the case for Pt(111) where adsorbed hydrocarbon species blocked CO adsorption. Second, the C−O stretching frequency shifted toward lower energy compared to CO adsorption on a clean Pd(111) surface, where the C−O stretching band was at 1928 $cm^{-1}$ for saturated CO coverage at 300 K (). The hydrocarbon species and/or aluminum may affect the C−O bond. However, investigation of CO is out of scope of this paper.

Ethylidyne is only stable up to about 300 K on the Pd(111) surface.[120, 121, 136] Heating at 373 K resulted in the disappearance of the ethylidyne group: all characteristic peaks were gone. No HREELS peaks of the MA species were detected whereas the symmetric deformation of $CH_3$ adsorbed on Pd(111) at 1210 $cm^{-1}$ did not change in intensity. The

high-frequency region underwent these changes accordingly: peaks at 2890 and 2964 $cm^{-1}$, assigned to $\nu_s(CH_3)$ and $\nu_{as}(CH_3)$ of ethylidyne, were not observed. The weak peak at 2906 $cm^{-1}$ might be a feature of $\upsilon_{as}(CH_2)$ for $CH_{2ads}$ or $CH_{ads}$ species; however, it was not possible to resolve $\delta$(CH) around 700 $cm^{-1}$.

No C−H stretching vibration or any other loss peaks were observed above 1000 $cm^{-1}$ after heating the surface at 473 K. Based on the XPS data, no carbon was present at this temperature (see Fig. SI.3). The HREELS region below 1000 $cm^{-1}$ was similar to the spectrum from TMA/Pt(111) at 473 K: a broad peak at 636 $cm^{-1}$ with weak shoulders at 545 $cm^{-1}$, and a well-resolved peak at 890 $cm^{-1}$. A straightforward assignment for these losses was not possible.

The HREELS data showed that TMA adsorption on Pt(111) and Pd(111) resulted in different compositions of the adsorbed layer. Methylaluminum (MA) was one of the dominant species on Pt(111). Adsorbed $CH_{x,ads}$ species (x=1, 2, 3) were detected on both Pt(111) and Pd(111). Ethylidyne was only observed on the Pd(111) surface.

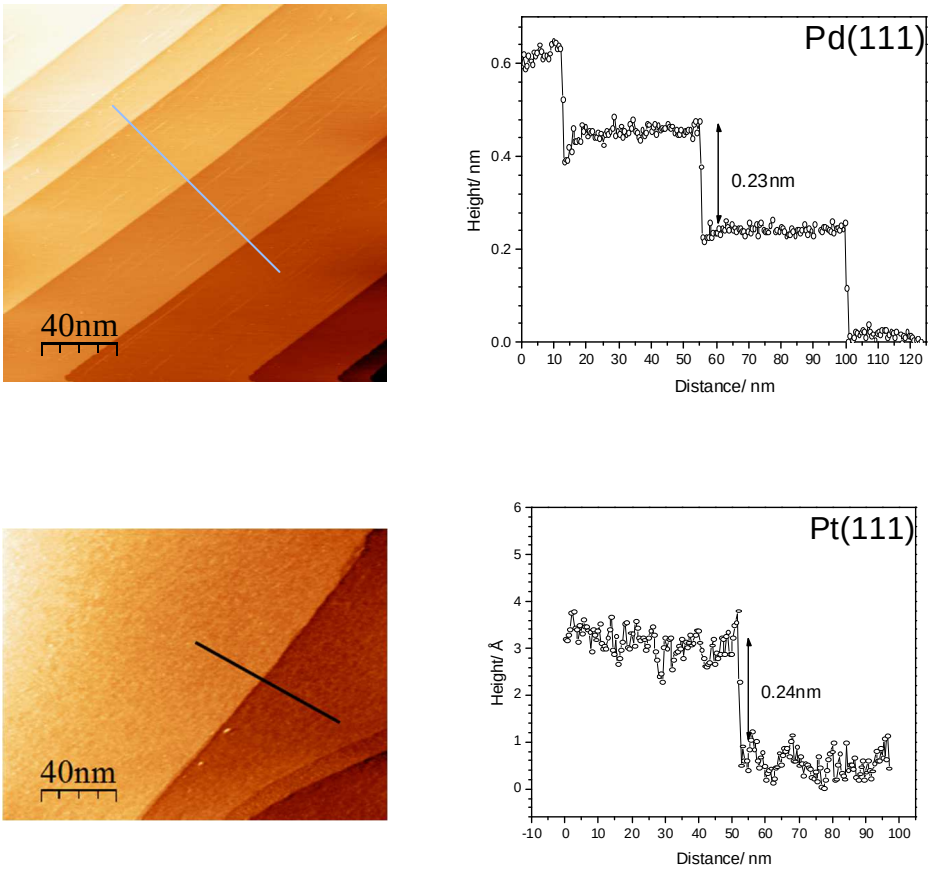


Figure 4.9. STM images of clean Pd(111) ($I_t$ = 0.5 nA $U_t$=0.5 V )and Pt(111) ($I_t$ = 0.3 nA $U_t$ = 0.5 V) which are characterized by wide, flat terraces separated by monatomic step edges, where the yellow terrace is topographically the highest area. The height profiles along the solid lines pointed in each image are shown in the right panel.

The interaction of TMA with Pd(111) and Pt(111) surfaces at room temperature and after annealing to 423, 523 and 623 K was followed using STM. Prior to TMA exposure Pt(111) and Pd(111) surfaces were characterized by atomically flat terraces separated by steps of atomic height: 2.4 and 2.3 Å, respectively (Figure 4.9).

Exposures of TMA > 20 L resulted in a roughened surface, which impaired STM imaging. Therefore, low exposures (2.5 L) yielding sub-monolayer Al coverages were used for the STM experiments. Figure 4.10a shows an STM micrograph (200 nm × 200 nm) of Pd(111) after 2.5 L exposure to TMA at room temperature. The terraces and monoatomic steps can be seen. Two distinct features of the TMA/Pd(111) surface are observed: (i) steps are covered with features that look like Norwegian fjords, and (ii) fractal islands jut out from steps which cover the terraces. The average height of the fractal islands was about 2.0 ± 0.3 Å, measured from the bimodal peak distribution in the histogram of pixel heights on the flat terraces as shown in Figure 4.10b.

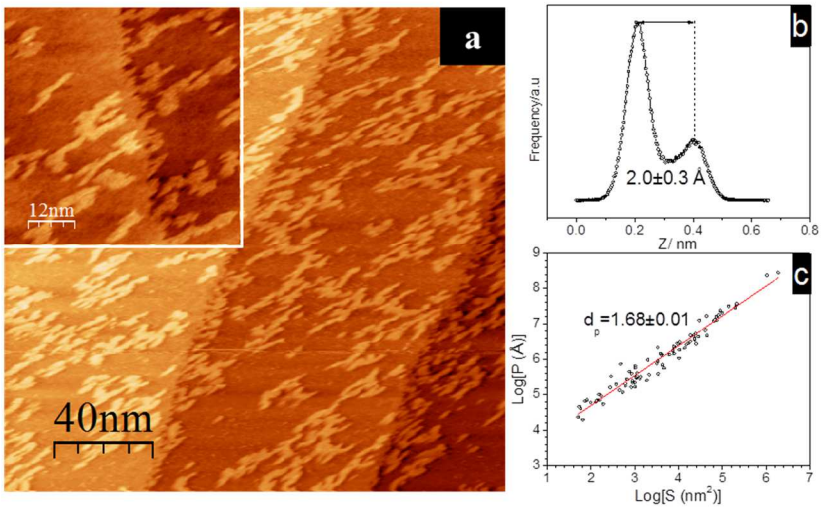


Figure 4.10.(a) STM images of Pd-Al islands formed after deposition of 2.5 L TMA at room temperature on Pd(111). Imaging conditions: 200 nm × 200 nm, $I_t$=0.5 nA, $U_t$=0.5 V. (b) Height histogram of pixels in STM images on flat terraces. (c) Plot of the perimeter (P) vs area (S) relationship of Pd-Al islands.

The bimodal distribution confirms the uniform height and flatness of the islands. The fractal islands have similar height (2.0 ± 0.3 Å) as the monoatomic Pd(111) steps. Therefore, the fractal islands and terraces likely have the same composition. According to the XPS and HREELS data, TMA dissociates to aluminum and hydrocarbon products on Pd(111). The characteristic high BE shift of Pd 3d peaks were evidence of the presence of a Pd-Al alloy. Since no evidence of aluminum atoms or clusters were detected, we conclude that the fractal islands consist of the Pd-Al alloy. The fjord-like features grew from steps and covered all step edges. This might point to the role played by steps in TMA adsorption/dissociation. Indeed, DFT calculations (discussed below) showed that MA dissociation on the step is more thermodynamically favorable than on the flat terraces. The fjord structures were observed growing out from the lower plane next to a step edge. This indicates the existence of an energy barrier for adatoms climbing over a step to a higher terrace, and highlights the role of the step edges in formation of the Pd-Al alloy islands. The fjord-like features attached to the step at random angles.

As reported by Batabyal et al.,[137] the shape of the 2-D fractal islands can be quantified in terms of fractal dimension, $d_p$, obtained from the perimeter- (P) area (S) relationship as $\ln P \, \alpha \, (d_p/2) \ln S$. The fractal dimension was $d_p$ = 1.68±0.01 after adsorption of 6 L TMA on Pd(111) at the room temperature (Figure 4.10c). $d_p$ in the range of 1.7 corresponds to a two-dimensional diffusion-limited-aggregation (DLA) growth mechanism,[138, 139] in which atoms diffuse randomly on a 2D lattice and attach irreversibly to perimeters of the growing aggregates forming irregular, branched fractal islands. The extended DLA mechanism allows atoms to relax locally after hitting an island by finding an energetically favorable site and branches can consist of more than one atom. An atom

attaching to a triangular lattice can stabilize only with two nearby neighboring pairs. The long-range diffusion along the island boundary is inhibited, and this results in the formation of highly fractal structures. The extended DLA mechanism can reasonably explain the highly fractal islands and growths on the steps (Figure 4.10). Thus, the MA species dissociates on the step to Al, and the aluminum atoms either accumulate in the step starting the growth of the fjord-like features, or diffuse across the surface until sticking to the boundary of the growing fractal island. The other possibility is that an aluminum atom can displace a palladium atom. The displacement of a palladium atom from a step is more likely than from a terrace. Since the fractal islands, the steps, and the fractal structures near the steps likely have similar chemical structures, palladium atoms likely participate in building the fractal structures.

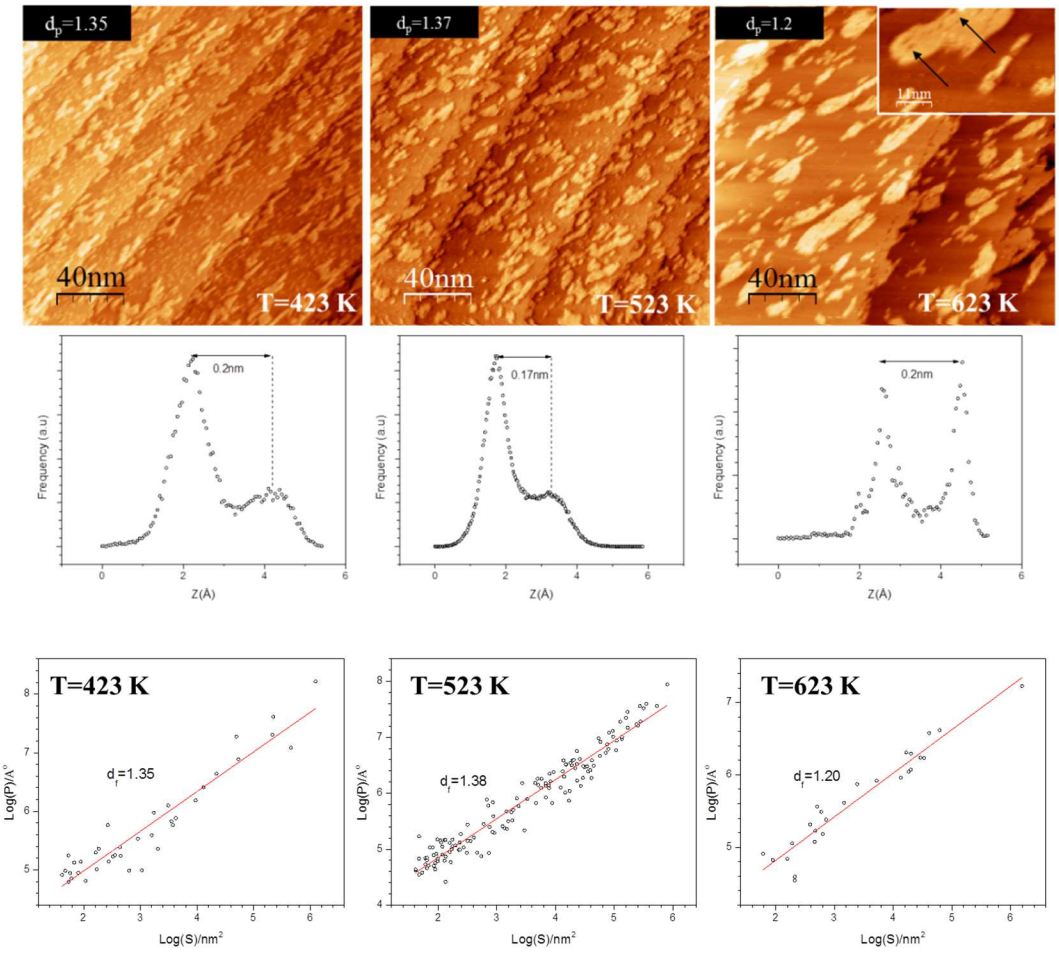


Figure 4.11. Room temperature STM images of Pd-Al islands after annealing the Pd(111) surface to 423, 523 and 623 K for 15 min. Imaging conditions: 200 nm × 200 nm, $I_t$=0.5 nA, $U_t$=0.5 V. More compact Pd-Al islands are formed on Pd(111) with increasing temperature, corresponding to a decrease in $d_p$ value. . Height histogram of pixels in STM images on flat terraces are shown below each image. Plot of the perimeter (P) vs area (S) relationship of PdAl islands at each temperature is used for calculating the $d_p$ value.

STM images after annealing the surface to 423, 523 and 623 K are shown in Figure 4.11. The perimeter fractal dimension ($d_p$) and the height distribution histogram are obtained in

the same manner as in Figure 4.10 at each temperature. Heating the surface at 423 K decreased the fractal dimension ($d_p$) to 1.35 ± 0.03. Increasing the temperature to 523 K did not alter the $d_p$ value (~1.38 ± 0.02). After annealing at 623 K, $d_p$ decreased to 1.2 ± 0.04. The decreasing of $d_p$ with increasing temperature represented the transition from fractal to compact island shape. Thus, $d_p$ is equal to 1 for an ideal 2-D compact object. Increasing the temperature facilitated the movement of the low coordinated atoms, which led to changing the islands from a fractal shape at room temperatures to a more compact shape at 623 K. A similar transition from fractal to compact island shape by annealing the sample has been reported for the Ag/Pt(111) system.[140]

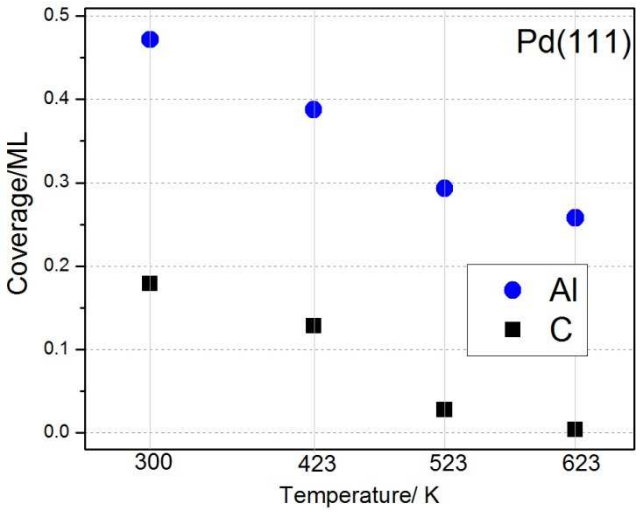


Figure 4.12. Al and C coverages after exposing the Pd(111) surface to 2.5 L TMA at room temperature and annealing up to 623 K.

Height histograms for the islands at 300, 423 and 623 K indicate that island height remains constant (~2 Å) after annealing the sample. From Figure 4.11, one can see that annealing to 623 K results in the appearance of pit-holes on the surface of Pd-Al islands (highlighted by black arrows). These pit-holes might be caused by the diffusion of Al

atoms into the palladium bulk. Indeed, according to the XPS data, the aluminum coverage decreased upon annealing. The Al coverage is presented in Figure 4.12.

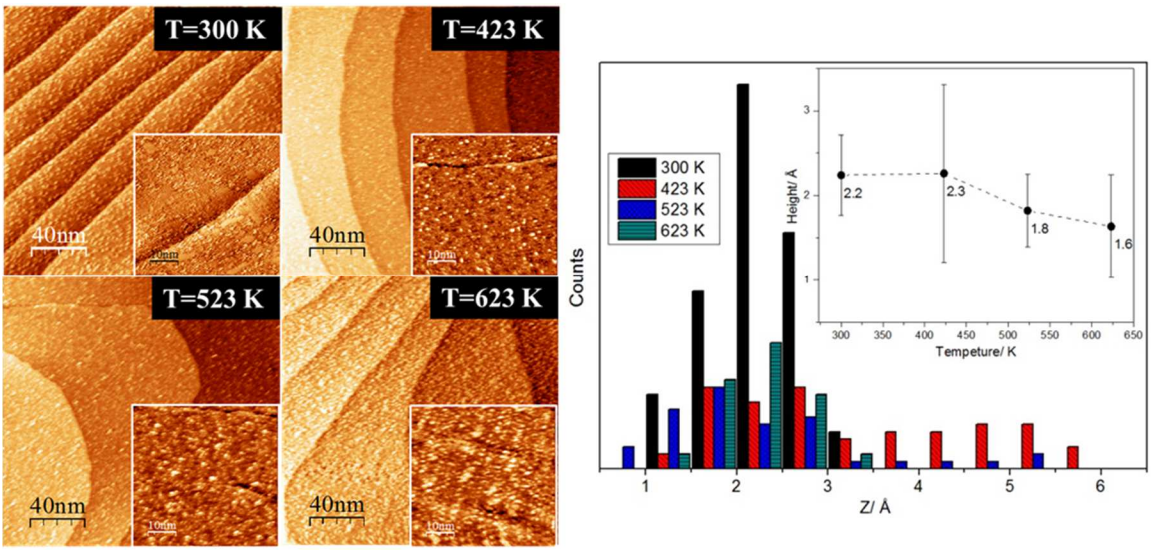


Figure 4.13. Left panel: STM images after exposing the Pt(111) surface to 2.5 L of TMA at 300 K (200 nm × 200 nm, $I_t$=0.3 nA $U_t$=0.5 V; Inset: 50 nm × 50 nm, $I_t$=0.7 nA, $U_t$=0.5 V) and annealing the sample to 423 K (200 nm × 200 nm, $I_t$=0.5 nA $U_t$=0.8 V; Inset: 50 nm × 50 nm, $I_t$=0.5 nA, $U_t$=0.8 V), 523 K (200 nm × 200 nm, $I_t$=0.3 nA $U_t$=0.5 V; Inset: 50 nm × 50 nm, $I_t$=0.7 nA, $U_t$=0.5 V) and 623 K (200 nm × 200 nm, $I_t$=0.5 nA $U_t$=0.5 V; Inset: 50 nm × 50 nm, $I_t$=0.5 nA, $U_t$=0.5 V) for 15 min. Right panel: distributions of particle heights observed at 300 K and after annealing to the indicated temperatures. Inset: the average particle height versus temperature.

Figure 4.13 shows STM images of Pt(111) after TMA exposure and consecutive annealing to 423, 523 and 623 K. Unlike Pd(111), no island-like or peninsula-like features were detected on the Pt(111) surface exposed to 2.5 L TMA at room temperature. Bright, elongated spots with apparent height of 2.2 ± 0.4 Å were homogenously

distributed on the surface. These bright features are assigned to Al−$CH_3$ species. The methyl group and the carbon clusters, which are present on the surface at these conditions according to the HREELS and XPS data, might hinder the surface diffusion of the Al−$CH_3$ species towards the steps, where Al−$CH_3$ might dissociate. The diffusion limitation may explain why the fractal islands observed on Pd(111) surface did not form on Pt(111). After annealing at 423 K, the height showed a bimodal distribution with the first maximum at ~2.3 Å, which is close to the Al−($CH_3$) species, and the second broad maximum was at 5 Å height (Figure 4.13). According to the XPS and HREELS data, at these conditions, the surface was covered with the remaining Al−$CH_3$ species, $CH_{x,ads}$, and aluminum. The bimodal height distribution might be associated with these different species on the surface at 423 K. The appearance of the new species correlated with the ongoing dehydrogenation process and formation of aluminum and/or carbon clusters on the surface. After annealing to 523 K, the height distribution narrowed, and one peak was detected at 1.8 ± 0.4 Å. At this temperature only aluminum and carbon were observed by XPS. Therefore, the single peak height distribution might correspond to the segregation of aluminum and/or carbon clusters. This segregation continued after heating at 623 K: the surface became more uniform and flattened out. The height of the small features was 1.6 ± 0.6 Å.

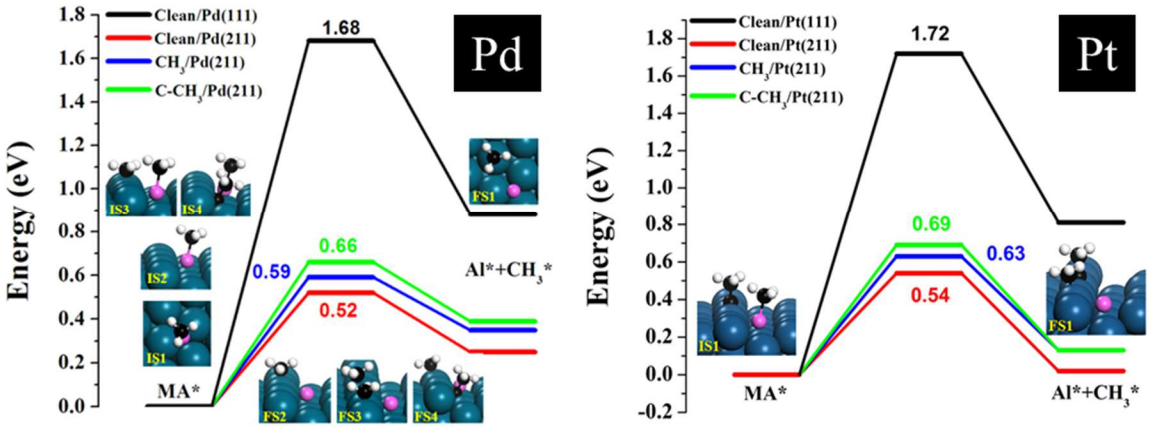


Figure 4.14. The potential energy surfaces of MA dissociation on clean and $CH_3$/$CCH_3$ covered (111) and (211) surfaces for Pd and Pt. The insets are the initial and final states. The blue, pink, black, and white spheres present Pd, Al, C, and H atoms, respectively.* Work of Dr. Xiangkui Gu.

To better understand the mechanism of TMA interaction with Pd(111) and Pt(111) substrates, DFT calculations were performed. Previous calculations showed that TMA decomposition to MA is kinetically and thermodynamically favorable on both Pd(111) and Pt(111) surfaces and, therefore, MA was expected to be the dominant species.[19] The potential energy surfaces of MA dissociation on clean Pt(111) and Pd(111) terraces, and $CH_3$/$CCH_3$ covered and clean Pd(211) and Pt(211) surfaces are shown in Figure 4.14. The calculated barriers for hollow-site MA (Figure 4.14.IS1) dissociation to Al and $CH_3$ (Figure 4.14.FS1) are 1.68 and 1.72 eV on clean Pd(111) and Pt(111), respectively. This means that MA dissociation on Pt(111) and Pd(111) terraces is thermodynamically unfavorable.

Also, the ability of defect sites such as step edges to dissociate MA was investigated. On clean Pd(211), the calculated barrier is only 0.52 eV for the dissociation of the four-fold-

site MA to four-fold-site Al and top-site $CH_3$ at a step, which is lower by 1.16 eV than the corresponding value on Pd(111) terraces (Figure 4.14.IS2). This is because the interaction between the abstracted $CH_3$ and Pd in the transition state (TS) on Pd(211) is stronger than on Pd(111). This is supported by the shorter bond distance of 2.10 Å for C−Pd on Pd(211) compared to 2.16 Å on Pd(111) in its TS. The conclusion is that steps can facilitate MA dissociation. On the other hand, carbon species adsorbed on a step have a small influence on MA dissociation (Figure 4.14). This is because the steric repulsion between existing carbon species and the abstracted $CH_3$ is relatively small on the unoccupied stepped surface. When the step was covered by 1/3 ML $CH_3$ or $CCH_3$, the calculated barriers were 0.59 and 0.66 eV, respectively, which are no more than 0.14 eV higher compared to the same values on the clean surface.

Figure 4.14 also shows results for MA dissociation on clean Pt(211) and on the same surface covered with 1/3 ML $CH_3$ or $CCH_3$. Although ethylidyne was detected experimentally only on Pd, its impact on MA dissociation on Pt(211) was investigated for comparison. The calculated barrier is 0.54 eV on clean Pt(211), and the barriers are 0.63 and 0.69 eV on Pt(211) covered with $CH_3$ and $CCH_3$, respectively. 2/3 ML $CH_3$ on the stepped top-site blocks MA dissociation.

The above calculations indicate that the MA dissociation is thermodynamically hindered on Pt(111) and Pd(111) terraces. On the other hand, MA dissociation is favorable on platinum and palladium steps up to carbon species coverage of approximately 1/3 ML.

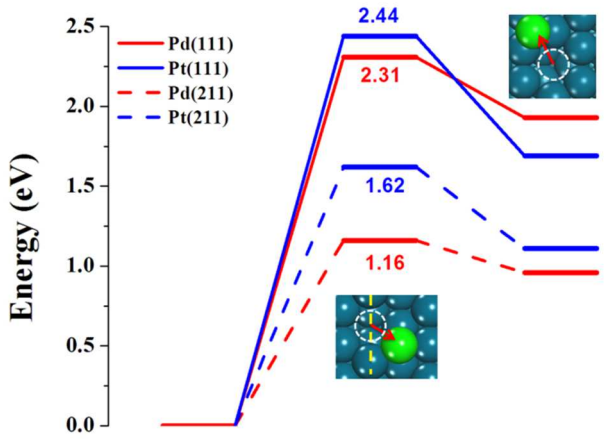


Figure 4.15.The potential energy surfaces of Pd/Pt vacancy formation. The dashed yellow line is the position of step and the white circle is the vacancy formed. The blue and green spheres represent Pd/Pt atoms and Pd/Pt adatoms, respectively.* Work of Dr. Xiangkui Gu.

Alloying was modeled as a two-step process: First, the surface Pd vacancy is formed, followed by the Al atom filling the vacancy. Figure 4.15 shows that removing an atom from the (111) terrace to form an adatom and a vacancy has barriers of 2.31 and 2.44 eV for Pd and Pt, respectively. However, this process is relatively easy on stepped surfaces. On Pd(211), the calculated barrier is 1.16 eV, 1.17 eV lower than on Pd(111). This is due to the lower coordination number of a Pd atom on the stepped surface compared to the (111) terraces. Moreover, the four-fold site Al adatom resulting from MA dissociation can diffuse to the step Pd vacancy with an energy barrier of only 0.02 eV. Therefore, Pd-Al alloying can occur at the step. Similarly, the calculated barrier of 1.62 eV for Pt vacancy formation on Pt(211) is lower by 0.82 eV than on Pt(111). However, it is higher by 0.46 eV than on Pd(211). Therefore, vacancy formation on steps is easier on Pd than

on Pt. On both surfaces, DFT calculations demonstrate the importance of the step for (i) MA dissociation and (ii) alloy formation.

## 4.5 Discussion

The results of our investigation of TMA interaction with Pd(111) and Pt(111) surfaces highlight the effect of substrate, which affects growth and morphology of ultra-thin films. For an ideal ALD process, an organometallic precursor anchors to the surface through a ligand exchange reaction with surface functional groups during the first half-cycle. The reaction is self-limiting: the amount of an organometallic precursor adsorbed on the surface is controlled by the amount of functional groups. No functional groups are needed for TMA to react with Pt(111) and Pd(111), which are catalytically active substrates. On these surfaces, TMA directly decomposes to aluminum and carbonaceous species at 473 K. The reaction is limited through the blocking of adsorption sites by products of TMA dissociation. The composition of the adlayers formed on Pt(111) and Pd(111) depend on the substrate-TMA interaction. Also, aluminum atoms formed upon TMA decomposition play an important role in the final film structure. A Pd-Al alloy was found on Pd(111); no Pt-Al alloying was detected on Pt(111).

### 4.5.1 TMA on Pd(111)

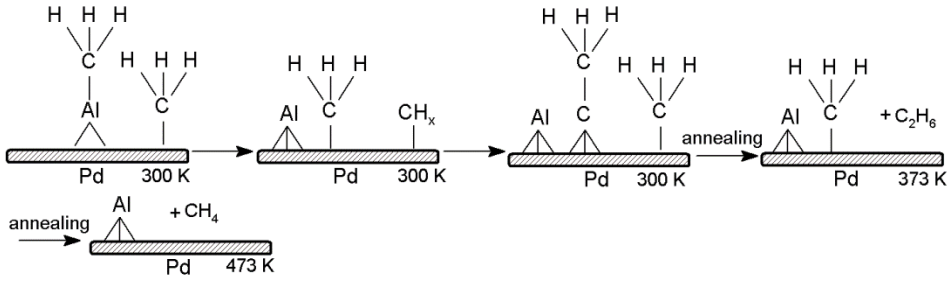


Figure 4.16. Al($CH_3$) reaction mechanism on Pd.

TMA molecules decompose to Al and methyl groups upon adsorption at 300 K on the Pd(111) surface. The $CH_{3,\,ads}$ can react further forming ethylidyne, $CCH_{3,\,ads}$ and different $CH_{x,\,ads}$ species (Figure 4.16). DFT calculations demonstrated that on Pd(111) terraces, TMA decomposes to MA without further dissociation of MA to Al. On the other hand, dissociation of MA has a relatively low barrier on the step sites (Figure 4.14). It should be stressed that at early adsorption stages, the coverage of carbonaceous species is low: at an aluminum coverage of ~0.5 ML, the carbon-containing species coverage was ~0.2 ML at 300 K and 2.5 L TMA exposure (Figure 4.12). Furthermore, ethylidyne, a major hydrocarbon detected on Pd(111) (see Figure 4.7), is very mobile at room temperature.[141] Therefore, MA diffusion across the surface and the following dissociation at step sites is not hindered on Pd. Combining our experimental observations and DFT calculations, we conclude that the decomposition of TMA to MA mainly happens on (111) terraces, whereas the further dissociation of MA to Al occurs preferentially on the step sites. MA moves freely across the (111) terraces reaching dissociation sites on steps. Newly formed Al atoms incorporate into the step via an exchange mechanism (Figure 4.15) resulting in

surface Pd-Al alloying. The ejected Pd atoms travel across the surface creating islands with a high number of under-coordinated sites. These sites serve as new dissociation sites for MA and the Pd-Al alloy forms on the islands. As TMA exposure increases so does the coverage of carbonaceous species on Pd(111). However, the relatively easy detachment of the Pd atom from the step could result in a "cleaning effect," producing a new dissociation site at step edges for MA. It is hard to tell whether the "octopus-arm" fractal features at the steps formed from the merging of the growing Pd-Al islands with the steps, or if these fractal features originate from the step. The shape of the Pd-Al islands formed at room temperature can be explained by either Pd or Al atom attachment to only nearest neighbors, or diffusion hindrance along island boundaries. Heating lowers this diffusion limitation, and the fractal islands become more compact. Upon heating, aluminum also dissolves into bulk palladium. At the room temperature, Pd and Al alloy on the surface. Upon heating, the aluminum surface concentration decreases and other the Pd-Al intermetallic compounds form in the near surface region. The pit-holes detected by STM are evidence of aluminum diffusion in the bulk.

The role and fate of the carbonaceous species deserve separate discussion. During the initial stages of TMA adsorption, a number of carbonaceous species were detected including ethylidyne ($CCH_{3,\ ads}$) and $CH_{x,\ ads}$ species, ethylidyne being the recombination product of $CH_{x,\ ads}$ ($x \leq 2$) and $CH_3$ species (Figure 4.16). In any case, the formation of ethylidyne and the $CH_{x,\ ads}$ species ($x \leq 2$) results in hydrogen evolution, which likely hydrogenates carbonaceous species followed by product desorption. This is consistent with no carbon at 523 K or very low carbon (~0.18 ML, see Figure 4.12) content that was observed during the early stage of the TMA adsorption at 300 K. In agreement with the

literature, $CH_4$ (methane) and $C_2H_6$ (ethane) were observed by mass spectrometry during the initial exposure of Pd nanoparticles to TMA.[120, 142] Pd(111) demonstrated self-cleaning properties through the hydrogenation of the carbonaceous species. All carbon-containing species disappeared after annealing Pd(111) exposed to 2.5 L TMA at 523 K, and no carbon was detected for low TMA exposures (< 50 L) at 473 K (Figure 4.5). Hydrogenation of the carbonaceous species followed by product desorption is one route for remove carbon. The other route could be the dissolution of the carbon in palladium bulk.[53]

### 4.5.2 TMA on Pt(111)

On Pt(111), TMA dissociates only to the MA species at room temperature—no experimental evidence of aluminum formation was found. According to our DFT calculations, TMA decomposes to MA on the Pt(111) terraces without further dissociation of MA to Al. Dissociation of MA could occur on the step sites (Figure 4.14), but once again this was not observed experimentally.

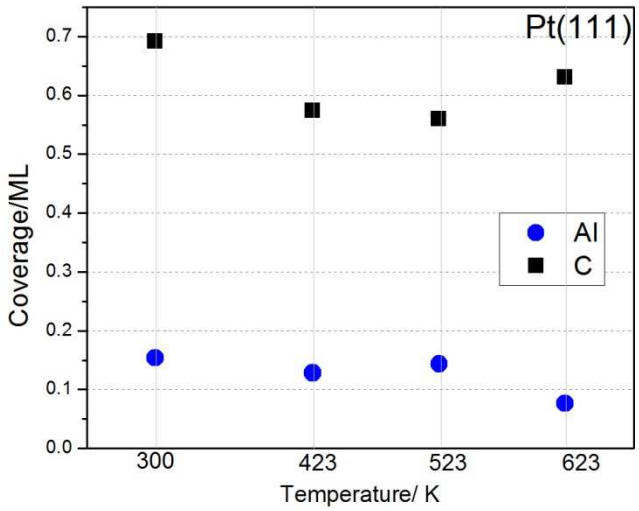


Figure 4.17. Al and C coverages after exposing the Pt(111) surface to 2.5 L TMA at room temperature and annealing up to 623 K.

This is due to the high coverage of carbonaceous species, which block step sites for MA decomposition and/or hinder MA diffusion toward the step. Indeed, the carbon coverage was about 0.7 ML on Pt(111) after 2.5 L TMA exposures at 300 K, compared to 0.18 ML on the Pd(111) surface at the same dosing conditions (Figure 4.17).

Obviously, the diffusion of the MA species through the compact adlayer was obstructed. On the other hand, the DFT calculation showed that the $CH_{3,ads}$ species with coverage of 2/3 ML on the stepped top-site can block MA dissociation. However, it was not possible to differentiate between the two mechanisms preventing MA dissociation based on experimental data. The main conclusion is that the MA species does not dissociate on Pt(111) at 300 K. However, heating at 373 K resulted in MA dissociation as the most of the methyl ligands transferred from Al to the Pt(111) surface.

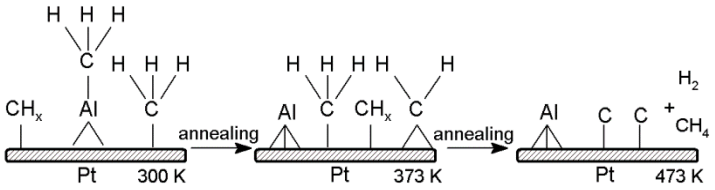


Figure 4.18. Al($CH_3$) reaction mechanism on Pt.

Not surprisingly, the dehydrogenation/hydrogenation of the $CH_{x,ads}$ species occurred on Pt(111) differently than on Pd(111). The overall carbon coverage did not change on Pt(111) during annealing to 623 K (Fig. SI.3). On the other hand, HREELS data indicated that no hydrocarbon species were present on the Pt(111) surface after 473 K. The surface methyl group dehydrogenated, forming methylene and methine groups. Hydrogen atoms recombined and desorbed. Carbon likely formed graphite-like patches and clusters (Figure 4.18).

In previous studies, hydrogen abstraction from surface methyl groups was suggested to be responsible for high carbon incorporation levels found in the epitaxial growth of AlGaAs using TMA as the Al precursor.[119] The absence of the ethylidyne formation on the Pt(111) surface covered with carbon clusters has been previously studied.[143] It was shown that ethylene dehydrogenation and formation of the ethylidyne is completely suppressed after about 30% of the surface is covered with carbon clusters.

The hydrogenation and removal of carbonaceous species is one of the key factors determining the TMA chemistry on Pt(111) and Pd(111). The carbon to aluminum ratio (C:Al) and the aluminum coverage at Al saturation were different on Pd(111) and Pt(111) surfaces with Al coverage reaching 1.4 and 0.96 ML on Pd and Pt, respectively (Figure

4.1). The C:Al ratio follows an opposite trend reaching 2.5 and 1.3 on Pt and Pt, respectively (Figure 4.5). This reflects blocking of the surface by the products of the TMA dissociation. At low exposures (< 50 L) of TMA at 473 K, the Pd(111) surface is very efficient in the hydrogenation and removal of the carbonaceous species. At the same conditions, the Pt(111) surface is covered with the carbonaceous species, which block the adsorption/dissociation sites of TMA. The self-cleaning properties of the Pd(111) surface result in a higher aluminum coverage on Pd(111) than on Pt(111).

## 4.6 Conclusion

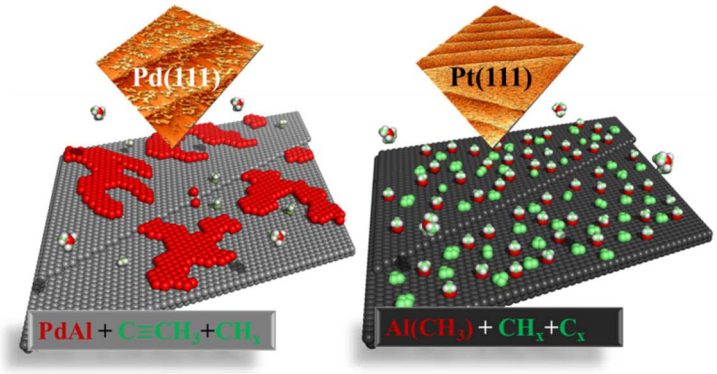


Figure 4.19. Graphical summary of chapter 4.

Using surface sensitive techniques we have shown that the ideal ALD reaction scheme is not fulfilled on Pt(111) and Pd(111) surfaces. On Pd, TMA dissociates to Al, ethylidyne, methyl, and $CH_{x,\,ads}$ groups at room temperature. At this temperature, the availability of Pd steps coupled with the low energy barrier required to remove Pd atoms from steps allow for MA to Al conversion and formation of the Pd-Al alloy on Pd. At room temperature, Al and Pd ejected from step sites form fractal islands consisting of a Pd-Al alloy, and these islands become more compact upon annealing to the higher temperature. TMA partially dissociates to MA on Pt(111) at room temperature. Unlike Pd(111), Pt(111) is unable to efficiently hydrogenate and remove carbon species which results in higher coverages of carbon at the same dosing conditions. The carbon atoms and clusters hinder surface diffusion of MA molecules and block MA decomposition sites at step edges resulting in the uniform coverage of Pt(111) by isolated MA molecules. In contrast to Pd(111), Al does not alloy with the Pt(111) surface due to blockage of the step edges by

carbon species and a higher energy barrier for removal of the Pt atom from step edges (see Figure 4.19).

Fundamental understanding of TMA interaction and surface chemistry on Pt and Pd can benefit the future improvements of ALD on transition metals and the design of the suitable ALD co-reactant and condition.

# CHAPTER 5. SURFACE SCIENCE STUDY OF INITIAL STAGES OF AL2O3 ATOMIC LAYER DEPOSITION ON CU(111)/CUOADS

## 5.1 Abstract

We have investigated the surface chemistry of alumina atomic layer deposition (ALD) using trimethylaluminium (TMA) and oxygen as the precursor and co-reactant on the Cu(111) and $CuO_{ads}$ surface. We mimicked the alumina ALD half-cycles in ultra-high vacuum (UHV) environment and the resultant surface chemistry was studied by X-ray photoelectron spectroscopy (XPS), high resolution electron energy loss spectroscopy (HREELS), and scanning tunneling microscopy (STM) after each ALD half-cycle. According to the XPS and HREELS, Cu(111) is inactive versus TMA. However, after exposing $CuO_{ads}$ to TMA at 473 K HREELS and XPS pointed to the formation of alumina overlayer as the TMA consumed the oxygen in $CuO_{ads}$ lattice and reduced $CuO_{ads}$ surface to $Cu^0$. After the first TMA half-cycle on $CuO_{ads}$, STM images showed that two dimensional alumina islands homogenously cover the surface. Density functional theory (DFT) calculations performed on $CuO_{ads}$ structure determined that at 473 K TMA decomposes to $CH_{3ads}$ and Al in series of exothermic reaction steps. In contrast, TMA adsorption and decomposition is thermodynamically unfavorable on Cu(111) surface, consistent with experimental observation. We used HREELS to investigate the relative occupancy of tetrahedrally and octahedrally coordinated Al ($Al_{oct}$

and $Al_{tet}$) after each alumina ALD half-cycle. TMA half-cycles produce alumina film which predominately consists of octahedral alumina ($Al_{tet}/Al_{oct} \approx 0.3$) while $O_2$ half-cycles favor formation of the tetrahedral alumina ($Al_{tet}/Al_{oct} \approx 0.5$). $O_2$ half-cycles at 623 K remove the residual carbon species after TMA exposure and result in carbon-free alumina film. Reducing the $O_2$ half-cycles temperature to 473 K or replacing $O_2$ with water at 623 K inhibit the alumina growth due to the poisoning of the surface with carbonaceous species.

## 5.2 Introduction

Copper is a widely used material in variety of applications such as water heat exchangers,[144] interconnect and gate electrode in microelectronic,[145, 146] heterogeneous catalyst in low temperature water-gas shift (WGS) and methanol steam reforming.[17, 147, 148] However, the application of Cu is limited due to the failure by corrosion in oxidative environment,[144, 149] diffusion into the adjacent layers in microelectronics,[146, 150] particle instability (sintering) and leaching in Cu-based catalyst.[17] Recently, atomic layer deposition (ALD) of alumina using trimethylaluminium (TMA) has been introduced to form a protective coating on Cu surface preventing corrosion in oxidative environment, diffusion of Cu in the $Cu_2S$ films in photovoltaic (PV) devices, and sintering of Cu-based nanoparticles in liquid-phase hydrogenation reactions.[17, 20, 144, 149, 150] ALD is a variation of chemical vapor deposition (CVD) based on the sequential self-limiting precursor-surface reaction.[5] In ALD the film deposition is performed in a cyclic manner. Typically each ALD cycle consist of two half-cycle reactions in which the surface is exposed to a gaseous precursor and co-reactant separated by purging an inert gas ($N_2$ or Ar) or evacuation of the reaction chamber. Among ALD precursors TMA is the most widely used precursor for the growth of aluminum oxide film (see for instance reference[4] and references therein).

With alumina protective layer showing promising results, different studies have been focused on understanding the TMA interaction and role of the co-reactant (water or oxygen) in alumina ALD growth and final film structure on the Cu surface. The alumina ALD on Cu nanoparticles has been studied by Alba-Rubio et al. using scanning transmission electron microscopy/electron energy loss spectroscopy (STEM/EELS) and

small-angle X-ray scattering (SAXS).[20] Their study showed that 30 cycles of TMA/water ALD is required to reach smooth and nonporous film on copper nanoparticles. Based on the X-ray diffraction and solid state NMR, the final film structure was detected as amorphous alumina. Annealing at 973 K in air opened pores in the alumina film by changing the Al coordination to the well-ordered octahedral structure ($\alpha$-$Al_2O_3$).

O'Neil et al. used Fourier transform infrared (FTIR) vibration peaks of the CO molecule as a structure sensitive probe for understanding the final structure of the alumina ALD using TMA/water on the Cu nanoparticles. They suggested that TMA preferentially covers the under-coordinated copper surface atoms (e.g., steps), leaving terraces open for CO adsorption. Prior to the alumina ALD, they detected the Cu state as the $Cu^0$ by employing X-ray absorption near edge structure (XANES) technique.

In-situ copper-plated quartz crystal microbalance (QCM) was used by Abdulagatov et al. to study the alumina ALD growth on the copper oxide.[144] They proposed that alumina growth occurs with nucleation delay at 450 K using TMA/water. Possible blockage of the copper oxide surface with carbonaceous species and/or lack of initial hydroxyl group were suggested for the initial nucleation delay in alumina film growth.

Although, wide range of characterization techniques has been employed to study the final structure of alumina ALD on copper, the alumina ALD surface chemistry and growth mechanism during the ALD half-cycles remain to be described. Moreover, with ever-increasing demand for decreasing the alumina film thickness in microelectronics and heterogeneous catalysis, understanding the initial precursor-substrate reactions become more crucial. With these applications in mind the substrate itself becomes one of the ALD reactants that can tailor the final structure and performance of the alumina thin film.

Many of the questions concerning the underlying surface chemistry of alumina ALD and the precursor-substrate interactions can be answered by employing surface science characterization techniques in a controlled environment.[34]

Here we report on interaction of TMA/$O_2$ with the Cu(111) and $CuO_{ads}$ during initial alumina ALD half-cycles. We have employed scanning tunneling microscopy (STM), X-ray photoelectron spectroscopy (XPS), high resolution electron energy loss spectroscopy (HREELS) and density functional theory (DFT) in combination with ALD dosing system which allows the investigation of the initial precursor-solid reaction. Preforming alumina ALD half-cycles in step-wise fashion and monitoring the surface species and morphology by XPS, STM and HREELS techniques enable us to elucidate the chemical evolution of the alumina film during each ALD half-cycle.

## 5.3 Experimental methods

The experiments were carried out in Omicron Surface Analysis Cluster system at the Birck Nanotechnology Center (BNC) consisting of an ultra-high vacuum (UHV) preparation chamber and μ-metal analysis chamber with base pressures of $1\times10^{-9}$ mbar and $5\times10^{-11}$ mbar, respectively. The preparation chamber was equipped with a mass spectrometer, an Ar+ sputtering gun, resistive sample heating, internal bakeout heaters (stab-in heaters using vacuum-compatible quartz IR lamps) designed to heat the preparation chamber walls and an ALD precursor-dosing manifold connected through a leak valve. The analysis chamber was equipped with XPS, low energy electron diffraction (LEED), HREELS, STM and resistive sample heating. The sample temperature was measured by a K-type thermocouple spot welded to the stainless steel back plate.

STM images were obtained at room temperature in constant current (topographic) mode with an electrochemically etched W tip. The W tips were conditioned by electron bombardment in preparation chamber. The STM images are displayed in a 2-D top-view representation with dark regions corresponding to lower levels. The STM images were analyzed using WSxM software.[151] The STM height measurement was calibrated by setting the step height to the reticular distance in the clean Cu(111) (0.208 nm).

The HREELS spectra reported here were acquired using an electron beam with a primary energy of 5.0 eV. At beam energy of 5.0 eV, the resolution (full width at half maximum of the elastically reflected electron beam) was about 2.8 meV (~23 $cm^{-1}$). Only spectra in the specular direction were collected. All HREELS spectra have been normalized to the respective primary peak intensity.

The XPS data were acquired using a non-monochromatic Mg Kα X-ray source (hν = 1253.6 eV) at 150 W. High resolution spectra were recorded at a constant pass energy of 20 eV. The resolution of the instrument, which was measured as the full-width at half-maximum (FWHM) of the Cu $2p_{3/2}$, was approximately 1.2 eV. Photoelectrons were ejected at a 45° angle with respect to the surface normal.

XPS data were analyzed with CasaXPS (version 2313Dev64) software.[67] Metallic and oxide Cu were fitted using an asymmetric Gaussian/Lorentzian line shape with tail dampening (CasaXPS Line shape = LF(1.2,1.3,15,60)). Nonmetallic species of C, O and Al were fitted with symmetric Gaussian/Lorentzian line shapes (CasaXPS Line shape = GL(30)). Both Al main peaks, Al 2p and Al 2s overlap with the substrate peak of Cu 3p and Cu 3s, respectively. However, monitoring the sample with the STM and HREELS techniques showed that appearance of Al species on the surface is accompanied by a distinctive shoulder in the Cu 3s region while the Al 2p peak is fully masked by the Cu 3p peak even after several deposition cycles. Therefore, we have chosen the Cu 3s region for analysis of the Al overlayer throughout our work.

To quantify the XPS result, we followed Fadley's approach,[94] which assumes a non-attenuating adlayer at fractional coverage. The XPS model derivation has been explained in details in Section 2.5.1.

Cu(111) single crystal with 10.0 mm diameter and 1.0 mm thickness (Princeton Scientific Corp.) with orientation accuracy of < 0.5° was used. The copper single crystal was routinely cleaned by repeated cycles of $Ar^+$ sputtering and vacuum annealing at 1000 K. During the initial cleaning cycles, the crystals were treated in $5\times10^{-6}$ mbar of $O_2$ at 623-

673 K for 20 minutes to remove traces of the adventitious carbon on the surface. The crystal cleanliness was monitored by XPS, STM and LEED.

The Cu(111) crystal was exposed to TMA (Aldrich, 97%) in the preparation chambers via a leak valve at reported exposure values and temperatures. Prior to dosing TMA several cycles of freeze-pump-thaw were performed for purification. Dosing lines were heated overnight at 423 K, and the lines were filled with TMA and pumped several times before dosing. The exposure values are reported in Langmuir (1 Langmuir = 1 L = $1 \times 10^{-6}$ Torr s). During TMA dosing, ionization gauges were left on for pressure measurement. Similar cycles of freeze-pump-thaw were performed on the water ("Birck Nanograde Water", as SEMI E1.2 with the total organic carbon (TOC) reduced from 1 ppb to 0.25 ppb). The water mini-cylinder has been kept at room temperature during the dosing. A separate dosing line and leak valve has been used for water to avoid cross contamination and any plausible safety hazards by accidental exposure of TMA to water.

### 5.3.1 Computational methods

DFT calculations were performed by Vienna ab initio simulation package (VASP)[98] using project augmented wave (PAW)[99] potential and PW91 exchange-correlation functional.[100] The plane wave cutoff of 400 eV was used. To model Cu(111), the three-layer slab model with (3 × 3) unit cell was used. Long-range ordered $CuO_{ads}$ layer grown on Cu(111) has a well-defined structure in literature.[152-154] The $CuO_{ads}$ film on Cu(111) consists of Cu−O rings with an isolated O located inside the ring. The appearance of this structure is further confirmed by our STM images. To model this structure, a ring including 12 Cu and 13 O atoms on two-layer Cu(111) with (5 × 5) unit cell was used (Figure 5.1). The (4 × 4 × 1) and (2 × 2 × 1) k-point meshes were used to sample the

Brillouin zone for Cu(111) and $CuO_{ads}$, respectively. The bottom-layer Cu atoms were fixed and the remained atoms and adsorbates were relaxed until the residual forces less than 0.02 eV/Å. To prevent the artificial interaction between the repeated slabs along z-direction, 12 Å vacuum was introduced with correction of the dipole moment.

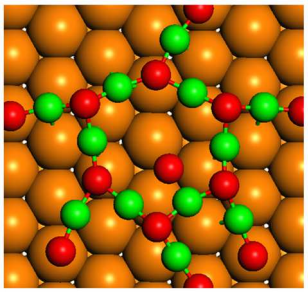

Figure 5.1.The optimized $CuO_{ads}$/Cu(111) structure. The orange, green, and red spheres present Cu in Cu(111) lattice, Cu in $CuO_{ads}$ layer and O atoms, respectively.

## 5.4 Results and Discussion

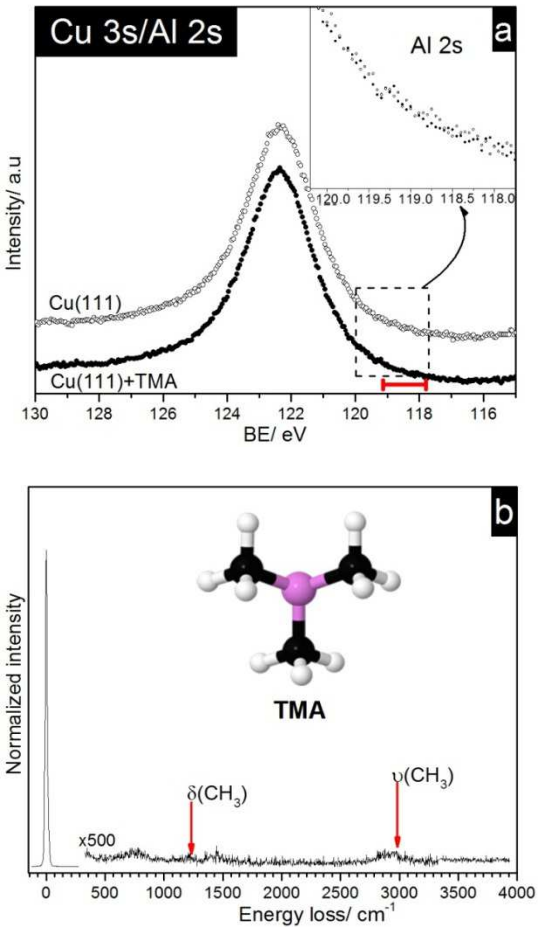


Figure 5.2**.** (a) Cu 3s/Al 2s XPS region for clean Cu(111) (open circles) and after exposure to 2000 L TMA at 473 K (filled circles). The expected BE range for Al or Al−$(CH_3)_x$ species is marked by the red bar. The clean Cu(111) spectrum is vertically shifted for clarity. The inset shows the zoom-in for the Al 2s BE region. XPS spectra of Cu 3s/Al 2s region for both samples are identical. (b) Energy loss spectrum recorded on Cu(111) surface after exposure to 2000 L TMA at 300 K. The expected loss peaks for the methyl ligands are pointed by the red arrows. The chemical structure of TMA is shown inside the figure (Al: pink, C: black, H: white).

To understand the Cu(111) interaction with TMA during the first ALD half-cycle we have investigated the surface species by HREELS and XPS techniques. Using HREELS, the surface chemistry of the TMA molecules can be probed by following the hydrocarbons loss peaks related to the methyl ligands. The HREELS is complimented by the XPS which can elucidate the state, composition and amount of the surface species including Al and C atoms on the surface.

Prior to dosing TMA, the Cu(111) single crystal was characterized by Cu $2p_{3/2}$ peak located at 932.8 eV and no oxygen peak in O 1s region to be in metallic state.[155] Figure 5.2a shows the XPS spectra for the Cu 3s/Al 2s region of the clean Cu(111) surface and after exposure to 2000 L of TMA at 473 K. BEs range for potential Al or $Al-(CH_3)_x$ species is marked by the red bar in XPS spectra and the inset shows the zoom-in to the Al 2s XPS region. After the TMA exposure the Cu 3s/Al 2s region is identical to the clean Cu(111) sample. Absence of any interaction between the metallic copper and TMA precursor has been further confirmed by HREELS technique. The Cu(111) has been exposed to 2000 L TMA at 300 K and the HREELS was recorded at room temperature. The position for $Al-(CH_3)_x$ signature loss peaks at 2946 $\upsilon_{as}(CH_3)$ and 1176 $cm^{-1}$ $\delta_s(CH_3)$ are pointed on the energy loss spectrum by the red arrows.[115, 116, 118] The loss peak around 1200 $cm^{-1}$ can also be due to the $CH_3$ group attached to the Cu(111) surface.[156] The HREELS spectra with typical sensitivity of ~$10^{-3}$ ML,[157] showed no detectable loss peak related to the hydrocarbons attached to Cu or Al center (Figure 5.2b). Therefore, after TMA exposure HREELS and XPS exclude formation of any Al or $Al-(CH_3)_x$ species on the Cu(111). Appearance of two broad and weak features centered around 2800 and 750 $cm^{-1}$ can be due to the adsorption of adventitious hydrocarbon species on the surface.

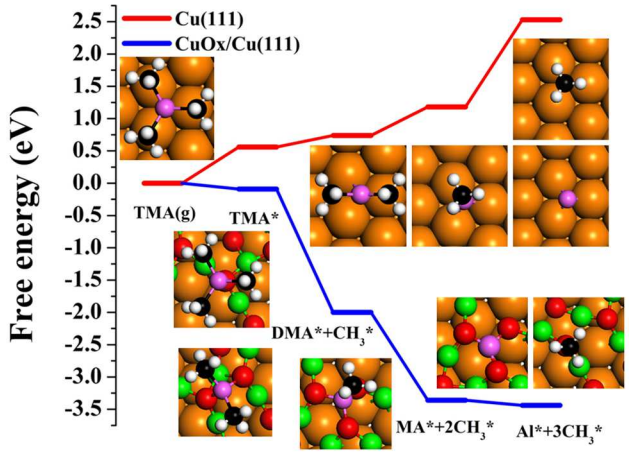


Figure 5.3. Free energy diagrams of TMA dissociation on Cu(111) and $CuO_{ads}$. The insets are the optimized most stable structures of adsorbed TMA, dimethylaluminum (DMA), methylaluminum (MA), Al, and $CH_3$, respectively. The orange, green, pink, black, red, and white spheres represent Cu of Cu(111), Cu of $CuO_{ads}$, Al, C, O, and H atoms, respectively.* Work of Dr. Xiangkui Gu.

DFT calculations has been employed to explain the inactivity of the metallic Cu(111) versus TMA precursor. The free energy diagram of TMA dissociation on Cu(111) at 473 K is shown in Figure 5.3. Comparing the TMA (g) and TMA* (adsorbed) free energy level, one can see that the TMA adsorption on Cu(111) is endothermic by 0.56 eV. This is the sum of the energy loss from the entropy of the gas-phase TMA at 473 K (0.84 eV) and binding energy of -0.28 eV for TMA on Cu(111). This indicates that TMA tends to desorb from the surface, which can prevent the following dissociation of TMA on the Cu(111) surface. Moreover, TMA dissociation on clean Cu(111) is also an endothermic process, the calculated reaction energies for TMA to dimethylaluminum (DMA), DMA to methylaluminum (MA), and MA to Al and $CH_3$ are 0.17, 0.45, and 1.35 eV, respectively.

Alternatively, TMA adsorption and dissociation on $CuO_{ads}$ surface is exothermic (see Figure 5.3). The TMA tends to adsorb at the top position on O in the Cu−O ring via Al atom with the binding energy of -0.93 eV, which is stronger by 0.65 eV than clean Cu(111). The reaction energy of TMA dissociation to DMA is -1.91 eV, and the formed DMA is strongly bonded to the bridge site of the two adjacent O atoms in the Cu−O ring. DMA dissociation to MA process is exothermic by -1.36 eV, and now the Al atom of MA is coordinated with three O atoms, in which one is the isolated O inside the ring. The final step considered, MA dissociation to Al and $CH_3$ is slightly exothermic by -0.09 eV, and the formed Al atom is bonded to three O atoms as the precursor of alumina. Compared to the endothermic process for TMA dissociation on clean Cu(111), the exothermic property on $CuO_{ads}$ film stems from the binding energies of the intermediates involved in TMA dissociation on $CuO_{ads}$ film are stronger than those on clean Cu(111). For instance, the binding energies of DMA, MA, Al, and $CH_3$ are stronger by 2.19, 3.45, 4.35, and 0.54 eV, respectively. From Figure 5.3, it can be found that TMA dissociation on clean Cu(111) is highly unfavorable, however, it is very facile on Cu(111) supported $CuO_{ads}$ film.

The lack of any interaction between TMA and metallic Cu(111) and favorable decomposition pathway on $CuO_{ads}$ points to the necessity of formation of $CuO_{ads}$ layer for the alumina film growth on copper surface. In the following sections, after formation and characterization of the $CuO_{ads}$ layer we will follow each TMA and $O_2$ half-cycle with XPS and HREELS spectra and image the alumina film formation by STM on $CuO_{ads}$ surface.

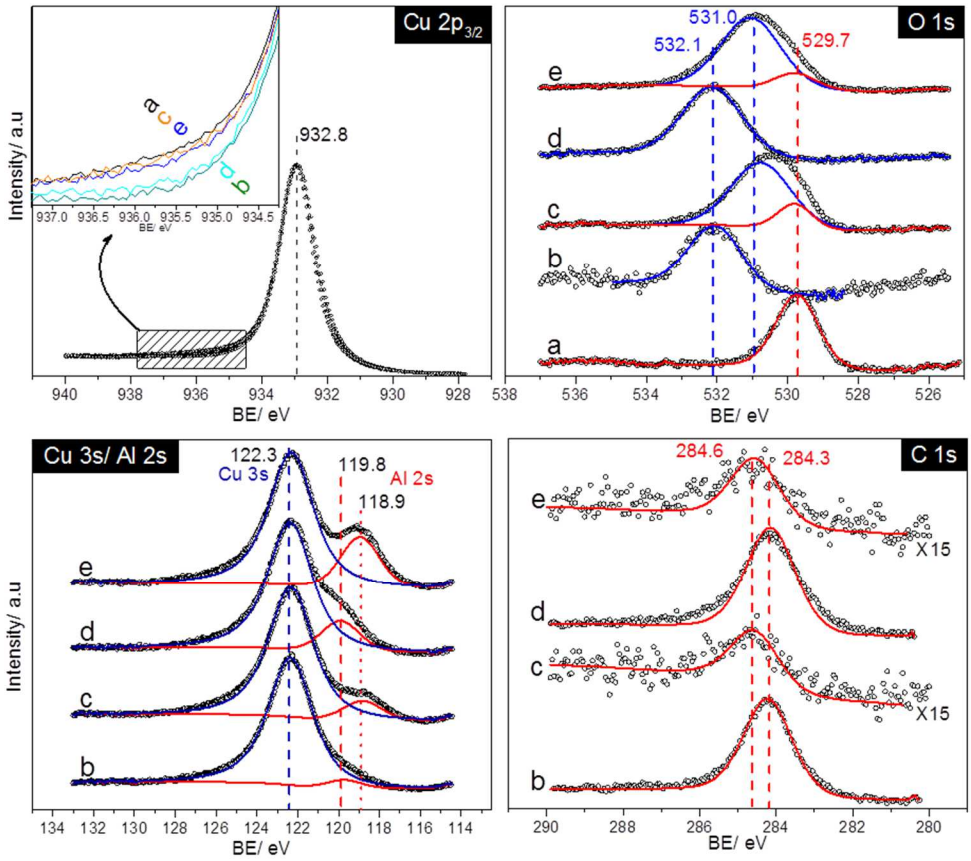


Figure 5.4. Cu $2p_{3/2}$, O 1s, C 1s and Cu 3s/Al 2s XPS spectra. Spectra are normalized to the maximum peak intensity. (a) $CuO_{ads}$ (4500 L $O_2$ at 623 K) (b) 1st TMA half-cycle (2000 L TMA at 473 K) (c) 1st $O_2$ half-cycle (4500 L $O_2$ at 623 K) (d) 2nd TMA half-cycle (e) 2nd $O_2$ half-cycle.

### 5.4.1 $CuO_{ads}$ formation

Prior to TMA and $O_2$ half-cycles the $CuO_{ads}$ layer is formed by treating the Cu(111) surface with $O_2$ at 623 K for 4500 L. The O 1s and Cu $2p_{3/2}$ XPS region for the $CuO_{ads}$ are shown in Figure 5.4a. The O 1s peak is fitted with one component at 529.7 eV for the $CuO_{ads}$ specie. The oxygen exposure causes appearance of a shoulder at ~936.0 eV in the Cu $2p_{3/2}$ region. The C 1s and Cu 3s/Al 2s regions remained unaffected after initial $O_2$ exposure (not shown here). The assignment of the O 1s peak position to the $CuO_{ads}$ is confirmed by the STM images showing the ordered $CuO_{ads}$ structure on the surface.

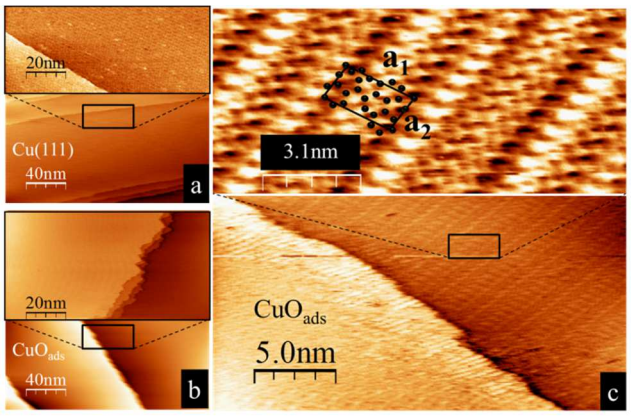


Figure 5.5. STM images (a) Clean Cu(111) (I = 1.0 nA, V = -0.50 V; inset: I = 1.0 nA, V = -1.0 V). (b) After $O_2$ exposure for 4500 L at 623 K. (I = 1.0 nA, V = -0.5 V; inset: I = 0.5 nA, V = -0.50 V). (c) Zoom-in at one of the steps of the $CuO_{ads}$ (I = 1.0 nA, V = -0.5 V). The inset shows the close-up of the well-ordered structure of the $CuO_{ads}$ at atomic resolution (I = 1.1 nA, V = -0.5 V). The unit cell is pointed inside the image. Only oxygen atoms with the black spheres are shown for the hexagonal O–Cu–O rings. The structure appears as the "44"-structure with periodicity of 11.8 ± 0.2 Å and 22.0 ± 0.2 Å along $a_2$ and $a_1$ directions, respectively.

Figure 5.5 shows room temperature STM images of the clean Cu(111) and two dimensional surface copper oxides ($CuO_{ads}$) after dosing the Cu(111) surface with oxygen at 623 K for 4500 L. The step edges of the clean Cu(111) surface are sharp with step height of 0.208 nm (Figure 5.5a). After oxygen exposure the sharp steps in Cu(111) become fuzzy with a saw tooth pattern as the mobility of the Cu atoms at the steps during the scanning time scale causes the blurriness and saw shape profile of the step edges (Figure 5.5b).[152] The STM image in Figure 5.5c shows the small area scan and close-up of atomic structure of the $CuO_{ads}$. Our oxidation condition resemble the Matsumoto et al. study in which they prepared an ordered copper surface oxide by post annealing a copper oxide layer with ~6800 L $O_2$ at 673 K.[152] In agreement with their observation the morphology observed here exhibited the hexagonal O–Cu–O rings forming the "44"-structure implying that the area for the unit cell (shown schematically inside the Figure 5.5c inset) is ~44 times larger than the (1 × 1) unit cell of Cu(111). This structure has a periodicity of 22.0 ± 0.2 Å and 11.8 ± 0.2 Å in the $a_1$ and $a_2$ directions indicated in the image.

### 5.4.2 First TMA half-cycle

We used HREELS technique to probe the surface species and the alumina structure formed on the $CuO_{ads}$ surface during the initial ALD half-cycles. Figure 5.6a shows the HREELS spectra for the first TMA half-cycle consist of 2000 L TMA exposure at 473 K on the $CuO_{ads}$.

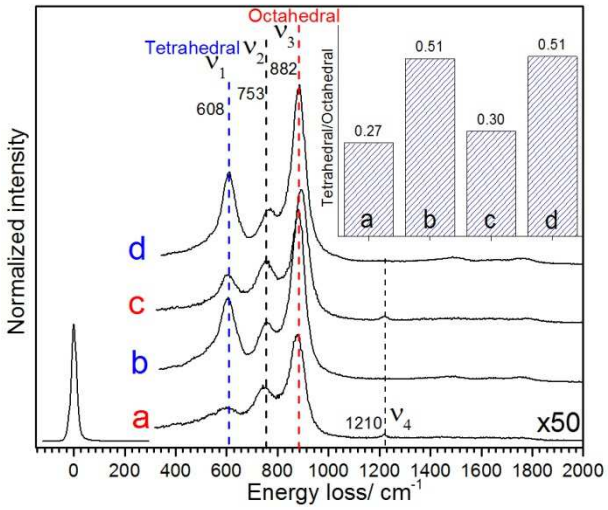


Figure 5.6. HREELS spectra recorded at room temperature for (a) 1st TMA half-cycle (2000 L TMA at 473 K) (b) 1st $O_2$ half-cycle (4500 L $O_2$ at 623 K) (c) 2nd TMA half-cycle (d) 2nd $O_2$ half-cycle; Inset: the ratio between $\upsilon_1$ to $\upsilon_3$ peak areas fraction ($Al_{tet}/Al_{oct}$) is plotted for each TMA and $O_2$ half-cycle.

After exposing the $CuO_{ads}$ to TMA three loss peaks at 608, 747 and most intense one at 880 $cm^{-1}$ were detected. Peaks at 608 ($\upsilon_1$) and 880 $cm^{-1}$ ($\upsilon_3$) have been previously assigned to a group of stretching vibrations between tetrahedrally coordinated $Al^{3+}$ cations ($Al_{tet}$) and their four nearest $O^{2-}$ neighbors ($\upsilon_1$), and to a group of stretching vibrations between octahedrally coordinated $Al^{3+}$ cations ($Al_{oct}$) and their six nearest $O^{2-}$ neighbors ($\upsilon_3$) in alumina film.[158-160] For a well-ordered thick film of alumina a loss peak at ~387 $cm^{-1}$ was previously reported due to the vertical stretching motion of the subsequent in-phase O-Al planes.[160, 161] The presence of the Al cations in both tetrahedral and octahedral coordination in Figure 5.6a suggests that the alumina film consists of transition phase alumina. The peak area fraction for tetrahedral and octahedral alumina

($Al_{tet}/Al_{oct}$) for the first TMA half-cycle is shown in Figure 5.6a inset. The $Al_{tet}/Al_{oct}$ value of 0.27 indicates that upon first TMA exposure the Al is mostly in octahedral coordination.

The loss peak at 740-770 $cm^{-1}$($\upsilon_2$) can be due to "quasi-trihedral" or "quasi-octahedral" alumina on the surface.[162, 163] At the outer surface layer, one of the oxygen coordinated with the Al in a tetrahedral or octahedral site can be missing and that causes the Al cation to relax in the different position and shows intermediate loss peak. Additional studies are required for better understanding of the $\upsilon_2$ peak origin.

The $\upsilon_4$ peak appeared at 1210 $cm^{-1}$ is a signature of the methyl group attached to the copper surface, $\delta_s(CH_3)$.[156, 164] The loss peak for $\delta_s(CH_3)$ group cannot be assigned to the $Al-(CH_3)_x$ species as two strong loss peaks of $\upsilon_s(CH_3)$ and $\upsilon_{as}(CH_3)$ at 2906 and 2947 $cm^{-1}$ are not observed.[115, 119] The absence of the $Al-CH_3$ signature loss peaks and appearance of the $CH_3$ vibration ($\upsilon_4$) attached to the Cu(111) surface indicate that upon adsorption on $CuO_{ads}$, TMA has lost all its methyl ligands and is decomposed to Al. This is consistent with the DFT calculations stating that TMA decomposition to Al and $CH_{3ads}$ is thermodynamically favorable on the copper oxide surface (Figure 5.3). The decomposed methyl groups can desorb as methane ($CH_4$) or dehydrogenate and form isolated carbon atoms/clusters which are quantified by the XPS technique as will be discussed later.

Upon first TMA half-cycle on the $CuO_{ads}$ substrate, the O 1s peak shifted from 529.7 eV to the higher BE at 532.1 eV and the Cu $2p_{3/2}$ shoulder at 936.0 eV disappeared (see Figure 5.4b O1s and Cu $2p_{3/2}$ regions). This suggests that the oxygen in $CuO_{ads}$ lattice is consumed and transferred to the alumina structure during the first TMA half-cycle.

Similar behavior has been observed with alumina ALD on GaAs and Ge(100) substrates and has been referred to as “self-cleaning” where the reduction of interface oxides occurs upon exposure to TMA.[165, 166] We fitted the O 1s region with one component at 532.1 eV for the alumina structure with $Al_{tet}/Al_{oct}$ value of ~0.3 (Figure 5.6a inset).

After first TMA half-cycle one can see appearance of a shoulder in Cu 3s/Al 2s region due to the Al 2s peak overlapping with the Cu 3s at about 119.8 eV. The Cu 3s/Al 2s region was fitted with two components. The first component assigned to the Cu 3s peak originated from the substrate which was kept restrained to the FWHM and peak position of the Cu 3s for the clean Cu(111) surface at 122.3 eV and FWHM of 2.5 eV. The second component was chosen for alumina structure with $Al_{et}/Al_{oct}$ of ~0.3 and was positioned at 119.8 eV after TMA half-cycles (see Figure 5.4b Cu 3s/Al 2s).

A wide asymmetric peak in C 1s region located at 284.3 eV appeared after the first TMA half-cycle. The C 1s peak was fitted with one component at BE of 284.3-284.6 eV. This peak is due to the methyl group attached to the copper surface (observed in Figure 5.6a as $\upsilon_4$ peak) and carbon atoms/clusters left behind after TMA decomposition.

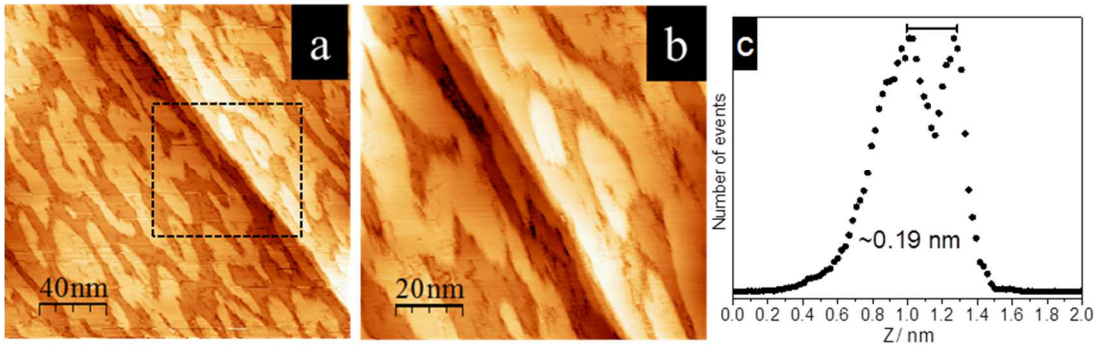


Figure 5.7.STM images (a) 200 nm × 200 nm, I = 1.0 nA, V = -0.75 V and (b) 100 nm × 100 nm, I = 1.0 nA, V = -0.75 V after first TMA half-cycle. The alumina islands uniformly cover the surface. (c) Height histogram showing a bimodal distribution. The distance between the first peak (terraces height) and second peak (islands height) is ~0.19 nm.

Figure 5.7 displays STM images of the copper surface after exposure to the first TMA half-cycle. At first glance, one can see after exposing the $CuO_{ads}$ surface to TMA the step edges become sharp and the long range order of the copper surface oxide has disappeared. As we discussed, the disappearance of the oxygen surface structure is accompanied by the shift in the O 1s peak to the higher BE and disappearance of the shoulder in Cu $2p_{3/2}$. The TMA consumes the oxygen in the surface oxide lattice (self-cleaning) and reduces the $CuO_{ads}$ to the metallic state which is inactive for further TMA decomposition. This mechanism along with possible blockage of the surface with residual carbon can be responsible for the observation of the bare metallic copper patches on the surface.

After first TMA half-cycle, two-dimensional growth of alumina film was established where no second layer formation was observed. There also appears to be no preferential

growth of alumina islands around the step edges as the oxygen atoms in Cu−O rings (Al adsorption sites according to DFT calculations in Figure 5.3) are distributed evenly on the surface. The height histogram corresponding to the islands and flat terraces has been used for the estimation of the islands heights (

Figure 5.7c). The average height for the alumina islands is ~0.19 nm higher than that of the Cu(111) terraces. Observation of bimodal peak distribution in the height histogram confirmed that the islands are flat with uniform height on the Cu(111).

### 5.4.3 First $O_2$ half-cycle

The HREELS spectra for the first $O_2$ half-cycle (4500 L $O_2$ at 623 K) is shown in Figure 5.6b. Comparing to the first TMA half-cycle, the $\upsilon_1$ loss peak intensity at 608 $cm^{-1}$ is increased and the $Al_{tet}/Al_{oct}$ reached 0.51 showing the $O_2$ exposure favors less ordered films with increasing the tetrahedral to octahedral ratio in the alumina structure (see Figure 5.6b inset). The $\upsilon_4$ for the $CH_3$ group attached to copper surface disappears as the oxygen half-cycle removes the residual carbon species on the surface in combustion like reaction.

XPS spectrum for the first $O_2$ half-cycle is shown in Figure 5.4c. Based on the observed structure in HREELS spectra and the O 1s BE for $CuO_{ads}$ (Figure 5.4a) two components were used for fitting the O 1s region. The first component at the lowest BE (529.7 eV) is due to reappearance of the Cu surface oxide phase ($CuO_{ads}$) with 27% area of the total O 1s envelope (Figure 5.4c O 1s). Confirming this assignment a shoulder appeared at about 936.0 eV in the Cu $2p_{2/3}$ region due to formation of the $CuO_{ads}$. The second component at 531.0 (73 % area) belongs to the oxygen in alumina structure with $Al_{tet}/Al_{oct}$ of ~0.5 (Figure 5.6b inset).

The Cu 3s/Al 2s XPS spectra showed a distinctive shoulder at 118.9 eV for the Al 2s (see Figure 5.4c Cu 3s/Al 2s region). The Al 2s is represented with one component for the alumina with $Al_{tet}/Al_{oct}$ of ~0.5 at 118.9 eV. Comparing to the first TMA half-cycle the $O_2$ half-cycle shifted the Al 2s from 119.8 eV to lower BE for about 0.9 eV. The shift in Al 2p peak position toward lower BE (~0.8 eV) has been reported for transition from more ordered α-$Al_2O_3$ (100% octahedral alumina) to amorphous alumina.[167] Here, the shift to lower BE for Al 2s peak is consistent with the $O_2$ half-cycle favoring amorphous alumina by increasing the $Al_{tet}/Al_{oct}$.

A weak C 1s peak can be detected after 1$^{st}$ $O_2$ half-cycle with contribution from the remaining carbon atoms/clusters. In agreement with HREELS (Figure 5.6b) the $O_2$ half-cycle removes the residual carbon species. Later, the $O_2$ effectiveness in removal of the carbonaceous species is elucidated by following the carbon coverage using XPS quantification model. We were not able to image the surface after the $O_2$ half-cycles as the insulation properties of the alumina overlayer impaired the STM. However, the surface can be imaged after consecutive TMA half-cycle as will be discussed below.

### 5.4.4 Second TMA and $O_2$ half-cycles

In the second TMA and $O_2$ half-cycle similar trend for the $Al_{tet}/Al_{oct}$ has been observed by HREELS. The peak area fraction between tetrahedral alumina ($\upsilon_1$) to octahedral alumina ($\upsilon_3$) after second TMA and $O_2$ half-cycle are shown in Figure 5.6 inset c and d. The TMA exposure increases the octahedral component and diminishes the tetrahedral peak intensity while oxygen exposure favors the tetrahedral structure formation. Similar to the first TMA and $O_2$ half-cycle the $Al_{tet}/Al_{oct}$ is ~0.3 and ~0.5 after second TMA and $O_2$ half-cycle, respectively.

After the second TMA half-cycle the O 1s peak shifted to its higher BE value at 532.1 eV (Figure 5.4d O 1s region). Similar to the first TMA exposure the $CuO_{ads}$ component contribution disappeared from O 1s spectra and only the oxygen component at 532.1 eV for the alumina structure with $Al_{tet}/Al_{oct}$ is ~0.3 is observed. The TMA exposure removed the shoulder in the Cu $2p_{3/2}$ region (see Figure 5.4d Cu $2p_{3/2}$ region). The Cu 3s/Al 2s region showed that upon TMA exposure the Al 2s component is shifted to its higher BE value at 119.8 (Figure 5.4d Cu 3s/Al 2s region). This is due to the increase in the $Al_{oct}$ contribution in the alumina structure. In agreement with reappearance of the $\upsilon_4$ peak in HREELS spectra (Figure 5.6c), intense C 1s peak at 284.3 eV is observed after TMA exposure (Figure 5.4d C 1s region). The C 1s peak was fitted with one component for methyl group attached to Cu and carbidic carbon clusters/atoms.

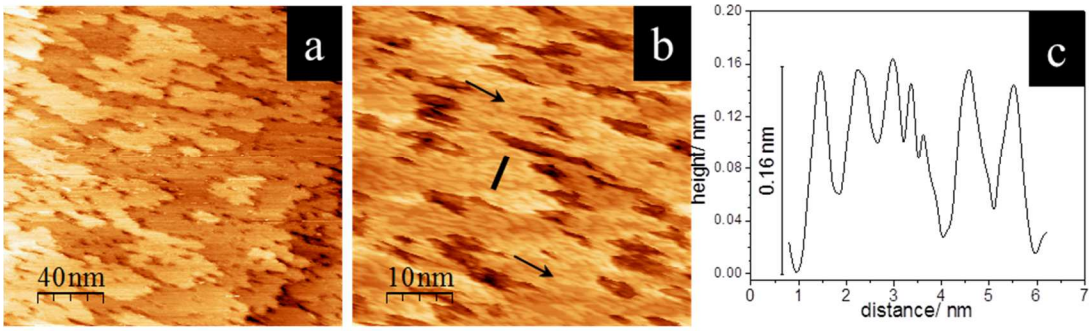


Figure 5.8. Room temperature STM images (a) 200 nm × 200 nm, I = 0.5 nA, V = -0.9 V and (b) 50 nm × 50 nm, I = 0.5 nA, V = -0.9 V after second TMA half-cycle. The alumina islands are stacked on the original Cu surface. (c) Line profile along the solid line indicated in (b). The ridges like features have an apparent height of about 0.16 nm.

Figure 5.8.a and b show the STM images after second TMA half-cycle. The noticeable feature is the appearance of separated planar islands with sharp boundaries that have some ridge-like structure (marked by arrows) formed on top of them. This transition from the single layer alumina island for the first TMA half-cycle (Figure 5.7) to the separated multilayers alumina sheets covered with ridge-like structure suggested that the alumina growth is not limited to the copper oxide surface. Even though the alumina islands covered the copper substrate, the ALD growth can continue on the pre-existing alumina islands after each TMA half-cycle. The line profile in Figure 5.8c shows that the ridge-likes features have an apparent height of about 0.16 nm above the alumina islands which is consistent with the single layer alumina islands average height formed during the first TMA half-cycle on $CuO_{ads}$ surface (see Figure 5.7c).

As concluded from the HREELS the TMA exposure favors more ordered alumina film by increasing the Al cation in octahedral coordination. This tendency for more ordered structure can be responsible for the islands formation with sharp boundaries on the surface.

After the second $O_2$ half-cycle the Al 2s and O 1s peaks are shifted to the lower BE at 118.9 and 531.0 eV respectively (Figure 5.4e Cu 3s/Al 2s and O 1s regions) for the alumina structure with $Al_{tet}/Al_{oct}$ ratio of ~0.5 (see Figure 5.6 inset d). The $CuO_{ads}$ component contribution in O 1s peak area is decreased by three times and is only responsible for 9% of the O 1s peak area which shows the Cu access to the oxygen became limited during the growth process. The second $O_2$ half-cycle effectively removed the majority of carbonaceous species as it is evident from the disappearance of the carbon peak in C 1s region (Figure 5.4e C 1s region) and the $\upsilon_4$ loss peaks in Figure 5.6d.

### 5.4.5 Alumina growth behavior

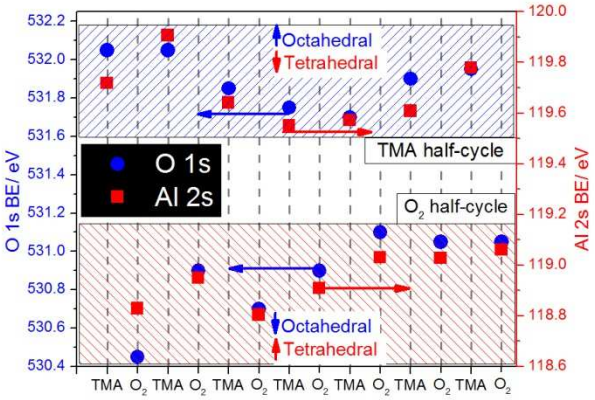


Figure 5.9. The O 1s (blue circle) and Al 2s (red square) peak position for each half-cycle of TMA and $O_2$. Both Al 2s and O 1s BEs show osicalatory behavior. The blue shaded area representing TMA half-cycles with red shaded area showing the $O_2$ half-cycles.

We studied the alumina overlayer growth by performing similar TMA and $O_2$ half-cycles in consecutive manner. Similar to the first two ALD half-cycles, each TMA and $O_2$ half-cycle consists of 2000 L TMA at 473 K and 4500 L $O_2$ at 623 K respectively. Total of 7 cycles of ALD (14 half-cycles of $O_2$ and TMA) have been performed on the $CuO_{ads}$ surface. For brevity the XPS spectra are not shown in here. Figure 5.9 shows the O 1s and Al 2s peak positions after each TMA and $O_2$ half-cycle. As we discussed for the first and second TMA and $O_2$ half-cycles, the common feature in the O 1s and Al 2s peak is the oscillatory behavior of the peak position after each TMA and $O_2$ half-cycle. The oscillatory behavior is in phase for O 1s and Al 2s peak positions, which were found to shift to higher BE after TMA half-cycles and to lower BE after $O_2$ half-cycles. The HREELS spectra showed that the observed oscillatory peak position for both Al and O

core level electrons stem from the changes in the Al ratio in the octahedral and tetrahedral coordination. The TMA half-cycle decreases the $Al_{tet}/Al_{oct}$ (blue shaded region in Figure 5.9) while this ratio increases after each $O_2$ half-cycle (red shaded region in Figure 5.9).

In our study, the changes in the coordination of the Al and O are suggested to be responsible for the apparent shifts in Al 2s and O 1s peak position after each TMA and $O_2$ half-cycle. O 1s and Al 2s peak positions alter between two values as the $Al_{tet}/Al_{oct}$ changes between 0.3 and 0.5 for TMA and $O_2$ half-cycles, respectively. Using high-resolution soft X-ray photoemission spectroscopy, Mulligan et al. reported that Al 2p peak shifts to the higher BE (~0.9 eV) for octahedral alumina comparing to alumina in tetrahedral structure.[168] We cannot detect the Al 2p peak position on Cu substrate but the BE shift to higher value for octahedral alumina structure is in agreement with Al 2s shift to higher BE observed after each TMA exposure that increase the alumina species in octahedral coordination.

Numbers of studies have fitted the O 1s and Al 2p (Al 2s) peaks with the Al−O−Al and Al−OH components at different BEs for the aluminum oxide/hydroxide layer.[114, 169, 170] Lack of any OH related loss peak in our HREELS spectra eliminates the presence of Al−OH species after TMA or $O_2$ half-cycles in our experiments.

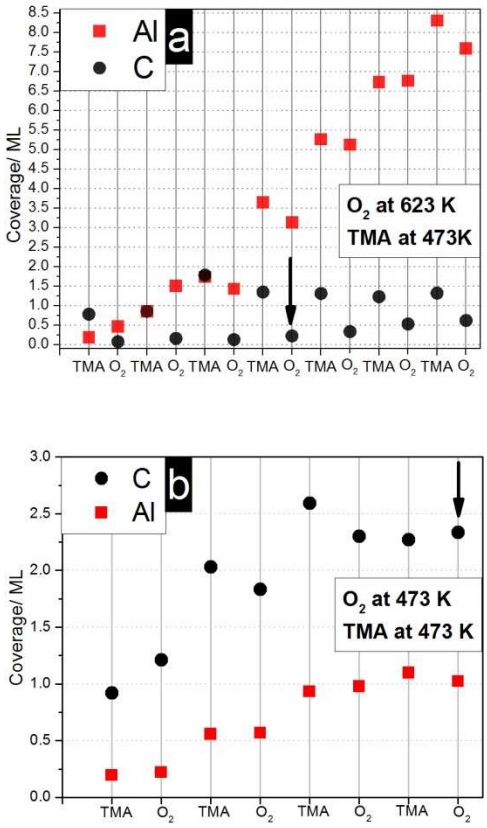


Figure 5.10. Al and C coverages in monolayer (ML) versus TMA half-cycle for 2000 L at 473 K and $O_2$ half-cycle for 4500 L at (a) 623 K and (b) 473 K. The coverage values are calculated by using non-attenuated XPS quantification model. Prior to the first TMA exposure the Cu(111) has been exposed to $O_2$ for 4500 L at 623 K to form the $CuO_{ads}$ required for initial TMA decomposition.

The Al and C coverages in monolayer (ML) calculated based on the non-attenuated XPS quantification model for each TMA (2000 L at 473 K) and $O_2$ half-cycle (4500 L at 623 K) are presented in Figure 5.10a. According to Figure 5.10a the Al coverage continuously increased after each TMA half-cycles and reached to 8.3 ML after 7$^{th}$ TMA exposure. The Al coverage increased after the first and second $O_2$ half-cycle (region I) while it

decreased afterwards upon each $O_2$ half-cycle (region II). This can be explained by the XPS quantification model used for coverage calculation. In region I the Cu surface is not fully covered with the alumina and the carbon species are removed from both Cu and alumina surfaces. Removing the carbon screening effect would increase the Al level in this region. However, after third $O_2$ half-cycle most of the removed carbon species belong to the alumina overlayer and the carbon removal from Cu surface is negligible. The carbon removal from alumina overlayer leaves behind pores and channels in the film that allowed direct sight for signal coming from substrate and intensified the substrate peak intensity in the XPS spectra after each $O_2$ half-cycle. This can result in decrease of the calculated coverage of the overlayer based on the relative intensity of the overlayer peak to the substrate after each oxygen exposure in region II.

The carbon coverage is ~1.0 ML for the first and second TMA half-cycles and becomes stable at ~1.5 ML for further TMA half-cycles. The carbon coverage approaches zero during the first three $O_2$ half-cycles at 623 K (see Figure 5.10a). The $O_2$ half-cycle gradually lost its effectiveness in removing the carbon as it is evident from gradual increase of the carbon level after the fourth $O_2$ half-cycle (pointed by arrow in Figure 5.10a) toward the end. It has been shown by DFT calculation on Cu(111), $O_2$ can dissociate to atomic oxygen on copper surface.[171] The atomic oxygen can react with the carbon clusters or methyl groups on the surface after TMA decomposition and convert them to volatile species. Increasing the Al coverage limits the oxygen access to the Cu surface and consequently decreased the $O_2$ dissociation level. This resulted in the gradual increase in the carbon level after the fourth $O_2$ half-cycle. Incorporation of impurities (particularly carbon) in initial ALD half-cycles is a major concern in oxide dielectrics

where the ultra-thin film (<10 nm) is deposited by initial ALD cycles. In these application it is desired to have carbon-free film to achieve high-quality microelectronic devices.[172] Our results showed that the $O_2$ half-cycles at 623 K can be used after the TMA exposure as an effective method to remove the residual carbon and achieve carbon-free alumina film.

The oxygen exposure temperature plays a major role in the carbon removal and consequent alumina growth behavior. Figure 5.10b shows the Al and C coverages in ML for similar TMA exposures as Figure 5.10a. Only the oxygen exposure temperature was decreased from 623 K to 473 K. The carbon coverage shows that the oxygen exposure at 473 K is not as effective as exposure at 623 K to remove the residual carbons. Decreasing the temperature caused the carbon level to increase after each ALD cycle and became stable at ~2.3 ML. After four ALD cycles the carbon coverage is about 12 times (2.3 ML/0.2 ML) higher than the $O_2$ exposure at 623 K (pointed by the arrow in Figure 5.10a and b). The Al growth observed for the $O_2$ half-cycles at 473 K becomes hindered at about 1.0 ML due to the poisoning of the surface by carbonaceous species.

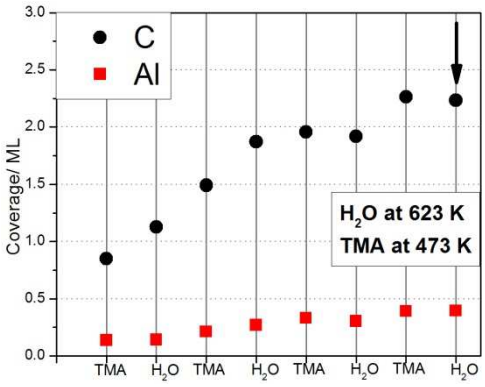


Figure 5.11. Al and C coverages in monolayer (ML) versus the TMA and water half-cycles. Each TMA and water half-cycle include 2000 L TMA exposure at 473 K and 4500 L water at 623 K, respectively. Prior to the first TMA half-cycle the Cu(111) has been exposed to $O_2$ for 4500L at 623 K to form the $CuO_{ads}$ required for initial TMA decomposition.

To further evaluate the effectiveness of second reactant in carbon removal and alumina growth behavior we have replaced the $O_2$ half-cycles with water at 623 K. As it is shown in Figure 5.11, replacing the oxygen with water in the ALD half-cycles is ineffective in removing the residual carbon. The water is only capable of providing the oxygen for the alumina structure as the Al (ML):O (ML) ratio for both water and $O_2$ half-cycles at 673 K reach ~ 0.6 which is close to the alumina stoichiometric value of 2:3. The carbon level increases during the first two cycles and become sable at ~2.3 ML. After fourth ALD cycles (marked by arrow in both Figure 5.10b and Figure 5.11) the carbon coverage for using the water at 623 K is similar to $O_2$ precursor at 473 K (~2.3 ML). However, Figure 5.10b shows that at fourth ALD cycle using the $O_2$ precursor at 473 K, the Al coverage is about 2.5 times higher than water precursor at 623 K. By comparing the Al and C

coverages for the first two ALD cycles in Figure 5.10b and Figure 5.11 one can see that the higher coverage of the Al in Figure 5.10b stems from ability of the oxygen at 473 K to dissociate to atomic oxygen on copper surface and partially burn the residual carbon during the first two $O_2$ half-cycles. However, previous studies showed that Cu(111) surface is hydrophobic and the water molecules is desorbs around 160 K on the Cu(111) surface without any dissociation.[173] Using water at 623 K the carbon level increased through the first two ALD cycles. This carbon poisoning shut down the Al growth on the surface.

Due to lack of surface characterization of the ALD process an ideal picture has been often adopted to explain the ALD surface chemistry and final structure of the alumina film.[4, 8, 27, 174] In the ideal alumina ALD, during the first TMA half-cycle the methyl ligands in TMA molecules are partially exchanged with surface functional groups and the precursor becomes anchored to the surface. The detection of the $CH_4$ group by in-*situ* quadrupole mass spectrometry (QMS) integrated in the ALD reactor is used for confirmation of this mechanism. Based on this picture the co-reactant (usually water) is selected to react with the remaining methyl ligands attached to the Al center. Ideally, the co-reactant provides the missing element (oxygen) and removes the carbon groups on the surface to regenerate the surface for the upcoming TMA half-cycle. However, as it has been demonstrated using HREELS (Figure 5.6) and DFT (Figure 5.3) techniques this ideal picture is not fulfilled on $CuO_{ads}$ surface. The TMA fully decomposes and forms alumina by losing all its methyl ligands upon deposition on the $CuO_{ads}$ at 473 K. The TMA decomposition leaves behind carbon atoms/cluster and methyl group attached to copper surface that can only be removed by using $O_2$ at 623 K.

## 5.5 Conclusion

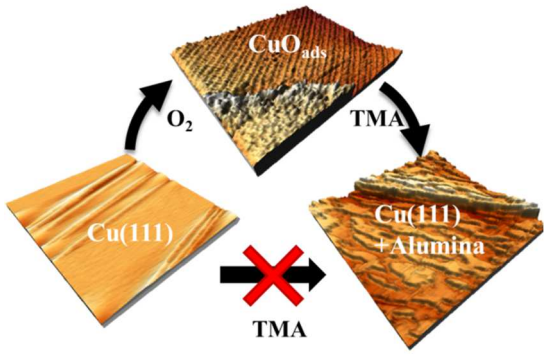


Figure 5.12. Graphical summary of chapter 5.

By employing the surface science characterization techniques and DFT calculations we have shown that the metallic $Cu^0$ surface is inactive versus TMA while TMA decomposition to Al is thermodynamically favorable on $CuO_{ads}$. Exposure of the $CuO_{ads}$ surface to the TMA formed single layered alumina islands that uniformly covered the copper surface. The islands formation progresses until complete reduction of the surface copper oxide structure to the metallic copper ("self-cleaning"). The TMA half-cycles favored ordered octahedral coordinated alumina while oxygen half-cycles increased the portion of the alumina with the tetrahedral structure. The oxygen half-cycle at 623 K removes the carbon atoms/cluster left after TMA decomposition and results in a carbon-free alumina film during the initial ALD cycles. Due to the carbidic nature of the carbon species after TMA decomposition the water is unable to remove the carbon residue. Our study shows that how the future developments in ALD reactants and conditions can benefit from the fundamental understanding of the ALD surface chemistry provided by surface science characterization techniques (see Figure 5.12).

# LIST OF REFERENCES

# LIST OF REFERENCES

1. Suntola, T.; Antson, J. Method for producing compound thin films. November 15, 1977.
2. Shin, S.; Ham, G.; Yeon, H.; Park, J.; Jang, W.; Jeon, H., Atomic layer deposition: overview and applications. *Han'guk Chaelyo Hakhoechi* **2013,** 23, (8), 405-422.
3. Miikkulainen, V.; Leskela, M.; Ritala, M.; Puurunen, R. L., Crystallinity of inorganic films grown by atomic layer deposition: Overview and general trends. *J. Appl. Phys. (Melville, NY, U. S.)* **2013,** 113, (2), 021301/1-021301/101.
4. Puurunen, R. L., Surface chemistry of atomic layer deposition: A case study for the trimethylaluminum/water process. *Journal of Applied Physics* **2005,** 97, (12).
5. Leskelä, M.; Ritala, M., Atomic layer deposition (ALD): from precursors to thin film structures. *Thin Solid Films* **2002,** 409, (1), 138-146.
6. Hämäläinen, J.; Ritala, M.; Leskelä, M., Atomic Layer Deposition of Noble Metals and Their Oxides. *Chemistry of Materials* **2013,** 26, (1), 786-801.
7. Lu, J.; Elam, J. W.; Stair, P. C., Synthesis and Stabilization of Supported Metal Catalysts by Atomic Layer Deposition. *Accounts of Chemical Research* **2013,** 46, (8), 1806-1815.
8. Johnson, R. W.; Hultqvist, A.; Bent, S. F., A brief review of atomic layer deposition: from fundamentals to applications. *Materials Today*, (0).
9. Kim, H.; Lee, H.-B.-R.; Maeng, W. J., Applications of atomic layer deposition to nanofabrication and emerging nanodevices. *Thin Solid Films* **2009,** 517, (8), 2563-2580.
10. Thiele, E. W., Relation between Catalytic Activity and Size of Particle. *Industrial & Engineering Chemistry* **1939,** 31, (7), 916-920.
11. Shekhar, M.; Wang, J.; Lee, W.-S.; Williams, W. D.; Kim, S. M.; Stach, E. A.; Miller, J. T.; Delgass, W. N.; Ribeiro, F. H., Size and Support Effects for the Water–Gas Shift Catalysis over Gold Nanoparticles Supported on Model Al2O3 and TiO2. *Journal of the American Chemical Society* **2012,** 134, (10), 4700-4708.
12. Lu, J.; Stair, P. C., Low-Temperature ABC-Type Atomic Layer Deposition: Synthesis of Highly Uniform Ultrafine Supported Metal Nanoparticles. *Angewandte Chemie International Edition* **2010,** 49, (14), 2547-2551.
13. Lu, J.; Low, K.-B.; Lei, Y.; Libera, J. A.; Nicholls, A.; Stair, P. C.; Elam, J. W., Toward atomically-precise synthesis of supported bimetallic nanoparticles using atomic layer deposition. *Nat Commun* **2014,** 5.
14. Christensen, S. T.; Feng, H.; Libera, J. L.; Guo, N.; Miller, J. T.; Stair, P. C.; Elam, J. W., Supported Ru−Pt Bimetallic Nanoparticle Catalysts Prepared by Atomic Layer Deposition. *Nano Letters* **2010,** 10, (8), 3047-3051.

15. Lei, Y.; Liu, B.; Lu, J.; Lobo-Lapidus, R. J.; Wu, T.; Feng, H.; Xia, X.; Mane, A. U.; Libera, J. A.; Greeley, J. P.; Miller, J. T.; Elam, J. W., Synthesis of Pt–Pd Core–Shell Nanostructures by Atomic Layer Deposition: Application in Propane Oxidative Dehydrogenation to Propylene. *Chemistry of Materials* **2012,** 24, (18), 3525-3533.
16. Feng, H.; Lu, J.; Stair, P.; Elam, J., Alumina Over-coating on Pd Nanoparticle Catalysts by Atomic Layer Deposition: Enhanced Stability and Reactivity. *Catalysis Letters* **2011,** 141, (4), 512-517.
17. O'Neill, B. J.; Jackson, D. H. K.; Crisci, A. J.; Farberow, C. A.; Shi, F.; Alba-Rubio, A. C.; Lu, J.; Dietrich, P. J.; Gu, X.; Marshall, C. L.; Stair, P. C.; Elam, J. W.; Miller, J. T.; Ribeiro, F. H.; Voyles, P. M.; Greeley, J.; Mavrikakis, M.; Scott, S. L.; Kuech, T. F.; Dumesic, J. A., Stabilization of Copper Catalysts for Liquid-Phase Reactions by Atomic Layer Deposition. *Angewandte Chemie International Edition* **2013,** 52, (51), 13808-13812.
18. Lu, J.; Fu, B.; Kung, M. C.; Xiao, G.; Elam, J. W.; Kung, H. H.; Stair, P. C., Coking- and Sintering-Resistant Palladium Catalysts Achieved Through Atomic Layer Deposition. *Science* **2012,** 335, (6073), 1205-1208.
19. Lu, J.; Liu, B.; Greeley, J. P.; Feng, Z.; Libera, J. A.; Lei, Y.; Bedzyk, M. J.; Stair, P. C.; Elam, J. W., Porous Alumina Protective Coatings on Palladium Nanoparticles by Self-Poisoned Atomic Layer Deposition. *Chemistry of Materials* **2012,** 24, (11), 2047-2055.
20. Alba-Rubio, A. C.; O'Neill, B. J.; Shi, F.; Akatay, C.; Canlas, C.; Li, T.; Winans, R.; Elam, J. W.; Stach, E. A.; Voyles, P. M.; Dumesic, J. A., Pore Structure and Bifunctional Catalyst Activity of Overlayers Applied by Atomic Layer Deposition on Copper Nanoparticles. *ACS Catalysis* **2014**, 1554-1557.
21. Lu, J.; Stair, P. C., Nano/Subnanometer Pd Nanoparticles on Oxide Supports Synthesized by AB-type and Low-Temperature ABC-type Atomic Layer Deposition: Growth and Morphology. *Langmuir* **2010,** 26, (21).
22. Lee, J.; Jackson, D. H. K.; Li, T.; Winans, R. E.; Dumesic, J. A.; Kuech, T. F.; Huber, G. W., Enhanced stability of cobalt catalysts by atomic layer deposition for aqueous-phase reactions. In Energy Environ. Sci., 2014; Vol. 7, pp 1657-1660.
23. Buttry, D. A.; Ward, M. D., Measurement of interfacial processes at electrode surfaces with the electrochemical quartz crystal microbalance. *Chemical Reviews* **1992,** 92, (6), 1355-1379.
24. Rahtu, A.; Alaranta, T.; Ritala, M., In Situ Quartz Crystal Microbalance and Quadrupole Mass Spectrometry Studies of Atomic Layer Deposition of Aluminum Oxide from Trimethylaluminum and Water. *Langmuir* **2001,** 17, (21), 6506-6509.
25. Elam, J. W.; Groner, M. D.; George, S. M., Viscous flow reactor with quartz crystal microbalance for thin film growth by atomic layer deposition. *Review of Scientific Instruments* **2002,** 73, (8), 2981-2987.
26. Goldstein, D. N.; McCormick, J. A.; George, S. M., Al2O3 Atomic Layer Deposition with Trimethylaluminum and Ozone Studied by in Situ Transmission FTIR Spectroscopy and Quadrupole Mass Spectrometry. *J. Phys. Chem. C* **2008,** 112, (49), 19530-19539.

27. Juppo, M.; Rahtu, A.; Ritala, M.; Leskelä, M., In Situ Mass Spectrometry Study on Surface Reactions in Atomic Layer Deposition of Al2O3 Thin Films from Trimethylaluminum and Water. *Langmuir* **2000,** 16, (8), 4034-4039.
28. Mulley, J. S.; Bennett, R. A.; Dhanak, V. R., Adsorption, orientation and thermal decomposition of copper(II) hexafluoroacetylacetonate on rutile TiO2(110). *Surface Science* **2008,** 602, (18).
29. Ma, Q.; Zaera, F., Chemistry of Cu(acac)2 on Ni(110) and Cu(110) surfaces: Implications for atomic layer deposition processes. *Journal of Vacuum Science & Technology A* **2013,** 31, (1), -.
30. Donnelly, V. M.; Gross, M. E., Copper metalorganic chemical vapor deposition reactions of hexafluoroacetylacetonate Cu(I) vinyltrimethylsilane and bis (hexafluoroacetylacetonate) Cu(II) adsorbed on titanium nitride. *Journal of Vacuum Science & Technology A: Vacuum, Surfaces, and Films* **1993,** 11, (1), 66-77.
31. Lin, W. B.; Wiegand, B. C.; Nuzzo, R. G.; Girolami, G. S., Mechanistic studies of palladium thin film growth from palladium(II) beta-diketonates .1. Spectroscopic studies of the reactions of bis(hexafluoroacetylacetonato)palladium(II) on copper surfaces. *Journal of the American Chemical Society* **1996,** 118, (25).
32. Weber, M. J.; Mackus, A. J. M.; Verheijen, M. A.; Longo, V.; Bol, A. A.; Kessels, W. M. M., Atomic Layer Deposition of High-Purity Palladium Films from Pd(hfac)2 and H2 and O2 Plasmas. *The Journal of Physical Chemistry C* **2014,** 118, (16), 8702-8711.
33. Stone, P.; Poulston, S.; Bennett, R. A.; Bowker, M., Scanning tunnelling microscopy investigation of sintering in a model supported catalyst: nanoscale Pd on TiO2(110). *Chemical Communications* **1998**, (13), 1369-1370.
34. Zaera, F., The Surface Chemistry of Atomic Layer Depositions of Solid Thin Films. *The Journal of Physical Chemistry Letters* **2012,** 3, (10), 1301-1309.
35. Ma, Q.; Guo, H.; Gordon, R. G.; Zaera, F., Uptake of Copper Acetamidinate ALD Precursors on Nickel Surfaces. *Chemistry of Materials* **2009,** 22, (2), 352-359.
36. Ma, Q.; Zaera, F.; Gordon, R. G., Thermal chemistry of copper(I)-N,N′-di-sec-butylacetamidinate on Cu(110) single-crystal surfaces. *Journal of Vacuum Science & Technology A* **2012,** 30, (1), -.
37. Elko-Hansen, T. D. M.; Ekerdt, J. G., XPS Investigation of the Atomic Layer Deposition Half Reactions of Bis(N-tert-butyl-N′-ethylpropionamidinato) Cobalt(II). *Chemistry of Materials* **2014,** 26, (8), 2642-2646.
38. Dhakal, D.; Waechtler, T.; Schulz, S. E.; Gessner, T.; Lang, H.; Mothes, R.; Tuchscherer, A., Surface chemistry of a Cu(I) beta-diketonate precursor and the atomic layer deposition of Cu2O on SiO2 studied by x-ray photoelectron spectroscopy. *Journal of Vacuum Science & Technology A* **2014,** 32, (4), -.
39. Janocha, E.; Pettenkofer, C., ALD of ZnO using diethylzinc as metal-precursor and oxygen as oxidizing agent. *Applied Surface Science* **2011,** 257, (23), 10031-10035.
40. Ye, L.; Gougousi, T., Indium Diffusion and Native Oxide Removal during the Atomic Layer Deposition (ALD) of TiO2 Films on InAs(100) Surfaces. *ACS Applied Materials & Interfaces* **2013,** 5, (16), 8081-8087.

41. Massimo Tallarida and Dieter, S., In situ ALD experiments with synchrotron radiation photoelectron spectroscopy. *Semiconductor Science and Technology* **2012,** 27, (7), 074010.
42. Wang, X.; Tabakman, S. M.; Dai, H., Atomic Layer Deposition of Metal Oxides on Pristine and Functionalized Graphene. *Journal of the American Chemical Society* **2008,** 130, (26), 8152-8153.
43. Mack, J. F.; Van Stockum, P. B.; Iwadate, H.; Prinz, F. B., A combined scanning tunneling microscope–atomic layer deposition tool. *Review of Scientific Instruments* **2011,** 82, (12), -.
44. Mack, J. F.; Van Stockum, P. B.; Yemane, Y. T.; Logar, M.; Iwadate, H.; Prinz, F. B., Observing the Nucleation Phase of Atomic Layer Deposition In Situ. *Chemistry of Materials* **2012,** 24, (22), 4357-4362.
45. Adelmann, C.; Cuypers, D.; Tallarida, M.; Rodriguez, L. N. J.; De Clercq, A.; Friedrich, D.; Conard, T.; Delabie, A.; Seo, J. W.; Locquet, J.-P.; De Gendt, S.; Schmeisser, D.; Van Elshocht, S.; Caymax, M., Surface Chemistry and Interface Formation during the Atomic Layer Deposition of Alumina from Trimethylaluminum and Water on Indium Phosphide. *Chemistry of Materials* **2013,** 25, (7), 1078-1091.
46. http://www.evactron.com/
47. Basnet, G.; Kevin Schoelz, J.; Xu, P.; Barber, S. D.; Ackerman, M. L.; Thibado, P. M., Etch-stop method for reliably fabricating sharp yet mechanically stable scanning tunneling microscope tips. *Journal of Vacuum Science & Technology B* **2013,** 31, (4), -.
48. Ibe, J. P.; Bey, P. P.; Brandow, S. L.; Brizzolara, R. A.; Burnham, N. A.; DiLella, D. P.; Lee, K. P.; Marrian, C. R. K.; Colton, R. J., On the electrochemical etching of tips for scanning tunneling microscopy. *Journal of Vacuum Science & Technology A* **1990,** 8, (4), 3570-3575.
49. Biffis, A.; Zecca, M.; Basato, M., Palladium metal catalysts in Heck C・C coupling reactions. *Journal of Molecular Catalysis A: Chemical* **2001,** 173, (1–2), 249-274.
50. Molnár, Á.; Sárkány, A.; Varga, M., Hydrogenation of carbon–carbon multiple bonds: chemo-, regio- and stereo-selectivity. *Journal of Molecular Catalysis A: Chemical* **2001,** 173, (1–2), 185-221.
51. Blaser, H.-U.; Indolese, A.; Schnyder, A.; Steiner, H.; Studer, M., Supported palladium catalysts for fine chemicals synthesis. *Journal of Molecular Catalysis A: Chemical* **2001,** 173, (1–2), 3-18.
52. Zhu, G.; Han, J.; Zemlyanov, D. Y.; Ribeiro, F. H., Temperature Dependence of the Kinetics for the Complete Oxidation of Methane on Palladium and Palladium Oxide†. *The Journal of Physical Chemistry B* **2004,** 109, (6), 2331-2337.
53. Gabasch, H.; Kleimenov, E.; Teschner, D.; Zafeiratos, S.; Hävecker, M.; Knop-Gericke, A.; Schlögl, R.; Zemlyanov, D.; Aszalos-Kiss, B.; Hayek, K.; Klötzer, B., Carbon incorporation during ethene oxidation on Pd(111) studied by in situ X-ray photoelectron spectroscopy at. *Journal of Catalysis* **2006,** 242, (2), 340-348.
54. Newton, M. A.; Belver-Coldeira, C.; Martinez-Arias, A.; Fernandez-Garcia, M., Dynamic in situ observation of rapid size and shape change of supported Pd nanoparticles during CO/NO cycling. *Nat Mater* **2007,** 6, (7), 528-532.

55. Elam, J. W.; Zinovev, A.; Han, C. Y.; Wang, H. H.; Welp, U.; Hryn, J. N.; Pellin, M. J., Atomic layer deposition of palladium films on Al2O3 surfaces. *Thin Solid Films* **2006,** 515, (4), 1664-1673.
56. Feng, H.; Elam, J. W.; Libera, J. A.; Setthapun, W.; Stair, P. C., Palladium Catalysts Synthesized by Atomic Layer Deposition for Methanol Decomposition. *Chemistry of Materials* **2010,** 22, (10).
57. Feng, H.; Libera, J. A.; Stair, P. C.; Miller, J. T.; Elam, J. W., Subnanometer Palladium Particles Synthesized by Atomic Layer Deposition. *ACS Catal.* **2011,** 1, (6), 665-673.
58. Rikkinen, E.; Santasalo-Aarnio, A.; Airaksinen, S.; Borghei, M.; Viitanen, V.; Sainio, J.; Kauppinen, E. I.; Kallio, T.; Krause, A. O. I., Atomic Layer Deposition Preparation of Pd Nanoparticles on a Porous Carbon Support for Alcohol Oxidation. *The Journal of Physical Chemistry C* **2011,** 115, (46), 23067-23073.
59. Goldstein, D. N.; George, S. M., Surface poisoning in the nucleation and growth of palladium atomic layer deposition with Pd(hfac)(2) and formalin. *Thin Solid Films* **2011,** 519, (16), 5339-5347.
60. Anderson, V. R.; Leick, N.; Clancey, J. W.; Hurst, K. E.; Jones, K. M.; Dillon, A. C.; George, S. M., Atomic Layer Deposition of Platinum Nanoparticles on Titanium Oxide and Tungsten Oxide Using Platinum(II) Hexafluoroacetylacetonate and Formalin as the Reactants. *The Journal of Physical Chemistry C* **2014,** 118, (17), 8960-8970.
61. Parmeter, J. E., Copper CVD chemistry on a reactive substrate: bis(hexafluoroacetylacetonato)copper and hfacH on platinum (111). *The Journal of Physical Chemistry* **1993,** 97, (44), 11530-11541.
62. Lei, Y.; Lu, J.; Zhao, H.; Liu, B.; Low, K.-B.; Wu, T.; Libera, J. A.; Greeley, J. P.; Chupas, P. J.; Miller, J. T.; Elam, J. W., Resolving Precursor Deligation, Surface Species Evolution, and Nanoparticle Nucleation during Palladium Atomic Layer Deposition. *The Journal of Physical Chemistry C* **2013,** 117, (21), 11141-11148.
63. Horcas, I.; Fernandez, R.; Gomez-Rodriguez, J. M.; Colchero, J.; Gomez-Herrero, J.; Baro, A. M., WSXM: A software for scanning probe microscopy and a tool for nanotechnology. *Rev. Sci. Instrum.* **2007,** 78, (1).
64. Schrödinger, L. *The PyMOL Molecular Graphics System*, Version 1.5.0.4.
65. Mezhenny, S.; Lyubinetsky, I.; Choyke, W. J.; Yates, J. T., Electron stimulated decomposition of adsorbed hexafluoroacetylacetonate Cu(I) vinyltrimethylsilane, Cu(I)(hfac)(vtms). *Journal of Applied Physics* **1999,** 85, (6), 3368-3373.
66. Diebold, U.; Li, M.; Dulub, O.; Hebenstreit, E. L. D.; Hebenstreit, W., The relationship between bulk and surface properties of rutile TiO2(110). *Surface Review and Letters* **2000,** 7, (5-6).
67. Fairley, N., *CasaXPS*, 2.3.16dev85; Casa Software Ltd. In 2011.
68. Yu, J. C.; Yu; Ho; Jiang; Zhang, Effects of F- Doping on the Photocatalytic Activity and Microstructures of Nanocrystalline TiO2 Powders. *Chemistry of Materials* **2002,** 14, (9), 3808-3816.
69. Gabasch, H.; Unterberger, W.; Hayek, K.; Kloetzer, B.; Kleimenov, E.; Teschner, D.; Zafeiratos, S.; Haevecker, M.; Knop-Gericke, A.; Schloegl, R.; Han, J.; Ribeiro, F. H.; Aszalos-Kiss, B.; Curtin, T.; Zemlyanov, D., In situ XPS study of Pd(111) oxidation at

elevated pressure, Part 2: Palladium oxidation in the 10(-1) mbar range. *Surface Science* **2006,** 600, (15).
70. Lin, W. B.; Wiegand, B. C.; Nuzzo, R. G.; Girolami, G. S., Mechanistic studies of palladium thin film growth from palladium(II) beta-diketonates .1. Spectroscopic studies of the reactions of bis(hexafluoroacetylacetonato)palladium(II) on copper surfaces. *J Am Chem Soc* **1996,** 118, (25), 5977-5987.
71. Hantsche, H., High resolution XPS of organic polymers, the scienta ESCA300 database. By G. Beamson and D. Briggs, Wiley, Chichester 1992, 295 pp., hardcover, £ 65.00, ISBN 0-471-93592-1. *Advanced Materials* **1993,** 5, (10), 778-778.
72. Cohen, S. L.; Liehr, M.; Kasi, S., Mechanisms of copper chemical vapor deposition. *Applied Physics Letters* **1992,** 60, (1), 50-52.
73. Cohen, S. L.; Liehr, M.; Kasi, S., Selectivity in copper chemical vapor deposition. *Applied Physics Letters* **1992,** 60, (13), 1585-1587.
74. Lin, W. B.; Nuzzo, R. G.; Girolami, G. S., Mechanistic studies of palladium thin film growth from palladium(II) beta-diketonates .2. Kinetic analysis of the transmetalation reaction of bis(hexafluoroacetylacetonato)palladium(II) on copper surfaces. *J Am Chem Soc* **1996,** 118, (25), 5988-5996.
75. Cheung, T. T. P., Lineshape studies of the X-ray photoemission of small metal clusters. *Surface Science* **1983,** 127, (2), L129-L134.
76. Diebold, U., The surface science of titanium dioxide. *Surface Science Reports* **2003,** 48, (5-8).
77. Horton, J. H.; Shapter, J. G.; Cheng, T.; Lennard, W. N.; Norton, P. R., STM investigation of a Cu organometallic complex adsorbed on Si(111)-(7 × 7). *Surface Science* **1997,** 375, (2–3), 171-182.
78. Rayner, D. G.; Mulley, J. S.; Bennett, R. A., Copper deposition on TiO2 from copper (II) hexafluoroacetylacetonate. *Journal of Vacuum Science & Technology A* **2012,** 31, (1), 01A121.
79. Siedle, A. R.; Newmark, R. A.; Pignolet, L. H., Structure of palladium bis(hexafluoroacetylacetonate) and the systematics of its acid-base chemistry. *Inorganic Chemistry* **1983,** 22, (16), 2281-2286.
80. Bennett, R. A.; Stone, P.; Bowker, M., Pd nanoparticle enhanced re-oxidation of non-stoichiometric TiO2: STM imaging of spillover and a new form of SMSI. *Catal Lett* **1999,** 59, (2-4), 99-105.
81. Calò, V.; Nacci, A.; Monopoli, A.; Cotugno, P., Heck Reactions with Palladium Nanoparticles in Ionic Liquids: Coupling of Aryl Chlorides with Deactivated Olefins. *Angewandte Chemie International Edition* **2009,** 48, (33), 6101-6103.
82. Zhu, G.; Han, J.; Zemlyanov, D. Y.; Ribeiro, F. H., Temperature Dependence of the Kinetics for the Complete Oxidation of Methane on Palladium and Palladium Oxide†. *J. Phys. Chem. B* **2004,** 109, (6), 2331-2337.
83. Williams, W. D.; Bollmann, L.; Miller, J. T.; Delgass, W. N.; Ribeiro, F. H., Effect of molybdenum addition on supported platinum catalysts for the water–gas shift reaction. *Applied Catalysis B: Environmental* **2012,** 125, (0), 206-214.
84. Newton, M. A.; Belver-Coldeira, C.; Martinez-Arias, A.; Fernandez-Garcia, M., Dynamic In Situ observation of rapid size and shape change of supported Pd nanoparticles during CO/NO cycling. *Nat. Mater.* **2007,** 6, (7), 528-532.

85. Mulla, S. S.; Chen, N.; Cumaranatunge, L.; Blau, G. E.; Zemlyanov, D. Y.; Delgass, W. N.; Epling, W. S.; Ribeiro, F. H., Reaction of NO and O2 to NO2 on Pt: Kinetics and catalyst deactivation. *Journal of Catalysis* **2006,** 241, (2), 389-399.
86. Berlowitz, P. J.; Peden, C. H. F.; Goodman, D. W., Kinetics of carbon monoxide oxidation on single-crystal palladium, platinum, and iridium. *The Journal of Physical Chemistry* **1988,** 92, (18), 5213-5221.
87. Hübert, T.; Boon-Brett, L.; Black, G.; Banach, U., Hydrogen sensors – A review. *Sensors and Actuators B: Chemical* **2011,** 157, (2), 329-352.
88. Randeniya, L. K.; Martin, P. J.; Bendavid, A., Detection of hydrogen using multi-walled carbon-nanotube yarns coated with nanocrystalline Pd and Pd/Pt layered structures. *Carbon* **2012,** 50, (5), 1786-1792.
89. Li, W.; Liang, C.; Zhou, W.; Qiu, J.; Zhou; Sun, G.; Xin, Q., Preparation and Characterization of Multiwalled Carbon Nanotube-Supported Platinum for Cathode Catalysts of Direct Methanol Fuel Cells. *The Journal of Physical Chemistry B* **2003,** 107, (26), 6292-6299.
90. Liang, X.; Li, J.; Yu, M.; McMurray, C. N.; Falconer, J. L.; Weimer, A. W., Stabilization of Supported Metal Nanoparticles Using an Ultrathin Porous Shell. *ACS Catalysis* **2011,** 1, (10), 1162-1165.
91. Fu, B.; Lu, J.; Stair, P. C.; Xiao, G.; Kung, M. C.; Kung, H. H., Oxidative dehydrogenation of ethane over alumina-supported Pd catalysts. Effect of alumina overlayer. *Journal of Catalysis* **2013,** 297, (0), 289-295.
92. Gomez-Rodriguez, J. M.; Baro, A. M.; Vazquez, L.; Salvarezza, R. C.; Vara, J. M.; Arvia, A. J., Fractal surfaces of gold and platinum electrodeposits: dimensionality determination by scanning tunneling microscopy. *The Journal of Physical Chemistry* **1992,** 96, (1), 347-350.
93. Moulder, J. F.; Chastain, J.; King, R. C., *Handbook of X-ray photoelectron spectroscopy: a reference book of standard spectra for identification and interpretation of XPS data*. Physical Electronics Eden Prairie, MN: 1995.
94. Fadley, C. S., Basic concepts of x-ray photoelectron spectroscopy. *Electron Spectrosc. Theory, Tech. Appl.* **1978,** 2, 1-156.
95. Scofield, J. H., Hartree-Slater subshell photoionization cross-sections at 1254 and 1487 eV. *J. Electron. Spectrosc. Relat. Phenom.* **1976,** 8, (2), 129-137.
96. Yeh, J. J.; Lindau, I., Atomic subshell photoionization cross sections and asymmetry parameters: $1 \leqslant Z \leqslant 103$. *At. Data Nucl. Data Tables* **1985,** 32, (1), 1-155.
97. Powell, C. J.; Jablonski, A., *NIST Electron Effective-Attenuation-Length Database* - Version 1.3, National Institute of Standards and Technology. In Gaithersburg, MD: 2011.
98. Kresse, G.; Furthmüller, J., Efficiency of ab-initio total energy calculations for metals and semiconductors using a plane-wave basis set. *Computational Materials Science* **1996,** 6, (1), 15-50.
99. Blöchl, P. E., Projector augmented-wave method. *Physical Review B* **1994,** 50, (24), 17953-17979.
100. Perdew, J. P.; Wang, Y., Accurate and simple analytic representation of the electron-gas correlation energy. *Physical Review B* **1992,** 45, (23), 13244-13249.

101. Henkelman, G.; Uberuaga, B. P.; Jónsson, H., A climbing image nudged elastic band method for finding saddle points and minimum energy paths. *The Journal of Chemical Physics* **2000,** 113, (22), 9901-9904.
102. Wilson, K.; Lee, A. F.; Hardacre, C.; Lambert, R. M., Electronic, Structural, and Reactive Properties of Ultrathin Aluminum Oxide Films on Pt(111). *The Journal of Physical Chemistry B* **1998,** 102, (10), 1736-1744.
103. Olefjord, I.; Mathieu, H. J.; Marcus, P., Intercomparison of surface analysis of thin aluminium oxide films. *Surface and Interface Analysis* **1990,** 15, (11), 681-692.
104. Matolın, V.; Stará, I.; Tsud, N.; Johánek, V., XPS and TDS study of CO interaction with Pd–AlOx systems. *Progress in Surface Science* **2001,** 67, (1), 167-181.
105. Johánek, V.; Tsud, N.; Matolín, V.; Stará, I., TPD and XPS study of the CO adsorption on transition-SP metal systems: Pd and Al. *Vacuum* **2001,** 63, (1), 15-22.
106. Johanek, V.; Stara, I.; Matolín, V., Role of Pd–Al bimetallic interaction in CO adsorption and catalytic properties of bulk PdAl alloy: XPS, ISS, TDS, and SIMS study. *Surface science* **2002,** 507, 92-98.
107. Shutthanandan, V.; Saleh, A. A.; Shivaparan, N.; Smith, R., Growth of ultrathin Pd films on Al (001) surfaces. *Surface science* **1996,** 350, (1), 11-20.
108. Stadlmayr, W.; Rameshan, C.; Weilach, C.; Lorenz, H.; Hävecker, M.; Blume, R.; Rocha, T.; Teschner, D.; Knop-Gericke, A.; Zemlyanov, D.; Penner, S.; Schlögl, R.; Rupprechter, G.; Klötzer, B.; Memmel, N., Temperature-Induced Modifications of PdZn Layers on Pd(111). *The Journal of Physical Chemistry C* **2010,** 114, (24), 10850-10856.
109. Rameshan, C.; Stadlmayr, W.; Penner, S.; Lorenz, H.; Mayr, L.; Hävecker, M.; Blume, R.; Rocha, T.; Teschner, D.; Knop-Gericke, A.; Schlögl, R.; Zemlyanov, D.; Memmel, N.; Klötzer, B., In situ XPS study of methanol reforming on PdGa near-surface intermetallic phases. *Journal of Catalysis* **2012,** 290, (0), 126-137.
110. Rameshan, C.; Lorenz, H.; Mayr, L.; Penner, S.; Zemlyanov, D.; Arrigo, R.; Haevecker, M.; Blume, R.; Knop-Gericke, A.; Schlögl, R.; Klötzer, B., CO2-selective methanol steam reforming on In-doped Pd studied by in situ X-ray photoelectron spectroscopy. *Journal of Catalysis* **2012,** 295, (0), 186-194.
111. Wilson, K.; Brake, J.; Lee, A. F.; Lambert, R. M., Growth morphology and electronic properties of ultrathin Al films on Pt(111). *Surface Science* **1997,** 387, (1–3), 257-268.
112. Colgan, E. G., Phase formation and dissociation in the thin-film Pt/Al system. *Journal of Applied Physics* **1987,** 62, (4), 1224-1231.
113. Lee, A. F.; Wilson, K.; Lambert, R. M., Structure and stability of the platinum/aluminium interface: alloying and substrate vacancy formation on Pt{111}/Al. *Surface Science* **2000,** 446, (1–2), 145-152.
114. Sherwood, P. M. A., Introduction to Studies of Aluminum and its Compounds by XPS. *Surface Science Spectra* **1998,** 5, (1), 1-3.
115. Kvisle, S.; Rytter, E., Infrared matrix isolation spectroscopy of trimethylgallium, trimethylaluminium and triethylaluminium. *Spectrochimica Acta Part A: Molecular Spectroscopy* **1984,** 40, (10), 939-951.
116. Soto, C.; Wu, R.; Bennett, D. W.; Tysoe, W. T., Infrared Spectroscopy of Trimethylaluminum and Dimethylaluminum chloride adsorbed on Alumina. *Chemistry of Materials* **1994,** 6, (10), 1705-1711.

117. Soto, C.; Tysoe, W. T., The reaction pathway for the growth of alumina on high surface area alumina and in ultrahigh vacuum by a reaction between trimethyl aluminum and water. *Journal of Vacuum Science & Technology A* **1991,** 9, (5), 2686-2695.
118. Cabrera, W.; Halls, M. D.; Povey, I. M.; Chabal, Y. J., Surface Oxide Characterization and Interface Evolution in Atomic Layer Deposition of Al2O3 on InP(100) Studied by in Situ Infrared Spectroscopy. *The Journal of Physical Chemistry C* **2014,** 118, (11), 5862-5871.
119. Hill, J. J.; Aquino, A. A.; Mulcahy, C. P. A.; Harwood, N.; Jones, A. C.; Jones, T. S., The adsorption and thermal decomposition of trimethylaluminium and dimethylaluminium hydride on GaAs(100). *Surface Science* **1995,** 340, (1–2), 49-56.
120. Kesmodel, L. L.; Gates, J. A., Ethylene adsorption and reaction on Pd(111): An angle-dependent eels analysis. *Surface Science Letters* **1981,** 111, (3), L747-L754.
121. Sock, M.; Eichler, A.; Surnev, S.; Andersen, J. N.; Klötzer, B.; Hayek, K.; Ramsey, M. G.; Netzer, F. P., High-resolution electron spectroscopy of different adsorption states of ethylene on Pd(1 1 1). *Surface Science* **2003,** 545, (1–2), 122-136.
122. Baró, A. M.; Ibach, H., Thermal evolution and decomposition of ethylene on Pt(111). *The Journal of Chemical Physics* **1981,** 74, (7), 4194-4199.
123. Ibach, H.; Lehwald, S., Identification of surface radicals by vibration spectroscopy: Reactions of CH2, C2H4, and H2 on Pt (111). *Journal of Vacuum Science and Technology* **1978,** 15, (2), 407-415.
124. Zhou, Y.; Feng, W. M.; Henderson, M. A.; Roop, B.; White, J. M., Surface photochemistry: products retained on platinum(111) during photolysis of adsorbed methyl bromide. *Journal of the American Chemical Society* **1988,** 110, (13), 4447-4448.
125. Henderson, M. A.; Mitchell, G. E.; White, J. M., The chemisorption of methyl halides (Cl, Br and I) on Pt(111). *Surface Science* **1987,** 184, (1–2), L325-L331.
126. Solymosi, F.; Klivényi, G., HREELS study of CH3I and CH3 adsorbed on Rh(111) surface. *Journal of Electron Spectroscopy and Related Phenomena* **1993,** 64–65, (0), 499-506.
127. Aquino, A. A.; Mulcahy, C. P. A.; Jones, T. S., Spectroscopic identification of the reaction intermediates in the thermal decomposition of trimethylindium at GaAs(100) surfaces. *Surface Science* **1995,** 344, (3), L1231-L1238.
128. Kato, H. S.; Noh, J.; Hara, M.; Kawai, M., An HREELS Study of Alkanethiol Self-Assembled Monolayers on Au(111). *The Journal of Physical Chemistry B* **2002,** 106, (37), 9655-9658.
129. Smirnov, M. Y.; Gall, N. R.; Cholach, A. R.; Gorodetskii, V. V.; Tontegode, A. Y.; Rut'kov, E. V.; Zemlyanov, D. Y., Hreels study and catalytic significance of low-temperature interaction of isolated carbon atoms with hydrogen on Pt(111). *Catalysis Letters* **1991,** 8, (1), 101-106.
130. Smirnov, M. Y.; Gorodetskii, V. V.; Cholach, A. R.; Zemlyanov, D. Y., Hydrogenation of isolated atoms and small clusters of carbon on Pt(111) surface: HREELS/TDS studies. *Surface Science* **1994,** 311, (3), 308-321.
131. Goldstein, D. N.; McCormick, J. A.; George, S. M., Al2O3 Atomic Layer Deposition with Trimethylaluminum and Ozone Studied by in Situ Transmission FTIR

Spectroscopy and Quadrupole Mass Spectrometry. *The Journal of Physical Chemistry C* **2008,** 112, (49), 19530-19539.
132. Eilertsen, J. L.; Rytter, E.; Ystenes, M., In situ FTIR spectroscopy during addition of trimethylaluminium (TMA) to methylaluminoxane (MAO) shows no formation of MAO–TMA compounds. *Vibrational Spectroscopy* **2000,** 24, (2), 257-264.
133. Kaltchev, M.; Thompson, A. W.; Tysoe, W. T., Reflection-absorption infrared spectroscopy of ethylene on palladium (111) at high pressure. *Surface Science* **1997,** 391, (1–3), 145-149.
134. Gates, J. A.; Kesmodel, L. L., Thermal evolution of acetylene and ethylene on Pd(111). *Surface Science* **1983,** 124, (1), 68-86.
135. Howard Fairbrother, D.; Peng, X. D.; Viswanathan, R.; Stair, P. C.; Trenary, M.; Fan, J., Carbon-carbon coupling of methyl groups on Pt(111). *Surface Science Letters* **1993,** 285, (1–2), L455-L460.
136. Kesmodel, L. L.; Dubois, L. H.; Somorjai, G. A., Dynamical LEED study of C2H2 and C2H4 chemisorption on Pt(111): evidence for the ethylidyne group. *Chemical Physics Letters* **1978,** 56, (2), 267-271.
137. Batabyal, R.; Mahato, J. C.; Das, D.; Roy, A.; Dev, B. N., Self-organized one-atom thick fractal nanoclusters via field-induced atomic transport. *Journal of Applied Physics* **2013,** 114, (6), -.
138. Witten, T. A.; Sander, L. M., Diffusion-limited aggregation. *Physical Review B* **1983,** 27, (9), 5686-5697.
139. Zhang, Z.; Lagally, M. G., Atomistic Processes in the Early Stages of Thin-Film Growth. *Science* **1997,** 276, (5311), 377-383.
140. Brune, H.; Röder, H.; Boragno, C.; Kern, K., Microscopic View of Nucleation on Surfaces. *Physical Review Letters* **1994,** 73, (14), 1955-1958.
141. Land, T. A.; Michely, T.; Behm, R. J.; Hemminger, J. C.; Comsa, G., Direct observation of surface reactions by scanning tunneling microscopy: Ethylene→ethylidyne→carbon particles→graphite on Pt(111). *The Journal of Chemical Physics* **1992,** 97, (9), 6774-6783.
142. Stacchiola, D.; Tysoe, W. T., The Kinetics of Ethylidyne Formation from Ethylene on Pd(111). *Journal of Physical Chemistry C* **2009,** 113, (19).
143. Johánek, V.; De La Ree, A. B.; Hemminger, J. C., Scanning Tunneling Microscopy Investigation of the Conversion of Ethylene to Carbon Clusters and Graphite on Pt(111). *The Journal of Physical Chemistry C* **2009,** 113, (11), 4441-4444.
144. Abdulagatov, A. I.; Yan, Y.; Cooper, J. R.; Zhang, Y.; Gibbs, Z. M.; Cavanagh, A. S.; Yang, R. G.; Lee, Y. C.; George, S. M., Al2O3 and TiO2 Atomic Layer Deposition on Copper for Water Corrosion Resistance. *ACS Appl. Mater. Interfaces* **2011,** 3, (12), 4593-4601.
145. Ma, Y.; Evans, D. R.; Nguyen, T.; Ono, Y.; Hsu, S. T., Fabrication and characterization of sub-quarter-micron MOSFETs with a copper gate electrode. *Electron Device Letters, IEEE* **1999,** 20, (5), 254-255.
146. Kelly, J.; Parks, C.; Demarest, J.; Li, J.; Penny, C., Microstructure Evolution of Copper in Nanoscale Interconnect Features. In *Copper Electrodeposition for Nanofabrication of Electronics Devices*, Kondo, K.; Akolkar, R. N.; Barkey, D. P.; Yokoi, M., Eds. Springer New York: 2014; pp 115-130.

147. Gokhale, A. A.; Dumesic, J. A.; Mavrikakis, M., On the Mechanism of Low-Temperature Water Gas Shift Reaction on Copper. *Journal of the American Chemical Society* **2008,** 130, (4), 1402-1414.
148. Gu, X.-K.; Li, W.-X., First-Principles Study on the Origin of the Different Selectivities for Methanol Steam Reforming on Cu(111) and Pd(111). *The Journal of Physical Chemistry C* **2010,** 114, (49), 21539-21547.
149. Chang, M. L.; Cheng, T. C.; Lin, M. C.; Lin, H. C.; Chen, M. J., Improvement of oxidation resistance of copper by atomic layer deposition. *Applied Surface Science* **2012,** 258, (24), 10128-10134.
150. Riha, S. C.; Jin, S.; Baryshev, S. V.; Thimsen, E.; Wiederrecht, G. P.; Martinson, A. B. F., Stabilizing Cu2S for Photovoltaics One Atomic Layer at a Time. *ACS Applied Materials & Interfaces* **2013,** 5, (20), 10302-10309.
151. Horcas, I.; Fernández, R.; Gómez-Rodríguez, J. M.; Colchero, J.; Gómez-Herrero, J.; Baro, A. M., WSXM: A software for scanning probe microscopy and a tool for nanotechnology. *Review of Scientific Instruments* **2007,** 78, (1), -.
152. Matsumoto, T.; Bennett, R. A.; Stone, P.; Yamada, T.; Domen, K.; Bowker, M., Scanning tunneling microscopy studies of oxygen adsorption on Cu(111). *Surface Science* **2001,** 471, (1–3), 225-245.
153. Jensen, F.; Besenbacher, F.; Lægsgaard, E.; Stensgaard, I., Oxidation of Cu(111): two new oxygen induced reconstructions. *Surface Science* **1991,** 259, (3), L774-L780.
154. Jensen, F.; Besenbacher, F.; Stensgaard, I., Two new oxygen induced reconstructions on Cu(111). *Surface Science* **1992,** 269–270, (0), 400-404.
155. Biesinger, M. C.; Lau, L. W. M.; Gerson, A. R.; Smart, R. S. C., Resolving surface chemical states in XPS analysis of first row transition metals, oxides and hydroxides: Sc, Ti, V, Cu and Zn. *Applied Surface Science* **2010,** 257, (3), 887-898.
156. Chao-Ming, C.; Bent, B. E., Methyl radical adsorption on Cu(111): Bonding, reactivity, and the effect of coadsorbed iodine. *Surface Science* **1992,** 279, (1–2), 79-88.
157. Vattuone, L.; Savio, L.; Rocca, M., High Resolution Electron Energy Loss Spectroscopy (HREELS): A Sensitive and Versatile Surface Tool. In *Surface Science Techniques*, Bracco, G.; Holst, B., Eds. Springer Berlin Heidelberg: 2013; Vol. 51, pp 499-529.
158. Lee, M. B.; Lee, J. H.; Frederick, B. G.; Richardson, N. V., Surface structure of ultra-thin A12O3 films on metal substrates. *Surface Science* **2000,** 448, (2–3), L207-L212.
159. Frank, M.; Wolter, K.; Magg, N.; Heemeier, M.; Kühnemuth, R.; Bäumer, M.; Freund, H.-J., Phonons of clean and metal-modified oxide films: an infrared and HREELS study. *Surface Science* **2001,** 492, (3), 270-284.
160. Jiang, Z.; Huang, W.; Zhang, Z.; Zhao, H.; Tan, D.; Bao, X., Thermal decomposition of Mo(CO)6 on thin Al2O3 film: A combinatorial investigation by XPS and UPS. *Surface Science* **2007,** 601, (3), 844-851.
161. Wu, M.-C.; Goodman, D. W., Particulate Cu on Ordered Al2O3: Reactions with Nitric Oxide and Carbon Monoxide. *The Journal of Physical Chemistry* **1994,** 98, (39), 9874-9881.
162. Zhou, R.-S.; Snyder, R. L., Structures and transformation mechanisms of the [eta], [gamma] and [theta] transition aluminas. *Acta Crystallographica Section B* **1991,** 47, (5), 617-630.

163. Sohlberg, K.; Pantelides, S. T.; Pennycook, S. J., Surface Reconstruction and the Difference in Surface Acidity between γ- and η-Alumina. *Journal of the American Chemical Society* **2000,** 123, (1), 26-29.
164. Lin, J. L.; Bent, B. E., Iodomethane dissociation on Cu(111): Bonding and chemistry of adsorbed methyl groups. *Journal of Vacuum Science & Technology A* **1992,** 10, (4), 2202-2209.
165. Milojevic, M.; Contreras-Guerrero, R.; Lopez-Lopez, M.; Kim, J.; Wallace, R. M., Characterization of the "clean-up" of the oxidized Ge(100) surface by atomic layer deposition. *Appl. Phys. Lett.* **2009,** 95, (21), 212902/1-212902/3.
166. Hinkle, C. L.; Sonnet, A. M.; Vogel, E. M.; McDonnell, S.; Hughes, G. J.; Milojevic, M.; Lee, B.; Aguirre-Tostado, F. S.; Choi, K. J.; Kim, H. C.; Kim, J.; Wallace, R. M., GaAs interfacial self-cleaning by atomic layer deposition. *Appl. Phys. Lett.* **2008,** 92, (7), 071901/1-071901/3.
167. Kovács, K.; Perczel, I. V.; Josepovits, V. K.; Kiss, G.; Réti, F.; Deák, P., In situ surface analytical investigation of the thermal oxidation of Ti–Al intermetallics up to 1000 °C. *Applied Surface Science* **2002,** 200, (1–4), 185-195.
168. Mulligan, A.; Dhanak, V.; Kadodwala, M., A High-Resolution Photoemission Study of Nanoscale Aluminum Oxide Films on NiAl(110). *Langmuir* **2005,** 21, (18), 8312-8318.
169. Kloprogge, J. T.; Duong, L. V.; Wood, B. J.; Frost, R. L., XPS study of the major minerals in bauxite: Gibbsite, bayerite and (pseudo-)boehmite. *Journal of Colloid and Interface Science* **2006,** 296, (2), 572-576.
170. Alexander, M. R.; Thompson, G. E.; Beamson, G., Characterization of the oxide/hydroxide surface of aluminium using x-ray photoelectron spectroscopy: a procedure for curve fitting the O 1s core level. *Surface and Interface Analysis* **2000,** 29, (7), 468-477.
171. Xu, Y.; Mavrikakis, M., Adsorption and dissociation of O2 on Cu(1 1 1). Thermochemistry, reaction barrier and the effect of strain. *Surf. Sci.* **2001,** 494, (2), 131-144.
172. Choi, M.; Lyons, J. L.; Janotti, A.; Van, d. W. C. G., Impact of carbon and nitrogen impurities in high-κ dielectrics on metal-oxide-semiconductor devices. *Appl. Phys. Lett.* **2013,** 102, (14), 142902/1-142902/4.
173. Yamamoto, S.; Andersson, K.; Bluhm, H.; Ketteler, G.; Starr, D. E.; Schiros, T.; Ogasawara, H.; Pettersson, L. G. M.; Salmeron, M.; Nilsson, A., Hydroxyl-Induced Wetting of Metals by Water at Near-Ambient Conditions. *The Journal of Physical Chemistry C* **2007,** 111, (22), 7848-7850.
174. Zaera, F., The surface chemistry of thin film atomic layer deposition (ALD) processes for electronic device manufacturing. *Journal of Materials Chemistry* **2008,** 18, (30), 3521-3526.

VITA

VITA

# Amir Gharachorlou

Email:agharach@gmail.com

## ▶ Education

***Doctor of Philosophy, Chemical Engineering*** **DEC 2014**

- *Purdue University – West Lafayette, IN*
- Research area**: Heterogeneous catalysis, Surface Science**, XPS, Organometallic precursors ,Catalysis, Atomic Layer Deposition
- Advisors: Fabio H. Ribeiro and W. Nicholas Delgass

***Master of Science, Polymer Engineering*** **2006-2008**

- *Amirkabir University* – Tehran
- Research area: Polymer Blends and Copolymers Phase Behavior, Polymer Rheology and Characterization

**Bachelor of Science**, Polymer and Color Engineering **2002-2006**

- *Amirkabir University* – Tehran

## ▶ Research Experience

Graduate Research Assistant, Purdue University **2010 - Present**

- Designed and built an Ultra High Vacuum (**UHV) compatible Atomic Layer Deposition (ALD)** reactor which allows full characterization of ALD technique using **surface science tools (XPS, STM LEED)** , in collaboration with Argonne national lab.
- Studied the fundamental mechanism of formation of protective alumina overlayer on transition metal single crystals using **ambient pressure XPS at synchrotron radiation source** BESSY II to overcome the surface science pressure gap.
- Developed a reproducible protocol to use ALD technique for synthesis of **model catalysts** systems of Pd, Pt, Cu with uniform particle size on $TiO_2$ and $SiO_2$ as oxide supports and inverse model catalysts consist of $TiO_x$ layer on Pt and Pd surface for fundamental understanding of heterogeneous catalysis.
- Designed a system and a protocol to conduct **reproducible kinetic measurements for ethylene hydrogenation reaction** using custom made ambient pressure reaction cell connected to GC and FTIR for kinetics modeling on Pd and Pt catalysts and TiOx/Pt inverse catalyst.
- Studied the fundamental mechanism of alumina ($Al_2O_3$) overcoats on supported transition metal nanoparticles to prevent deactivation by **coking and sintering in high-temperature applications** of heterogeneous catalysts in **oxidative dehydrogenation of ethane** over alumina-supported Pd.

- Master's Research Project, Amirkabir University of Technology, Tehran **2006 – 2008**
- Designed, prepared and executed series of experiment to employ rheological behavior of polymer blends to understand the phase separation dynamic and compatibilizer effect on phase diagram.

## ► Industrial Experience

*Technical Engineer* **:BASF Polyurethanes (Elastogran Pars)** , Tehran **2007-2008**

- Tested new PU products for automotive components, footwear and refrigerator panels.
- Started and equipped the quality control lab for the first BASF Polyurethanes system house in Qazvin, Iran.

*Technical Consultant:* **German Technical Cooperation (GTZ) Proklima,** Tehran **2008-2009**

- Technology transfer, procurement of new equipment and provision of engineering services required for adapting the existing or new donated machine to match requirement to phase-out ozone-damaging fluorinated greenhouse gas (CFC, HCFC, HFC) emissions in PU industry

## ► Communication Skills

### Oral and Poster Presentations:

- **A. Gharachorlou**, M. D. Detwiler, Y. Lei, J. Lu, J. W. Elam, D. Y. Zemlyanov, J. F. Greeley, W. N. Delgass and F. H. Ribeiro *Surface Science Studies of Alumina Overlayers on Pd(111), Pt(111) and Cu(111) Surfaces Prepared by Atomic Layer Deposition*, EFRC PI meeting, Washington, D.C, July 2013. (Oral presentation)
- **A. Gharachorlou**, M. D. Detwiler, Y. Lei, J. Lu, J. W. Elam, D. Y. Zemlyanov, J. F. Greeley, W. N. Delgass and F. H. Ribeiro, *Reaction of trimethylaluminum and $H_2O$ on Pd(111, Pt(111)and Cu(111) surfaces: Observation of a pressure-gap effect*, ACS 246th National Meeting, Indianapolis, IN, September 2013 (Oral presentation).
- **A. Gharachorlou**, M. D. Detwiler, Y. Lei, J. Lu, J. W. Elam, D. Y. Zemlyanov, J. F. Greeley, W. N. Delgass and F. H. Ribeiro, *Mechanistic Studies of Palladium (II) hexafluoroacetylacetonate Reactions on $TiO_2$ and Preparation of Palladium Nanoparticles by Atomic Layer Deposition*, 23rd NAM, Louisville, KY, June 2013. (Poster presentation)
- **A. Gharachorlou**, M. D. Detwiler, Y. Lei, J. Lu, J. W. Elam, D. Y. Zemlyanov, J. F. Greeley, W. N. Delgass and F. H. Ribeiro, *Inverse Catalysts of Aluminum Oxide on Pt(111) Prepared by Atomic Layer Deposition*, 23rd NAM, Louisville, KY, June 2013. (Poster presentation)
- M. D. Detwiler, **A. Gharachorlou**, A. V. Nartova, J. W. Elam, D. Y. Zemlyanov, W. N. Delgass and F. H. Ribeiro, *Gas phase formic acid decomposition on platinum metal single crystal and polycrystalline surfaces: Kinetics and characterization*, CCC Spring symposium, Naperville, IL, May 2013. (Poster presentation)
- **A. Gharachorlou** and F. Goharpey, *Study on Phase separation kinetics of PS/PVME (Polystyrene/Polyvinyl methyl ether) in the presence of Spherical Nanoparticles as a compatibilizer*, International Conference on Multifunctional Hybrid and Nanomaterial, Tours, France, March 2009. (Oral presentation)
- **A. Gharachorlou** and F. Goharpey, *Determination of Phase Separation Dynamic Behavior of PS/PVME (Polystyrene/Polyvinyl methyl ether) Blends*, IUPAC Congress, Turin, Italy, August 2007. (Oral presentation)
- S. Behdad, **A. Gharachorlou** and M. Mohseni, *A comparison between the adhesion performance of a stoving acrylic paint on TPO (Thermoplastic polyolefin's) substrate using flame pretreatment and*

*chlorinated polyolefin (CPO) tie layer*, 30th Annual Meeting of the Adhesion Society of America, February, 2007. (Poster presentation)

## ► Technical Skills and Languages

- Expertise in using X-ray Photoelectron Spectroscopy **(XPS)**, Atomic Force Microscopy **(AFM)**, Scanning Tunneling Microscopy **(STM)**, Low Energy Electron Diffraction **(LEED)**, Kinetic measurements by Gas Chromatography **(GC)** and Fourier transform infrared spectroscopy **(FTIR)** techniques for **characterization** and problem solving in **heterogeneous catalysis**. Gas handling and purification, laboratory safety. Experience with in-situ X-ray Photoelectron Spectroscopy at Synchrotron Radiation Source BESSY II.
- **Software**: ***CasaXPS***, OriginPro, Chemstation Software (GC), WinXAS (EXAFS, XANES), MATLAB, AutoDesk and basic programming various languages.
- Proficient in **French** and English with knowledge in **Arabic.**

## ►Teaching Experience

- Supervised students Chemical Engineering laboratory (CHE 511) and ensure the safety of each experiment in lab. **Fall 2012**
- Conducted recitation for Statistical Modeling And Quality Enhancement (CHE 320) course